

UC Berkeley

UC Berkeley Electronic Theses and Dissertations

Title

Orientation-Dependent van der Waals Epitaxy of Graphene on Ir(111)

Permalink

<https://escholarship.org/uc/item/9kb635nt>

Author

Rogge, Paul Charles

Publication Date

2014

Peer reviewed|Thesis/dissertation

Orientation-Dependent van der Waals Epitaxy of Graphene on Ir(111)

by

Paul Charles Rogge

A dissertation submitted in partial satisfaction of the

requirements for the degree of

Doctor of Philosophy

in

Engineering – Materials Science and Engineering

in the

Graduate Division

of the

University of California, Berkeley

Committee in charge:

Professor Oscar D. Dubón Jr., Chair

Professor Mark Asta

Professor Sayeef Salahuddin

Fall 2014

Orientation-Dependent van der Waals Epitaxy of Graphene on Ir(111)

Copyright 2014
by
Paul Charles Rogge

Abstract

Orientation-Dependent van der Waals Epitaxy of Graphene on Ir(111)

by

Paul Charles Rogge

Doctor of Philosophy in Engineering – Materials Science and Engineering

University of California, Berkeley

Professor Oscar D. Dubón Jr., Chair

Understanding the fundamental mechanisms that control van der Waals epitaxy of two-dimensional layered materials is necessary in order to grow large, defect-free crystals. Two-dimensional materials, such as graphene and transition-metal dichalcogenides, are a relatively new class of materials that display unique electronic and optical properties and are promising candidates for continued improvement of microelectronics, improved sensors, and many other applications, some not yet conceived. However, the growth of single-crystal two-dimensional materials is often frustrated by the fact that different in-plane rotational variants nucleate and grow. Their nucleation is a consequence of the weak interaction between the film and substrate that is characteristic of van der Waals epitaxy. It is well known that the nucleation and growth behavior of graphene islands greatly varies with the growth substrate, which is surprising given the weak interaction between the film and substrate. A unique system is graphene on Ir(111) because graphene islands have properties that depend on their in-plane orientation relative to the Ir(111) lattice. Thus, graphene on Ir(111) is a model system to investigate the fundamental factors that control the van der Waals epitaxy of graphene.

Experimentally, Ir(111) presents significant advantages for investigation by low-energy electron microscopy, including the quantification of surface adatom concentrations during growth. By using low-energy electron microscopy, the *real-time* evolution of graphene islands on Ir(111) were investigated during growth and annealing. First, island growth characteristics are compared under identical driving forces in order to isolate the orientation-induced differences. In the temperature range of 750-900 °C, islands rotated relative to the Ir(111) lattice are more faceted than islands aligned with the substrate (R0). Further, the growth velocity of rotated islands depends not only on the C adatom supersaturation but also on the geometry of the island edge. The growth of rotated islands is determined to be kink-nucleation-limited, whereas aligned islands are kink-advancement-limited. These different growth mechanisms are attributed to differences in the graphene edge binding strength to the substrate. By analyzing the growth rate as a function of the C adatom concentration, the size of the attachment species for R0 is determined to be a 4-atom carbon cluster.

Next, the evolution of multi-domain graphene islands was monitored during annealing. Three distinct mechanisms were observed in which islands tend to align with the substrate: 1) the simultaneous growth of aligned domains and dissolution of rotated domains, i.e., “ripening”, 2) domain boundary motion within islands, and 3) continuous lattice rotation of entire domains. By measuring the relative growth velocity of domains during ripening, the driving force for alignment is estimated to be on the order of 0.1 meV/C atom and increases with rotation angle. A simple model of the atomic-scale corrugation and resulting energy of the graphene sheet as a function of the rotation angle supports the experimental findings. It is proposed that the origin of the preferential alignment is caused by the varying degree to which carbon atoms can attain the preferred distance from the substrate: the graphene bending rigidity prevents the sheet from following the short wavelength corrugations inherent in highly rotated domains. The epitaxial properties observed here are common to graphene on many substrates; thus, it is concluded that the corrugation-induced energy is a significant factor in the resulting epitaxial relationship with the substrate during van der Waals epitaxy. This indicates that in order to control the rotational order in films of two-dimensional materials, growth should occur on substrates where corrugations are induced. Finally, these results show that annealing can still improve rotational order in graphene films on a variety of substrates.

To my family, friends, and all others who supported me along my journey.

Contents

Contents	ii
List of Figures	v
List of Tables	vii
List of Symbols	viii
1 Introduction	1
1.1 van der Waals epitaxy of two-dimensional materials: Motivation and overview	1
1.2 Two-dimensional materials	2
1.3 Graphene synthesis	4
1.3.1 Exfoliation of graphite	4
1.3.2 Silicon carbide	5
1.3.3 Vapor deposition	6
1.4 Current challenges	8
1.5 This dissertation	9
2 Background	10
2.1 Crystal growth	10
2.1.1 Terrace-step-kink model	11
2.1.2 Attachment-limited and diffusion-limited growth kinetics	13
2.1.3 Kossel and non-Kossel growth	14
2.1.4 Crystal growth summary	17
2.2 Graphene on Ir(111): A model system	17
2.2.1 Literature review of graphene on Ir(111)	17
2.2.2 Moirés and incommensurate films	19
2.2.3 Summary	20
3 Experimental Techniques	21
3.1 Low-energy electron microscopy (LEEM)	21
3.1.1 Introduction	21
3.1.2 LEEM instrumentation	23

3.1.3	LEEM resolution	24
3.1.4	Film growth in LEEM	25
3.1.5	Quantifying adatom concentrations in LEEM	25
3.2	Low-energy electron diffraction (LEED)	26
3.2.1	Determining the zigzag orientation for graphene islands	27
4	Orientation-dependent growth mechanisms of graphene on Ir(111)	29
4.1	Assigning graphene island orientations: LEED analysis	30
4.2	Island shape analysis	32
4.2.1	Method: Fourier transform of island shapes	32
4.2.2	Results	32
4.3	Comparison of R0 and rotated island growth	36
4.3.1	Island growth experimental process	36
4.3.2	Measuring local edge velocities	36
4.3.3	Results	36
4.3.4	Growth model: kink-nucleation- vs. kink-advancement-limited	39
4.3.5	Graphene edge binding to the substrate	40
4.4	Graphene growth by cluster attachment	41
4.4.1	Determining the equilibrium adatom concentration	42
4.4.2	Determining the attachment species for R0	42
4.4.3	Growth species for rotated domains	45
4.4.4	Unifying cluster attachment to Ru(0001) and Ir(111)	46
4.5	Summary and significance of findings	47
5	Reorientation of graphene domains on Ir(111)	48
5.1	Experimental process	49
5.2	Results	49
5.3	Discussion of ripening results	51
5.4	Relative graphene chemical potential as a function of orientation	51
5.5	Quantitative differences in chemical potential	52
5.5.1	Determining average island growth rates	54
5.5.2	Effect of island edge energies	55
5.6	Domain boundary motion discussion	56
5.7	Comment: Continuous lattice rotation	57
5.8	Orientation-dependent flexure model of graphene on Ir(111)	58
5.9	Density functional theory results	62
5.10	Summary and significance	64
6	Conclusions and future work	66
6.1	Summary of findings	66
6.2	Unifying growth and reorientation results	67
6.3	Future directions	68

6.3.1	Modeling the graphene edge/substrate interaction	68
6.3.2	Domain boundaries between R0 and rotated domains	68
6.3.3	Modeling the continuous lattice rotation mechanism	68
6.3.4	Applying the moiré corrugation model to other systems	69
6.3.5	Ultra-fast LEED of graphene nucleation	69
6.3.6	Mosaicity in bilayer graphene	69
A	Supplementary data	71
A.1	Islands used for shape analysis	71
A.2	Island growth experiments	76
A.3	Ripening: Simultaneous growth and dissolution	82
A.4	Ripening: Continuous domain rotation	85
B	Data analysis code	88
B.1	Interactive Data Language (IDL)	88
B.2	Igor Pro code	89
B.3	ImageJ	89
	Bibliography	90

List of Figures

1.1	Graphene: Honeycomb structure of carbon	2
1.2	Graphene rotational variants on Ir(111)	8
2.1	Terrace-step-kink model of crystal growth	12
2.2	Adatom concentration profiles during diffusion-limited and attachment-limited growth	15
2.3	Kossel and non-Kossel crystal growth	15
2.4	Graphene moiré positions	19
3.1	Schematic of a low-energy electron microscope	22
3.2	LEED from multiple scattering events	27
3.3	Relationship between LEED and real-space graphene zigzag orientation	28
4.1	Select LEED patterns of graphene rotational variants on Ir(111)	30
4.2	Moiré analysis for determining orientation of graphene domains relative to Ir(111)	31
4.3	Fourier transform island shape analysis applied to a circle and hexagon	33
4.4	Fourier transform island analysis applied to graphene islands on Ir(111)	34
4.5	R0 and rotated island perimeter within $\pm 5^\circ$ of the zigzag as a function of the island area	35
4.6	Fitting procedure for correcting overlapping peaks for the Fourier transform island shape analysis	35
4.7	Typical graphene growth experiment	37
4.8	Local velocity measurements of R0 and rotated islands at 850 °C	38
4.9	Local velocity measurement of a rotated island grown at 950 °C	39
4.10	Orientation-dependent graphene growth model on Ir(111)	41
4.11	Determining the equilibrium C adatom concentration and results	43
4.12	R0 local velocity measurements for fitting analysis and R0 cluster attachment model	44
4.13	Scaling of R0 local velocity measurements and kinetic coefficient results	44
4.14	Average growth rate of rotated islands	46
5.1	Three mechanisms of graphene domain reorientation	50
5.2	Interpretation of ripening results	51

5.3	Orientation-dependent relative chemical potential of graphene domains on Ir(111)	52
5.4	Determining quantitative differences in chemical potential using temperature-controlled ripening	53
5.5	Quantitative differences in chemical potential as a function of orientation relative to R0 domains	55
5.6	Average growth rates of R0 islands	56
5.7	DFT results of graphene rotational variants on Ir(111) and comparison to moiré corrugation model	61
5.8	Energy per C atom as a function of graphene rotation angle obtained from the moiré corrugation model	62
5.9	The optB86b-vdW optimized R0, R7.5, R15, R22.5, and R30 graphene structures on Ir(111)	63
A.1	R0 and rotated graphene island shapes at 750 °C	72
A.2	R0 and rotated graphene island shapes at 800 °C	73
A.3	R0 and rotated graphene island shapes at 850 °C	74
A.4	R0 and rotated graphene island shapes at 900 °C	75
A.5	750 °C R0 island growth and local velocity measurements	76
A.6	800 °C R0 island growth and local velocity measurements	77
A.7	900 °C R0 island growth and local velocity measurements	78
A.8	750 °C rotated island growth and local velocity measurements	79
A.9	800 °C rotated island growth and local velocity measurements	80
A.10	900 °C rotated island growth and local velocity measurements	81
A.11	Ripening: simultaneous growth and dissolution example 1: The first observed ripening	82
A.12	Ripening: simultaneous growth and dissolution example 2	83
A.13	Ripening: simultaneous growth and dissolution example 3	84
A.14	Ripening: continuous lattice rotation example 1	85
A.15	Ripening: continuous lattice rotation example 2	86
A.16	Ripening: continuous lattice rotation example 3	87

List of Tables

4.1	R0 local velocity fitting results	43
4.2	Fitting results of average growth velocity of rotated domains	46
5.1	Temperature-controlled ripening results	55
5.2	Graphene bending energies and relative binding energies obtained by DFT	64

List of Acronyms & Symbols

Acronyms

2D	two-dimensional
CVD	chemical vapor deposition
DFT	density functional theory
FOV	LEEM field-of-view
FT	Fourier transform
hBN	hexagonal boron nitride
HOPG	highly oriented pyrolytic graphite
IDL	Interactive Data Language
I-V	LEEM intensity as a function of start voltage
LDA	local density approximation
LEED	low-energy electron diffraction
LEEM	low-energy electron microscopy
MEM	mirror electron microscopy
ML	monolayer
PAW	projector-augmented-wave
PVD	physical vapor deposition
R	rotation angle
RF	radio frequency
STM	scanning tunneling microscopy
TEM	transmission electron microscopy
TMD	transition metal dichalcogenide
TSK	terrace-step-kink (model)
UHV	ultra-high vacuum
vdW	van der Waals
vdWE	van der Waals epitaxy

Symbols

a	kink depth
a_s	lattice spacing along the step edge
A	island area
B	step kinetic coefficient
$B_{a,k}$	kink kinetic coefficient
$B_{J,nk}$	kinetic coefficient for non-Kossel crystal with kink nucleation
c^{ad}	adatom concentration
c_{bulk}	carbon concentration in the substrate bulk
c^{eq}	equilibrium adatom concentration
$c^{eq,R0}$	R0 equilibrium adatom concentration
$c^{eq,RX}$	rotational variant equilibrium adatom concentration
c_n	density of n -atom clusters
d	carbon-carbon distance in graphene (1.42 Å)
d_{Gr}	magnitude of graphene k -vector
d_{Ir}	magnitude of Ir(111) k -vector
d_k	kinetic length
d_m	length of kink nucleation species
d_{mo}	magnitude of moiré k -vector
d_n	length of growth species
D_s	surface diffusion coefficient
E_a	attachment barrier to a kink
$E_{a,k}$	cluster attachment barrier for kink nucleation
E_b	bending energy
E_{BE}	binding energy
E_c^{LDA}	vdW functional local density approximation
E_c^{vdW-DF}	vdW functional non-local correlation energy
E_d	surface diffusion barrier
E_f	enthalpy of adatom formation
E_k	kink formation energy
E_m	energy to form an m -atom cluster
E_n	energy to form an n -atom cluster
E_{xc}	van der Waals functional
$E_x^{optB86b}$	vdW functional exchange energy
f_a	attachment attempt frequency
F_b	bending force
f_d	diffusion attempt frequency
F	flux
I	LEEM image intensity
I_0	initial LEEM image intensity

J	kink nucleation rate
\mathbf{J}_d	diffusion flux
k	curvature
\mathbf{k}_{Gr}	graphene k -vector
\mathbf{k}_{Ir}	Ir(111) k -vector
\mathbf{k}_{m0}	moiré k -vector
k_s	spring constant
K	mean curvature
l	distance between step edges
m	size of kink nucleation species
n	size of attachment species to a kink
p	island perimeter
p_{ave}	average island perimeter
P	probability of attachment to a kink site
R	radius of curvature
r	radius
r_i	position of atom i
S_0	footprint of a C atom in graphene
t	time
T	temperature
v_{ave}	average island growth velocity
v_k	kink velocity
v_{R0}	R0 island growth rate
v_s	step velocity
V_s	LEEM start voltage
γ	domain boundary energy per unit length
ϵ	binding energy
λ	reflectivity proportionality factor
λ_b	mean bending rigidity
μ	chemical potential
ρ_k	kink density
$\rho_{k,eq}$	equilibrium kink density
ϕ	rotation angle between graphene and substrate lattice
Φ	polar angle
Ω	atomic volume

Acknowledgments

This dissertation was only possible through the instruction and with the help of many. Of course, this would not have been possible without my advisor, Professor Oscar Dubón Jr., who extended a hand and gave me an opportunity for the taking. That opportunity was split between Berkeley and Sandia National Laboratories in Livermore, CA with Dr. Kevin McCarty and Dr. Norman Bartelt. Working under these three tremendously talented and knowledgeable people has provided me with a critical thinking mindset and communication skills that I will carry forward forever. It is difficult to convey my gratitude in words to these three and I will therefore borrow those of others. It was August of 2012 and I was sitting at the French Hotel Cafe in Berkeley, reading Ansel Adams' autobiography in preparation for an upcoming backpacking trip to the Ansel Adams Wilderness. I came across a thank you letter Adams sent to Alfred Stieglitz, a photographer whom Adams admired and had recently presented his photographs to. The following passage resonated with me; not only did Adams capture my feelings in this new and exciting time for me, but he also conveyed an ideal that it seems to me those of us in scientific research should aspire to. I knew that Oscar, Kevin, and Norm had achieved this and I hope that, some day, I will too.

... My work has become new and exciting to me as never before. The praise you give never nourishes conceit – it reveals too much of the future for that. And your criticism is never disintegrating. The entire experience evaluates much more than it defines, and the joy with which I will attack my problems from now on will be a joy that has nothing to do with conquest, superior accomplishment, fashionable fame and all the other transparent gewgaws that ornament the garment of social intercourse. I can see only one thing to do – make the photography (*research*) as clean, as decisive, and as honest as possible. It will find its own level.

- Ansel Adams to Alfred Stieglitz, November 29, 1936

The work in this dissertation was supported by many. From Sandia, I must also thank Dr. Shu Nie, who first trained me on the LEEM; Dr. Konrad Thürmer for his efforts on the corrugation model; Dr. Mike Foster for the DFT simulations; Dr. David Siegel for providing Igor Pro code; Dr. Farid el Gabaly for LEEM support; and Suzy Vitale for administrative help. From Berkeley I must thank the Dubon group members, especially Dr. Joe Wofford, Dr. Doug Detert, Alex Luce, and Jose Fonseca Vega. And I must thank Dr. Alejandro Levander, Dr. John Heron, Kyle Clark, Seth Fortuna, Amy Bergerud, Sibel Leblebici, and Emily Regier for lending an ear, offering support, and helping me along my path through graduate school.

Finally, I am thankful for my parents, Kristin and Gary, and my brothers, Eric and Brian, for their support in my academic endeavors. You have provided me the foundation upon which I am able to succeed. I am forever grateful.

Chapter 1

Introduction

1.1 van der Waals epitaxy of two-dimensional materials: Motivation and overview

Two-dimensional (2D) materials were discovered experimentally in 2004 when a single atom thick layer of C atoms, termed graphene, was isolated from a three-dimensional graphite crystal [1]. Although graphene had been observed on the surface of metal substrates in previous decades [2–5], it was the demonstration of its unique electronic properties that demarcated the emergence of 2D materials. These electronic properties have excited physicists and engineers alike. For physicists, graphene provides a simple benchtop solid-state system to study complicated phenomenon such as quantum electrodynamics [6] whereas engineers look to incorporate graphene into existing devices for a multitude of applications or even create new devices. Furthermore, the interest in 2D materials has not been limited to graphene; research is being conducted on many other 2D systems [7, 8], each with their own distinct properties. Together, these materials offer significant promise in improving existing technologies and the development of new ones.

The implementation of 2D materials requires controllable and repeatable synthesis in a scalable manner. Currently, the most successful production method is vapor deposition onto various substrates, including metals [9–14] and semiconductors [15]. In this technique, the growth of 2D materials occurs by van der Waals epitaxy (vdWE) [16–19], which is characterized by strong in-plane bonding within the 2D layer and weak out-of-plane bonding between the 2D film and the substrate. However, nucleation tends to result in many in-plane rotational variants relative to the substrate [12–14, 20–23], resulting in domain boundary formation, which limits electrical performance [24, 25]. To eliminate such defects, nucleation and growth must be controlled. However, the fundamental mechanisms that govern nucleation and growth during vdWE are not well understood. Specifically, it is not known how these disparate interactions, strong in-plane and weak out-of-plane bonding, affect nucleation and growth, and why some substrates produce graphene films with improved rotational order than others. To this end, this dissertation explores the growth of graphene on Ir(111).

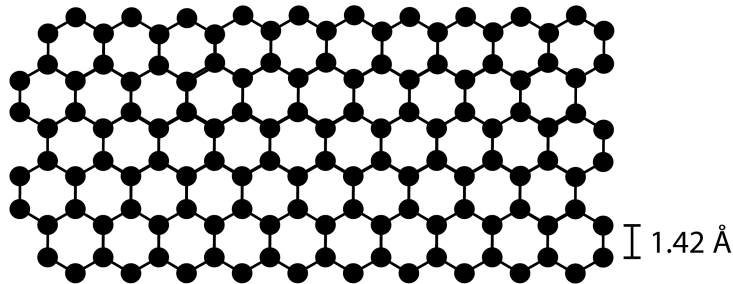


Figure 1.1: The atomic honeycomb structure of carbon atoms that constitute graphene.

In this model system, nucleation results in many graphene in-plane rotational variants relative to the Ir(111) substrate. In Chapter 4, the differences in growth characteristics among these rotational variants are explored using low-energy electron microscopy (LEEM), elucidating the influence of how these disparate bonding interactions affect the growth process. In Chapter 5, the evolution of graphene rotational variants during annealing is observed using LEEM. By characterizing this evolution, the energy landscape of graphene rotational variants is deduced. Together, these results provide fundamental insight into the factors that significantly influence vdWE of 2D materials and provide important insight into improving their rotational order.

1.2 Two-dimensional materials

Layered materials in their bulk form consist of sheets with self-terminated surfaces (i.e., no dangling bonds) one to a few atoms thick held together by vdW interactions [1, 7], for example, graphite [1, 26]. Two-dimensional materials consist of a single, isolated layer of their bulk counterpart. Graphene consists of single-atom thick honeycomb structure of C as shown in Figure 1.1. Its initial isolation was achieved by the physical exfoliation of a bulk graphite crystal. The weak out-of-plane interaction is a consequence of the sp^2 hybridization between C atoms within the 2D layer, resulting in the formation of three σ bonds, one between each C atom and its three nearest-neighbors, which are separated by 1.42 Å [27]. The remaining electron in the p orbital covalently bonds with the neighboring atoms, forming a π orbital that is perpendicular to the planar structure. With the four valence electrons of each C atom accounted for, no valence electrons remain to form strong chemical bonds with the substrate.

The structural configuration of graphene leads to its unique electronic and optical properties [28, 29]. Graphene is a zero-gap semiconductor, where the valence and conduction bands touch at single points within the Brillouin zone [1, 28, 29]. In contrast to typical gapped semiconductors, graphene's bandstructure results in a Fermi velocity independent of the electron energy or momentum [29]. These so-called massless Dirac fermions can be thought of as electrons with no mass [6]. It is this property that leads to the exceptional electronic

and optical properties of graphene and provides a simple benchtop experimental system to study numerous quantum electrodynamic phenomena, such as the anomalous integer quantum Hall effect, the Klein paradox, and chiral quantum Hall effects [29]. Other properties more relevant to technology include an exceptionally high mobility of $140,000 \text{ cm}^2/\text{Vs}$ at room temperature and carrier concentrations above $4 \times 10^{12} \text{ cm}^{-2}$ [30]. This high mobility at high carrier concentrations is due to ballistic transport on the micron scale, an indication of the superior electronic quality of graphene. Optically, graphene has an exceptionally wide transparency bandwidth, absorbing 2.3% from ultraviolet to infrared [31]. Remarkably, this one-atom thick material is still visible to the naked eye [32].

The strong carbon-carbon sp^2 bonding of pristine graphene leads to an extremely high strength. The measured Young's modulus is 1.0 TPa [33] and holds the title of strongest material ever tested to date. This is considered its intrinsic strength, that is, the strength required to break the carbon-carbon bonds, not the strength required to propagate defects, which is typically associated with material deformation. Furthermore, the two-dimensional nature of graphene results in a flexibility that does not appreciably deteriorate its electronic properties [34, 35].

Together, these properties make graphene attractive for a number of applications. Its high mobility is well-suited for analog radio frequency (RF) electronics, such as receivers, transmitters, and amplifiers [36], with operation at frequencies above 400 GHz [37] demonstrated. Its transparency combined with its high conductivity make it ideal as a transparent conducting electrode for electronic displays and solar cells [31]. With the addition of its flexibility, it is also well-suited for bendable electronics [34, 35]. Sensors, including chemical, biological, optical, and mechanical, are another area of potential applications for graphene [38]. Because of its single-atom-thick structure, it has the highest possible surface to volume ratio for a material, an important consideration for sensors. Furthermore, the electronic noise in graphene is exceptionally low, resulting in the detection of single molecules [39]. However, because graphene has no inherent band gap, it is not suitable to replace the active component of transistors, solar cells, and light-emitting diodes. A band gap can be induced by controlling the graphene morphology, either through narrow (10 nm) ribbons [40–42] or by AB-stacked bilayer graphene [43, 44]; but, significant synthesis challenges remain in these areas.

The excitement caused by graphene has renewed interest in other layered materials, such as hexagonal boron nitride (hBN) and transition-metal dichalcogenides (TMDs), which do have intrinsic band gaps. For example, hBN has a similar 2D hexagonal structure as graphene but the two C atoms per unit cell replaced by a B and N atom, and has a band gap of approximately 5.9 eV [45]. TMDs are 2D compounds that consist of a more complex structure, typically a transition metal atom (M) in between two layers of chalcogen atoms (X) with a resulting stoichiometry of MX_2 . For example, single-layer MoS_2 has a direct band gap of 1.9 eV [46]. Thus, 2D layered materials span the entire range of electronic conductivities, from metal to semiconductor to insulator. Not surprisingly, their combination resulted in the demonstration of an all 2D transistor, where graphene was used as the source, drain, and gate contacts, MoS_2 as the channel, and hBN as the dielectric [47].

2D layered materials are not limited to simply replacing traditional semiconductors and dielectrics. Other 2D compounds exhibit various effects, such as superconductivity, thermoelectricity, and act as topological insulators [48]. Applications include optoelectronics, spintronics, catalysts, chemical and biological sensors, supercapacitors, solar cells, and battery components [48], and more have yet to be discovered. Clearly, the discovery of graphene and the exploration of its extraordinary properties have led to a significant research effort in the general field of 2D materials, and these materials offer promise for continued improvement of existing technologies and the creation of new technologies. However, these exceptional properties were obtained from samples singled out due to their perfection, and are not necessarily representative of what is currently possible in terms of large-scale production. Because graphene is relatively easy to produce on the laboratory scale, the understanding of its physical properties and incorporation into devices has proceeded exceptionally fast. In contrast, the synthesis of large, high-quality graphene sheets has lagged. This is one of the major bottlenecks restricting the incorporation of 2D materials into existing and new technologies. Understanding the fundamentals that govern the synthesis of 2D materials should help facilitate their deployment.

1.3 Graphene synthesis

The science of crystal growth has been concerned historically with the controlled production of materials, often with the goal of reducing or controlling defects to improve performance. This is especially true for electronic materials, where defects reduce mobility by scattering electrons, reduce photovoltaic efficiency by acting as recombination centers of separated charge carriers, and reduce brightness in light-emitting diodes and lasers by acting as non-radiative recombination centers. Not surprisingly, the electrical and optical properties of graphene and other 2D materials depend on their crystalline quality as well. In the sections below, the three main methods of producing high-quality, crystalline, single-layer graphene are discussed.

1.3.1 Exfoliation of graphite

The initial discovery of graphene was achieved by mechanical exfoliation of highly oriented pyrolytic graphite (HOPG) [1]. In this method, a three-dimensional piece of graphite is repeatedly peeled using a sticky adhesive, such as tape. Each time the crystal is peeled its thickness decreases. Eventually after repeated peeling, flakes of multilayer and single-layer graphene are obtained. This method tends to produce graphene flakes that are single-crystalline and is still the main synthesis method for producing high-quality samples used to experimentally test graphene's electronic properties. The flake sizes produced by exfoliation tend to be relatively small, on the order of 10-500 μm^2 [1, 6, 49]. Although exfoliation produces superior quality graphene flakes, the throughput and size makes exfoliation impractical for any large-scale production of graphene films.

1.3.2 Silicon carbide

Silicon carbide (SiC) wafers have also been shown to produce graphene. The wafers are heated to temperatures of 1200-1600° C, at which point the Si atoms sublime and leave behind a C-rich surface that ultimately forms graphene layers [50–52]. Initial annealing performed in ultra-high vacuum (UHV) produced low-quality graphene films. Various deleterious features were shown to develop on the surface, including etch pits, fingers, and step erosion [51, 52]. Furthermore, controlling the number of graphene layers that form has also proved challenging. In UHV, anywhere from 3-10 graphene layers form [50]. This is detrimental because the properties of graphene are only observed for single monolayers and quickly diminish with increasing layer number. These artifacts were partially mitigated by annealing in a silicon-rich atmosphere [52], which maintains the system closer to equilibrium. However, layer-control is still a significant problem for producing graphene on SiC substrates. The best results have only shown select areas with single-layer graphene, whereas other areas are bilayer or more. Furthermore, Si atoms can collect at the SiC step edges during growth, which act as electron scatterers and severely diminish the conductivity in directions perpendicular to the SiC steps [53]. This ultimately limits any devices to be constrained within the SiC terraces.

It is important to note that the electronic bandstructure denotes the areas of single-layer graphene on SiC, specifically a linear dispersion [50]. Structurally, multiple carbon-rich layers may exist. When growing graphene on the Si-terminated substrate, another carbon-rich layer exists beneath the top graphene layer [54]. This layer acts as an insulating buffer because some C atoms covalently bond with Si atoms. Below this buffer exists dangling bonds from Si atoms and results in charge transfer to the top graphene layer, leading to significant charge densities that ultimately decrease the mobility [55–57]. Thus, in order to improve the electrical performance, additional synthesis steps, such as hydrogen intercalation, are performed to saturate the Si dangling bonds and electrically isolate the top graphene layer [55, 56]. Even then, mobilities only reach 11,000 cm²/Vs at 0.3 K [57].

The effect of dangling Si bonds is mitigated when using C-terminated SiC. Initially, graphene quality was relatively poor due to rotational disorder [54]. An advance was made by using a radio frequency furnace to heat the SiC substrates, which resulted in significantly improved graphene layers; however, the experimental conditions are not well documented and the reasons for improved quality are not well known at this time [58]. Again, controlling the number of layers is still a significant challenge, with 4-5 graphene layers typically forming [54].

In summary, annealing SiC is a viable method to achieve large-scale production graphene electronics. A number of significant challenges remain, including controlling layer thickness, the detrimental effects of the underlying layers, rotational disorder, and the effect of SiC steps on performance.

1.3.3 Vapor deposition

Vapor deposition is another technique that produces high-quality graphene. In this technique, graphene grows heteroepitaxially on foreign substrates, such as metals and semiconductors. Both physical vapor deposition (PVD) and chemical vapor deposition (CVD) have been successful. CVD is by far the more prevalent method and will be discussed first.

During CVD the growth species are transported to the substrate in the form of a gas [59]. Because the gas fills the entire chamber, this method is less restrictive on sample and source placement than PVD, discussed below. CVD requires a catalytic substrate to decompose the vapor molecule into its constituents, typically activated by elevated substrate temperatures [59]. The resulting constituents then become adsorbed onto the substrate surface, at which point they undergo typical mechanisms of diffusion, nucleation, growth, or desorption. In the case of graphene growth, hydrocarbons are typically used as the active gas species. These hydrocarbons are often mixed with other carrier gases, such as H_2 [9, 60]. Substrates used for CVD graphene growth include Ru(0001) [10, 61], Ir(111) [11, 20, 21, 62, 63], Cu [9, 23, 60], Pt(111) [13], Ni(111) [64, 65], and Ge [15, 66] and are typically heated to temperatures ranging from 750 °C to just below their melting temperature during growth. One of the main advantages of CVD is the self-limiting nature of single monolayer growth. Graphene itself is inert. As the substrate becomes covered with a graphene monolayer, the contact between the vapor and the catalytic substrate is eliminated and further growth ceases.

An important constraint on the substrate is a low C solubility. Although CVD limits growth to one monolayer from above, second layers can be nucleated underneath the first by C segregation [67, 68], especially as the substrate is cooled from the growth temperature. Metals with a high C solubility, such as Ni and Pd, present significant challenges in controlling layer thickness [14, 69]. On the other hand, Cu has a relatively low C solubility [70] and has become one of the main substrates for CVD graphene growth [9, 23, 60]. Although this eliminates second layer formation during cooling, second layers can nucleate during growth before the first monolayer is completed [68], possibly due to C adatoms existing under the monolayer islands. Techniques have been developed to mitigate second layer nucleation, resulting in uniform monolayer graphene [71].

For substrates that are not catalytic to the decomposition of hydrocarbons, CVD cannot be employed for graphene growth. Instead, physical vapor deposition has been used to grow graphene. These substrates include Au [12], Ag [72], and also Cu [22, 73] in high-vacuum atmospheres. During PVD, a solid source is evaporated, typically by electron bombardment, to produce a flux of C atoms [59]. This so-called line-of-sight deposition, where the atoms travel through the chamber until they impact a solid surface, creates constraints on the deposition geometry, namely that the substrate must be within this line-of-sight of the source. Not surprisingly, PVD presents challenges in growing only a single monolayer since growth is no longer self-limiting. In terms of growth kinetics, growth by PVD is the same as CVD in the case of graphene on Ru(0001), an indication that the CVD by-products do not significantly affect the growth process [21].

Graphene grown by vapor deposition, especially CVD, stands out due to two reasons:

its superior structural and electronic quality. Scanning tunneling microscopy (STM) has shown that CVD graphene is of exceptional crystalline quality [11, 62, 74, 75]. Furthermore, substrate steps do not impact the crystallinity: films remain continuous and defect-free as they grow across substrate steps [63, 73]. The superior quality is evident in the mobility of graphene grown by CVD, up to 45,000 cm²/Vs [76], and is much higher than graphene on SiC.

However, the electronic properties graphene are tested only after the film has been removed from the substrate and placed on an insulating substrate, typically SiO₂ or BN [76]. Thus, if CVD graphene is to be implemented into devices, it must first be removed from its metal substrate. Various techniques have achieved this, most notably dissolving the underlying metal substrate [9, 77]. A support layer, typically PMMA [9, 77, 78], is spun onto the graphene layer and then the substrate is dissolved. After placing the graphene on an insulating substrate, the support layer is removed, typically by soaking in acetone [78]. This transfer process typically leaves behind residues that detrimentally affect the electronic properties; however, significant progress has been made and transferred graphene exhibits high mobilities (45,000 cm²/Vs [76]).

More recently, CVD graphene was grown on Ge(110) and was removed by depositing a thin layer of gold onto the graphene and simply peeling the graphene off the substrate after [15], presumably due to the extremely weak interaction strength between the graphene and the germanium (the interaction strength between graphene and Au has been estimated to be on the order of 13 meV/C atom [74]). Likely, other materials such as dielectrics could be deposited on the graphene in order to remove it from the Ge substrate, eliminating the need to subsequently dissolve any metals. Furthermore, removal of graphene from Ge has been achieved by simply dipping the graphene/Ge wafer into warm water, at which point the graphene layer releases from the substrate [79].

It is clear that graphene growth by vapor deposition has a number of significant advantages over graphene produced by exfoliation or on SiC. Both vapor deposition and SiC offer scalable solutions to production, however, vapor deposition, especially CVD, offers the possibility of much larger sheets: it is limited only by the substrate size. Metal foils can be made arbitrarily large and Ge wafers currently exist up to 12 inches in diameter [80], whereas SiC wafers are currently at 6 inches [81]. Furthermore, Ge wafers are currently one-third the cost of SiC ([80, 81] and Ge wafers are reusable [15], whereas graphene devices are integrated into the SiC wafer. CVD also offers a significant advantage in controlling layer uniformity due to the self-limiting growth of a single monolayer. Most importantly, graphene produced by vapor deposition has electronic properties approaching that of high-quality exfoliated graphene. These advantages of vapor-deposited graphene over exfoliation and SiC make it a very promising candidate for the production of large-scale, high-quality graphene films.

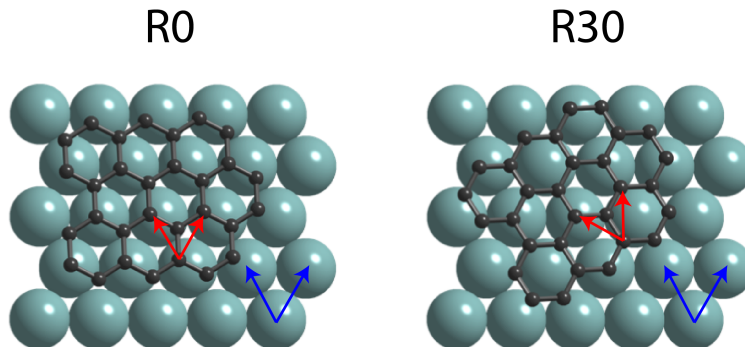


Figure 1.2: Illustration of a graphene lattice on top of an Ir(111) lattice. If the graphene lattice vectors (red arrows) are aligned with the Ir(111) lattice vectors (blue lines), the orientation is termed ‘aligned’ or R0 (left). Domains termed ‘rotated’ occur when the graphene lattice is misoriented from the substrate lattice vectors (right), labeled by the letter R followed by the angle of misorientation, e.g., R30 here. (Figure courtesy of K. F. McCarty)

1.4 Current challenges

Although graphene growth by vapor deposition exhibits clear advantages, a significant drawback remains towards the production of single-crystalline films. Rotational disorder is common in films grown by vapor deposition. During nucleation, graphene islands can assume various orientations relative to the substrate, so-called in-plane rotational variants [12–14, 20–22, 25, 73], as shown in Figure 1.2. As these islands grow and coalesce, a domain boundary forms due to their relative misorientation. These domain boundaries have been shown to degrade the electronic performance of the graphene films [24, 25, 76].

Rotational variants have been shown to nucleate on Ir(111) [20, 21, 67], Pt(111) [13], Pd(111) [14], Ni(111) [82], Cu(100) [73], Cu(111) [22], Cu foils [25], Au(111) [12], Ge(111) [15], and Ge(110) [15]. One exception is graphene grown on Ru(0001) where only a single orientation nucleates [10, 61], resulting in single-crystalline films. Unfortunately, graphene is difficult to remove from Ru(0001) and the substrate is too expensive to dissolve in order to produce free-standing films. Recently, graphene on Ge(110) was reported to be single-crystalline [15]. The single orientation was only obtained after optimizing the deposition conditions, namely the ratio of H_2 to CH_4 [15]. At higher partial pressures of CH_4 , rotational disorder was present. Only after lowering the CH_4 partial pressure did a single orientation emerge.

In contrast, graphene grown on Ir(111) [20, 21, 67] and Pd(111) [14] produce many in-plane rotational variants that span the full range of the possible 30° misorientations (31° is equivalent to 1° of misorientation), resulting in significant rotational disorder. Other substrates, such as Cu(111) and Au(111), exhibit rotational variants, but their rotational disorder is significantly reduced. In the case of Au(111), over 95% of graphene domains are

of a single orientation [12], whereas graphene on Cu(111) tends to exhibit a small spread of orientations, for example $\pm 3^\circ$ about R0 [22].

The source of these variations in nucleation and growth characteristics is currently unknown. Clearly, in order to consistently produce large-scale, single-crystal graphene films on a variety of substrates, a better understanding of the nucleation and growth processes of these rotational variants is needed.

1.5 This dissertation

In this dissertation, the growth and stability of graphene rotational variants on Ir(111) are explored using low-energy electron microscopy. An introduction to crystal growth concepts is presented in Chapter 2 along with a review of graphene on Ir(111), including the factors that make graphene on Ir(111) a model system to study. Experimental techniques are presented in Chapter 3, specifically LEEM. In Chapter 4, the growth properties of graphene rotational variants on Ir(111) are investigated. Here, growth morphology and growth rates are correlated to elucidate the growth mechanisms. The C species responsible for attachment is also discussed. In Chapter 5, the relative stability of rotational variants is observed during annealing. Experimental techniques to determine the energy landscape of rotational variants are presented along with the results. A simple model is developed to help explain the experimental findings and provides insight into the nucleation characteristics observed on various substrates. In Chapter 6, the growth and stability results are discussed in broader terms of the energy landscape of graphene, the implications of this work, and possible future directions of research.

Chapter 2

Background

In this chapter, an introduction to the science of crystal growth is presented with emphasis placed on concepts that directly relate to the work presented in this dissertation. The equations developed here illustrate the insight that can be gained by measuring step velocities as a function of adatom concentrations. This type of experiment has historically been limited to crystal growth from solutions [83–86] because growth rates are slow enough that they can be monitored by *in-situ* techniques such as atomic force microscopy and the concentration of the growth species is easily controlled experimentally. In the case of vapor phase growth, it is much more challenging to precisely determine adatom concentrations during growth. However, a relatively new technique using low-energy electron microscopy has been demonstrated to accurately measure adatom concentrations during growth [21, 61, 87, 88] and is employed in this dissertation to investigate graphene growth mechanisms. Finally, a review of the relevant literature of graphene on Ir(111) is given and is discussed in context of graphene on other substrates in order to highlight its use as a model system, along with the experimental advantages of iridium as a substrate for graphene growth.

2.1 Crystal growth

The science of crystal growth is concerned with understanding the thermodynamics and kinetics of phase transformations where the final product is of the solid phase. For example, growth from the liquid or vapor, or transformations from one solid phase to another. The structure of the resulting solid has significant implications on its properties. Foreign atoms incorporated into the atomic lattice can significantly degrade electronic and optical properties of semiconductors [89]. Line defects, such as dislocations resulting from lattice mismatch between film and substrate or grain boundaries that form from the coalescence of misoriented grains, similarly reduce electronic and optical performance in semiconductors [59]. In other cases, foreign atoms improve properties, such as the conductivity of doped semiconductors [89] or the mechanical properties of structural materials, e.g., steel [90]. The challenge in crystal growth is determining how to control the formation of the solid in order to achieve

the desired structure and, thus, the resulting properties. A key step is to understand the ‘energy landscape’ [91] of the system, that is, what phases or structures form, i.e., nucleate, and what are the kinetic pathways and driving forces that govern their evolution and growth.

For graphene and 2D materials, the current challenge is to produce large-scale, single crystal films. The main impediment, as discussed in Chapter 1, is the nucleation of islands with various in-plane orientations relative to the substrate, which result in domain boundaries. Thus, this dissertation explores the energy landscape of graphene by investigating vdWE of graphene rotational variants. The following discussion is presented in the context of heteroepitaxial growth, that is, film growth on a foreign substrate.

2.1.1 Terrace-step-kink model

During crystallization, a driving force exists for atoms of one phase to transition to another, e.g., from a vapor to a solid. The atoms in the vapor do not directly add to the growing crystal; instead, the atoms adsorb onto the substrate and become adatoms [92]. These adatoms then undergo a number of processes: desorb and re-enter the vapor, dissolve into the substrate, diffuse along the substrate surface, combine with other adatoms to form clusters (i.e., nuclei), or attach to existing islands. In the limit that adatoms neither desorb nor dissolve and existing islands have already nucleated such that no further nucleation occurs, a simple picture of crystal growth emerges: the growth species adsorbs and diffuses along the surface until they attach to an island.

Growing islands are often understood in terms of the standard terrace-step-kink (TSK) model. Here, the top face of the island is a terrace, its edges are the steps, and along the steps exist kink sites, as shown in Figure 2.1(a). Kinks are so-called ‘half crystal sites’ because they have half the number of bonds compared to an atom in the crystal bulk [92]. In the TSK model, the most probable way for an adatom to attach to the growing crystal is through kink sites [92]. A simple qualitative argument can be made: when an adatom attaches to a kink site, the attaching species has one more completed bond than if it were to attach to an unknicked step edge (see Figure 2.1(b) and 2.1(c)); thus, its probability of detaching from the step edge is much higher than detachment from the kink. Furthermore, attachment to a kink does not alter the island edge energy, which is related to the number of dangling bonds at the island edge: attachment to a kink merely propagates the kink along the step edge, whereas attachment to a kink-free edge results in the formation of two kinks, and thus, two dangling bonds.

Equilibrium is achieved through communication between the various phases and manifests itself through mass transfer between them: atoms sample the various environments, resulting in a net transfer of atoms to phases of lower free energy. When there is no difference in free energy between the two states, there is no net mass transfer and the two states are said to be in equilibrium. Thus, for an island on a substrate, the island is in equilibrium with an adatom concentration, c^{eq} .

During crystal growth, a driving force is applied in the form of an external flux of the growth species. This increases the adatom concentration, c^{ad} , above its equilibrium value

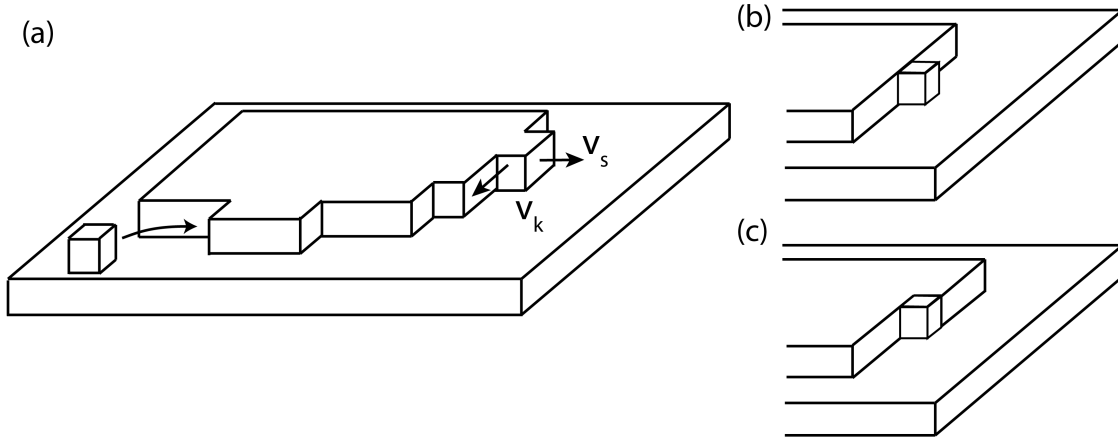


Figure 2.1: Terrace-step-kink model of crystal growth. (a) The island step edge has a number of kink sites. The most probable mode of attachment occurs when the growth species (cube) attaches to a kink site (arrow). The step velocity v_s depends on the kink velocity, v_k , and the density of kinks along the step edge. (b) Attachment to a straight step edge results in the attachment species having more unmet bonds than if it attaches to a kink as in (c).

and drives the growth of the crystal. In the TSK model, a simple expression for the step velocity can be deduced from geometry alone:

$$v_s = a\rho_k v_k \quad (2.1)$$

where a is the kink depth, ρ_k is the kink density, and v_k is the kink velocity. The kink density can be approximated by

$$\rho_k \approx (2/a_s)e^{-E_k/kT} \quad (2.2)$$

where a_s is the lattice spacing along the step edge, E_k is the kink formation energy, k is the Boltzmann constant, and T is the absolute temperature. Because the creation of a kink results in two kink sites, a factor of two is present in Equation 2.2. In many cases of metal and semiconductor growth, E_k is on the order of the thermal energy, kT [85, 93], which results in large kink densities that approach the upper limit of one kink at every other lattice site. In this high kink density limit, the kink density is constant during growth and the resulting growth rate depends only on the kink velocity [85, 93]. The kink velocity is given by [92]

$$v_k = Pd_n(c^{ad} - c^{eq}) = f_a d_n e^{-E_a/kT} (c^{ad} - c^{eq}) \quad (2.3)$$

where the probability of attachment to a kink is $P = f_a e^{-E_a/kT}$, where f_a is the attachment attempt frequency and E_a is the attachment barrier, d_n is the length of the growth species, and the quantity $(c^{ad} - c^{eq})$ is how far out of equilibrium the concentration of the growth species is, where c^{ad} is the adatom concentration directly next to the island step edge.

Combining Equations 2.2 and 2.3, the step velocity is now given by

$$v_s = \frac{2a}{a_s} e^{-E_k/kT} f_a d_n e^{-E_a/kT} (c^{ad} - c^{eq}) \quad (2.4)$$

The terms independent of concentration can be grouped into a kinetic coefficient, B [92],

$$v_s = B(c^{ad} - c^{eq}) \quad (2.5)$$

As one sees, in the high kink density limit the step velocity is linearly proportional to the quantity $(c^{ad} - c^{eq})$.

Up to this point, it was assumed that $E_k \approx kT$ and the growing step has a high kink density. However, if the conditions are such that $E_k \gg kT$, then kink nucleation can be relatively slow compared to kink advancement. In this regime kinks nucleate by attachment of clusters to the step edge [85, 94] and results in a kink density dependent on the adatom concentration. Therefore, Equation 2.1 is generalized to account for kink nucleation. At steady-state, the kink nucleation rate, J ($\text{cm}^{-1} \text{s}^{-1}$), is equal to the kink annihilation rate, $2\rho_k^2 v_k$ [85]. At zero supersaturation, J and v_k vanish and the kink density is equal to its equilibrium value, $\rho_{k,eq}$. Thus, the steady-state kink density is

$$\rho_k = \sqrt{\frac{J}{2v_k}} + \rho_{k,eq}. \quad (2.6)$$

The steady-state step velocity is now given by substituting the steady-state kink density into Equation 2.1,

$$v_s = a\sqrt{v_k J/2} + a\rho_{k,eq} v_k. \quad (2.7)$$

Here, the step velocity is no longer a simple linear function of $(c^{ad} - c^{eq})$ but now depends on the square root of the product of the kink velocity and the kink nucleation rate, both of which are functions of $(c^{ad} - c^{eq})$. Thus, in general, v_s is non-linear with $(c^{ad} - c^{eq})$, and its exact dependence will be discussed below. In the limit that kink nucleation from the adatom sea does not contribute to growth, $J = 0$, the step velocity is given by Equation 2.1 as expected.

2.1.2 Attachment-limited and diffusion-limited growth kinetics

In the previous section, the step and kink velocities of a growing crystal were discussed in terms of the adatom concentration directly next to the growing step edge. In this section, the factors that determine the resulting adatom concentration are discussed. Specifically, the relationship between the rates at which adatoms are supplied to the growing step edge and the rates at which they attach to the step edge are discussed. The interplay between these two rates define two distinct growth regimes: diffusion-limited and attachment-limited growth.

At steady-state, the diffusion of a surface adatom is expressed by Fick's first law, which says that the diffusion flux is proportional to the negative of the concentration gradient [95]

$$\mathbf{J}_d = -D_s \nabla c \quad (2.8)$$

where D_s is the surface diffusion coefficient. For random jumps and an attempt frequency independent of concentration, the surface diffusion coefficient is given by

$$D_s = \frac{1}{4} a_0^2 f_d e^{-\frac{E_d}{kT}} \quad (2.9)$$

where adatoms attempt to jump from one atomic site to another with frequency f_d and must overcome an energy barrier of E_d .

When an adatom reaches a kink site, it can attach to the kink. The rate of attachment determines the kink velocity. Equation 2.3 can be rewritten as $v_k = B_{a,k}(c^{ad} - c^{eq})$ where $B_{a,k}$ is the kinetic coefficient for attachment to a kink,

$$B_{a,k} = f_d d_n e^{-E_a/kT}. \quad (2.10)$$

By taking the ratio of the surface diffusion coefficient (Equation 2.9) to the kinetic coefficient for attachment (Equation 2.10) and assuming that $a_0 \approx d_n$ and $f_a \approx f_d$, one arrives at the so-called kinetic length [96, 97]

$$d_k = \frac{D_s}{B_a} \approx \frac{1}{4} a_0 e^{\frac{E_a - E_d}{kT}}. \quad (2.11)$$

The resulting growth regime depends on the relationship between the kinetic length and the average distance between step edges, l . In the limit where no attachment barrier exists, $E_a \approx 0$, $d_k \ll l$ and growth is diffusion-limited. In other words, as soon as an adatom reaches a kink at the step edge, it attaches immediately, and the growth rate depends on how quickly adatoms diffuse to the step edge. In this limit, the adatom concentration at the step edge is equal to the equilibrium value of the step edge, as depicted in Figure 2.2. In the limit where $E_a \gg E_d$, $d_k \gg l$ and the attachment-limited growth regime prevails ($d_k \geq 10l$ is considered reasonable to assume this limit [96]). In this regime, the rate of attachment is much slower than the surface diffusion rate; thus, surface diffusion quickly replaces adatoms after any attachment event. This relatively fast diffusion eliminates any adatom concentration gradients, resulting in a spatially-uniform adatom concentration between the growing step edges. In the intermediate regime where $d_k \approx l$ a hybrid situation emerges where concentration gradients exist near the step edges, but the adatom concentration next to the step edge is greater than the equilibrium value. These various situations are shown in Figure 2.2.

2.1.3 Kossel and non-Kossel growth

The previous discussion assumed that the species responsible for growth, those that attach to kinks, are single adatoms. This is the so-called Kossel crystal growth model [83]. Another

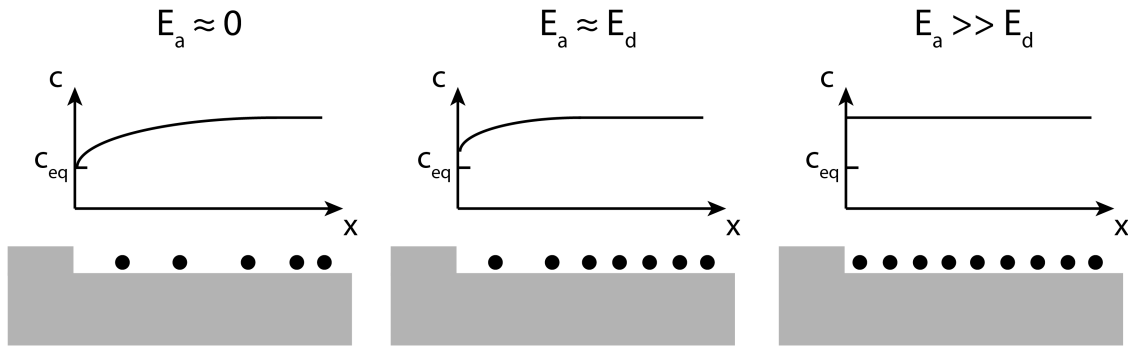


Figure 2.2: As the barrier for attachment to a growing step edge increases relative to the surface diffusion barrier, the adatom concentration next to the step edge increases and the diffusion gradient decreases.

regime of crystal growth is called non-Kossel, where the attachment species consists of more than one atom [83, 84] as shown in Figure 2.3. For an elemental solid, non-Kossel crystals have non-simple unit cells (i.e., unit cells other than BCC, FCC, or HCP) in which the ordering of the atoms result in non-equivalent positions within the unit cell [83, 84]. Since kinks advance by the addition of repeatable units, for non-Kossel crystals, this occurs by the addition of a unit cell composed of multiple atoms.

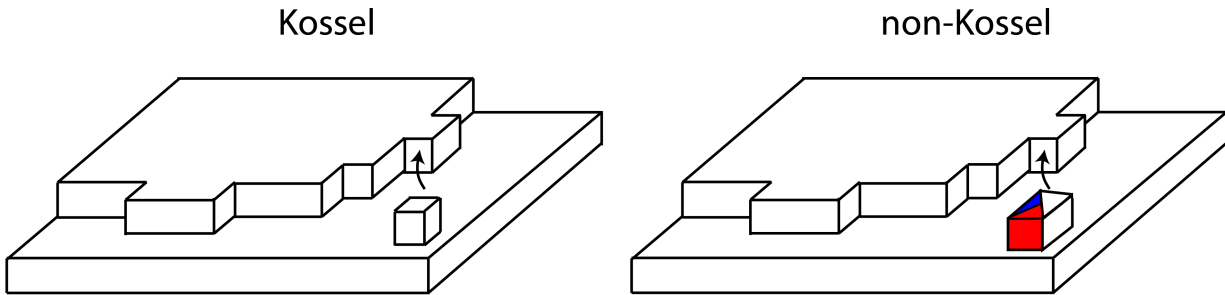


Figure 2.3: Kossel crystals grow by attachment of single adatoms ($n = 1$) whereas non-Kossel crystals have complex unit cells in which growth occurs by the addition of multi-atom clusters (e.g., $n = 3$ here).

Not surprisingly, the step velocity of a non-Kossel crystal depends differently on the adatom concentration than a Kossel crystal. Growth is driven by how far out of equilibrium the attachment species is. For non-Kossel crystals, it is driven by the density of clusters in the adatom sea relative to the equilibrium cluster density. The density of an n -atom cluster, c_n , depends exponentially on the energy difference between n isolated adatoms and

the energy needed to form an n -atom cluster, E_n [98]:

$$c_n = e^{\frac{n\mu}{kT} - \frac{E_n}{kT}} = \left(\frac{c^{ad}}{c^{eq}} \right)^n e^{-E_n/kT} \quad (2.12)$$

where the adatom sea is assumed to be an ideal lattice gas with C chemical potential

$$\mu = kT \ln \left(\frac{c^{ad}}{c^{eq}} \right). \quad (2.13)$$

The step velocity is now proportional to how far out of equilibrium the density of these clusters are. In the high kink density limit, the step velocity from Equation 2.4 can be expressed as

$$v_s = a\rho_k P d_n (c_n - c_n^{eq}) = \left(\frac{2a}{b} \right) e^{-E_k/kT} f e^{-E_a/kT} d_n e^{-E_n/kT} \left[\left(\frac{c^{ad}}{c^{eq}} \right)^n - 1 \right] \quad (2.14)$$

or, when the prefactors independent of concentration are grouped into the kinetic coefficient, can be expressed as [61]

$$v_s = B \left[\left(\frac{c^{ad}}{c^{eq}} \right)^n - 1 \right]. \quad (2.15)$$

Here, the step-velocity is non-linear with the adatom concentration, and the non-linearity depends on the cluster size responsible for attachment to a kink.

Equations 2.14 and 2.15 assumed a high kink density along the growing step edge. If this is not the case, the step velocity can be generalized to include kink nucleation from the adatom sea. This requires determining the kink nucleation rate, J , in Equation 2.7 as a function of the adatom concentration. By assuming that kink nucleation occurs by a cluster of a single critical size, m , the above approach can be applied, that is, the rate of kink nucleation is proportional to how far out of equilibrium the density of the kink nucleation clusters is. Consider a step edge section with length equal to that of the cluster responsible for kink nucleation, d_m . The rate at which clusters attach depends on the energy barrier for attachment, $E_{a,k}$ and the density of m -atom clusters in the adatom sea,

$$J = \frac{f}{d_m} e^{-E_{a,k}/kT} e^{-E_m/kT} \left[\left(\frac{c^{ad}}{c^{eq}} \right)^m - 1 \right] \quad (2.16)$$

where E_m is the energy needed to form an m -atom cluster. Substituting Equation 2.16 for the kink nucleation rate and Equation 2.3 for the kink velocity into Equation 2.7, the step velocity as a function of adatom concentration for a non-Kossel crystal with kink nucleation from the adatom sea is given by

$$v_s = af \sqrt{\frac{d_n}{2d_m}} e^{-(E_a+E_{a,k})/2kT} e^{-(E_n+E_m)/2kT} \left[\left(\frac{c^{ad}}{c^{eq}} \right)^n - 1 \right]^{\frac{1}{2}} \left[\left(\frac{c^{ad}}{c^{eq}} \right)^m - 1 \right]^{\frac{1}{2}} + \left(\frac{2a}{b} \right) e^{-E_k/kT} f e^{-E_a/kT} d_n e^{-E_n/kT} \left[\left(\frac{c^{ad}}{c^{eq}} \right)^n - 1 \right] \quad (2.17)$$

In the limit that $E_k \gg kT$, the equilibrium kink density becomes negligible and the second term on the right hand side of the above equation goes to zero. In this limit, it is worthwhile to note that the kinetic barriers are now averages of the barriers for attachment of clusters to kink sites and those for attachment to nucleate kinks, E_a and $E_{a,k}$, and an average of the barriers for cluster formation in the adatom sea, E_n and E_m . If the cross terms of the quantities involving the adatom concentration are negligible, then

$$v_s \approx B_{J,nK} \left[\left(\frac{c^{ad}}{c^{eq}} \right)^{\frac{m+n}{2}} - 1 \right] \quad (2.18)$$

where $B_{J,nK}$ is the kinetic coefficient for the step velocity of a non-Kossel crystal and kink nucleation. Here, the non-linearity of the step velocity goes as $(m+n)/2$, and if the assumptions above are applicable, insight can be gained about the cluster sizes responsible for kink nucleation and kink advancement.

2.1.4 Crystal growth summary

This section on crystal growth focused on the kinetics of kink formation and what species attach to kinks. Emphasis was given on how the step velocity depends on the adatom concentration for the various growth regimes. It is specifically noted that a non-linear step velocity can be manifested from two distinct mechanisms: growth in which kink nucleation is slow and kinks nucleate by attachment of multi-atom clusters to the step edge, or by the attachment of clusters to kinks of a highly kinked surface. Of course, the most general case occurs when both mechanisms occur: kink-nucleation by cluster attachment and kink-advancement by cluster attachment (Equation 2.17). In the latter case, drawing conclusions from the step velocity as a function of adatom concentration becomes significantly more challenging.

2.2 Graphene on Ir(111): A model system

This section reviews the relevant literature of graphene on Ir(111) and highlights the characteristics that make graphene on Ir(111) a model system to study.

2.2.1 Literature review of graphene on Ir(111)

Iridium is a transition metal with a face-centered cubic crystal structure with lattice parameter of 3.840 Å and a melting temperature of 2719 K [99]. Iridium is catalytic to the breakdown of hydrocarbons (ethylene fully dissociates at 820 K [2]) and thus can be used to grow graphene by chemical vapor deposition. Carbon can be easily removed from the Ir surface by oxidation, forming CO which desorbs from iridium at 600 K [100], as well as oxygen above 1300 K [101].

In hindsight, the first observation of graphene on Ir(111) was reported in 1976 [2], evidenced by the characteristic LEED patterns. The first investigations of the properties of graphene were by a Russian group, Rut'kov and Tontegode, in the 1980's and 1990's [3–5]. The Russian group recognized that an ordered, 2D carbon layer (so-called ‘monolayer graphite’ or ‘2D graphite films’) existed on many transition metal surfaces. They determined that the graphene film was weakly bound to the metal substrates and actively investigated intercalation of sub-monolayer films. A more recent investigation confirmed their interpretation and showed that R0 graphene is, on average, 3.4 Å above the Ir(111) surface [102]. The Russian group also showed that graphene island edges behave differently than the interior. They presented strong evidence that island edges are tightly bound to metal substrates [3–5], attributed to the strong in-plane, dangling bonds of the graphene layer at the island edge. This island edge-binding has been confirmed more recently [10, 103].

After the demonstration of graphene's electronic properties in 2004 [1], a new research undertaking of graphene on transition metals began. Graphene on Ir(111) was one of the first substrates investigated. Early STM studies demonstrated the superior structural quality of graphene on Ir(111) [11]. Notably, it was shown that growth proceeded uninterrupted, i.e., defect-free, over Ir substrate steps [63] illustrating that the domain size would not be limited by the substrate terrace width.

LEEM studies of graphene on Ir(111) showed that discrete domains did exist due to the nucleation of various in-plane rotational variants relative to the substrate lattice. Six in-plane rotational variants have been observed: R0, R14, R19, R22, R26, and R30 [21, 67]. As with graphene on many metal substrates, it quickly became clear that the quality of the final film would significantly depend on the nucleation characteristics: the degree of domain misalignment and the nucleation density, as discussed in Chapter 1.

LEEM also showed that graphene growth on Ir(111) is attachment-limited [21], which is also observed for graphene on Ru(0001) [61], Pt(111) [13], Pd(111) [104], Cu(100) [73], and Cu foils [23]. Attachment-limited growth was determined by LEEM reflectivity measurements during growth. The use of this technique shows that adatom concentrations are relatively large, even at equilibrium. It was also estimated that C adatoms are tightly bound to the Ir substrate, on the order of 7 eV [21].

In-depth studies of the growth kinetics of graphene on metals have been limited to Ru(0001) and Ir(111). In the case of Ru(0001), LEEM was used to show that the step velocity is non-linear with the C adatom concentration and it was determined that a 5-atom C cluster was the attachment species [61]. In the case of Ir(111), the growth rate of R0 islands is non-linear with the carbon adatom concentration [21] as well. However, the investigation was not as extensive as the case of Ru(0001) because the adatom concentrations on Ir(111) are less than Ru(0001), making the attachment-species-size experiments more challenging. Thus, the specific growth mechanism or cluster size responsible for growth was not deduced. Another interesting result is that the growth rate of R30 is faster than R0 on Ir(111) [21]. The growth rate also depends on graphene orientation in the case of Pt(111) as well [13]. No explanation has been presented to explain this growth behavior with orientation.

2.2.2 Moirés and incommensurate films

Graphene is not lattice-matched to Ir(111). The in-plane lattice parameter of graphite is 2.461 Å [27] and the Ir atom spacing is 2.715 Å [99]. Because vdWE has weak bonding between the film and the substrate, the film does not adopt the lattice spacing of the substrate. Thus, both the graphene and Ir lattices maintain their approximate lattice spacings. This results in a periodic moiré structure as shown in Figure 2.4, an effect similar to the beat frequency in interferometry. The R0 moiré on Ir(111) has a periodicity of 25.3 ± 0.4 Å and forms a 9.32×9.32 superstructure [11]. Because the superstructure is not an integer number of unit cells, translational symmetry is broken and the system is termed incommensurate.

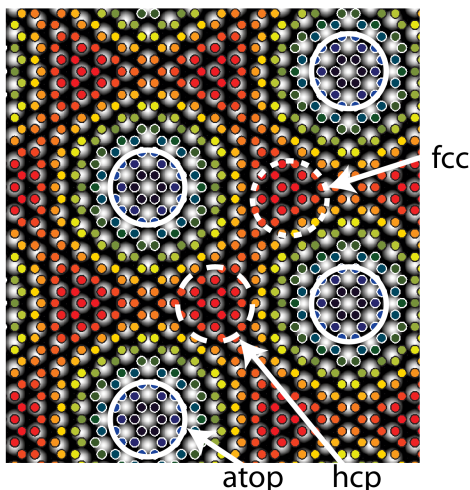


Figure 2.4: The moiré positions of graphene on Ir(111). The filled white circles represent Ir atoms, filled colored circles are C atoms in the graphene sheet. The nomenclature is based on where the C-ring is centered relative to the substrate atoms. ‘atop’: ring is centered directly above a surface Ir atom. ‘hcp’: the ring is positioned such that it follows ABA stacking (hexagonal close-packed or hcp), i.e., the ring is directly above an Ir atom in the second layer of the substrate. ‘fcc’: the ring is positioned such that it follows ABC stacking (face-centered cubic or fcc), i.e., the C-ring is centered directly above an Ir atom in the third layer below the surface. The colors represent relative heights: red is close to the substrate, violet is further away. Actual heights are discussed in Section 5.8. Figure provided by K. Thürmer.

Strictly speaking, the moiré is an optical effect resulting from the different periodicities of the film and substrate. However, for graphene on Ir(111) and metals in general, the moiré results in a physical corrugation of the graphene film. This corrugation has been observed in STM [11, 20, 105, 106], He atom diffraction [105], LEED [11], X-ray diffraction [107], and is consistent with density functional theory results [102]. The reason for this corrugation is that the preferred distance of the graphene sheet from the substrate varies locally, depending

on the lateral position of the C atoms with respect to the substrate (whether the C atom is at an atop position, a threefold hollow site, etc. as seen in Figure 2.4). To maximize its binding to the substrate, the graphene sheet flexes slightly in an effort to follow a contour of minimum C-Ir potential. Corrugations are not limited to graphene. Other 2D materials on metal substrates exhibit corrugations as well, including MoS₂ on Au [108] and Cu(111) [109] and hexagonal-BN on Pt(111) [110].

2.2.3 Summary

The growth characteristics of graphene on Ir(111) (superior structural quality, rotational variants, attachment-limited kinetics, non-linear velocity) are shared by graphene on many other substrates. Furthermore, the properties of iridium allow for high-throughput experimentation: easy removal of graphene by oxidation and flashing to desorb oxygen, and an unchanging surface (i.e., no step-flow) due to the high melting temperature relative to temperatures where graphene is typically grown (750-900 °C). Coupled with the fact that adatom concentrations are large enough to be measured, graphene on Ir(111) is a model system to investigate the orientation-dependent van der Waals epitaxy of graphene.

Chapter 3

Experimental Techniques

The main experimental technique used in this dissertation was low-energy electron microscopy and low-energy electron diffraction (LEED). A significant advantage of LEEM is real-time imaging of *in-situ* dynamic processes on surfaces with nanometer resolution. This includes phase transitions, such as vapor phase growth (CVD, PVD). Section 3.1 discusses the basics of LEEM, the instrumentation, and the advantages it provides in studying thin film growth. Specific attention is given to estimating adatom concentrations on surfaces using LEEM reflectivity. Section 3.2 discusses LEED in context of the LEEM instrument along with relating LEED and LEEM images to characterize island morphology.

3.1 Low-energy electron microscopy (LEEM)

Low-energy electron microscopy is an imaging technique that is sensitive to surfaces. It was conceived and developed by Ernst Bauer. Historically, LEEM lagged other electron microscopy techniques in implementation and development, specifically transmission electron microscopy (TEM), for two major reasons [111]: (i) glass-based vacuum systems provided insufficient UHV conditions and did not enable the typical surface-cleaning techniques required for surface imaging, and (ii) a misunderstanding in the aberrations of the objective lens led the electron microscopy community to conclude that the resolution of LEEM was much worse than in reality. Not until the mid-1980's were quality LEEM images produced; however, significant advances have been made in the past 20 years [112]. Below, the basic operation and imaging modes of LEEM are discussed. The LEEM used in this work was an Elmitec model at Sandia National Laboratories in Livermore, CA.

3.1.1 Introduction

LEEM is a method that images elastically backscattered electrons with energy less than 100 eV and typically less than 20 eV from a surface in ultra-high vacuum. The technique produces a beam of high-energy electrons, typically 15 keV to 20 keV, that is deflected onto

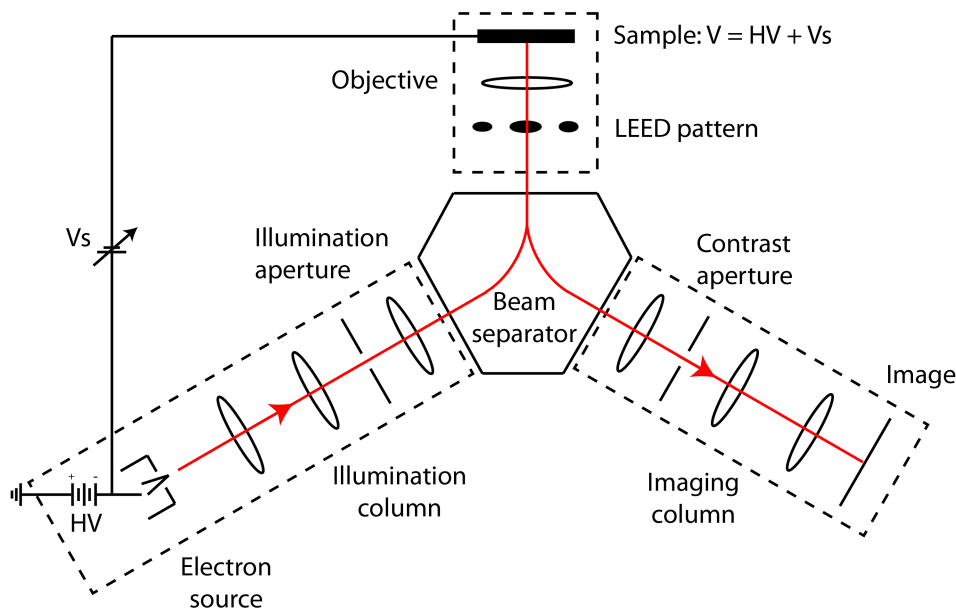


Figure 3.1: Schematic of a low-energy electron microscope. Filament is negatively biased at a high voltage (15 kV - 20 kV). The illumination column contains condenser lenses (ovals) that produce a parallel beam. The beam separator is made of magnetic dipoles that separate the incident and image beams. The sample is negatively biased, which slows the electrons down to low energies, set by V_s . The lenses in the imaging column produce the pre-determined FOV, which is displayed on a phosphor screen. Instrumentation is discussed further in Section 3.1.2. Figure modeled after [112].

the sample. The sample is negatively biased, which slows the incident electrons down to the desired imaging energy (also called ‘start voltage’ or V_s). This is a so-called cathode-lens [111, 113]. Elastically backscattered electrons are then accelerated by this same electrostatic field and pass through a beam-splitter. This beam-splitter is unique to LEEM and is required to separate the incident and imaging beams [111, 113]. The electrons are then projected onto a phosphor screen that is recorded by an external camera. Imaging field-of-view (FOV) can range from 1 μm up to 100 μm and image acquisition rates are on the order of one frame per 100 ms to tens of seconds, limited only by the electron flux [112]. A schematic of the Elmitec LEEM is shown in Figure 3.1.

At the low electron energies used in LEEM, the atomic backscattering cross section is large enough to form an image at typical electron gun emission currents [113]. To understand how LEEM images are formed, elastic scattering interactions of electrons with a sample is considered. The interaction with low-energy electrons is more challenging to predict than high-energy electrons in, for example, TEM, where energies are on the order of 80-200 keV [114]. The velocity of an electron is proportional to the square root of its energy. Thus, high-energy electrons in TEM travel quickly and a valid approximation is to assume that

the electron does not disturb the atoms in the specimen; thus, the ground state is used to model the interaction with the electron. Further, it is assumed that the electron undergoes a single scattering event, the so-called first Born approximation [111]. In contrast, low-energy electrons travel much more slowly and have a much longer interaction time with the substrate atoms. To understand the scattering, an excited state of the substrate atom must be considered. Furthermore, low-energy electrons can undergo multiple scattering events. These multiple scattering processes from excited states are much more challenging to accurately model [111].

Nonetheless, the Born approximation can be applied as a first-order approximation. In this approximation, the intensity depends on the unoccupied band structure of the surface [111, 113], and resultingly depends on the energy of the incident electrons. At energies where the density of states is low, the electrons are more readily reflected and the intensity will be higher than at energies where many states exist. In contrast, if an electron enters the sample in one of the free electron states, it can then interact with the sample atoms, increasing the likelihood of an inelastic scattering event to occur. It is this strong attenuation of low-energy electrons by inelastic scattering that produces the high sensitivity to surfaces in LEEM [111]. Nonetheless, the intensity of elastically backscattered electrons at low-energies can be high, on the order of 20% of forward scattering [113].

Contrast in LEEM can come from a number of sources. The main source, and the main one employed in this dissertation, is diffraction contrast. Here, the specular beam is imaged and contrast is due to a difference in the (00) structure factor between the two phases, i.e., one phase diffracts more strongly than the other [114]. Contrast is also observed in another imaging mode called mirror electron microscopy (MEM). Here, the sample is at a voltage slightly more negative than that of the incident electrons and all electrons are reflected without interacting with the surface. Contrast in MEM is due to variations in the local electric field, e.g., due to topography differences or to work function differences [112]. A third contrast mechanism is interference contrast. Here, destructive interference between the electron wave fields decrease the intensity. This is observed at substrate steps where the height difference provides the difference in electron path length required for the partial destructive interference [113].

3.1.2 LEEM instrumentation

LEEM uses many pieces of hardware that are common on transmission electron microscopes, including a filament to produce an electron beam, electrostatic and magnetic lenses to manipulate the electrons, and various apertures. This section discusses these components and those that are unique to LEEM.

There are three typical filaments used as an electron source: thermionic, field-emission, and photoemission. The most common emitter used is the LaB₆ thermionic emitter [112]. It has a low workfunction (2.7 eV), is relatively inexpensive, and has a long lifetime [114]. Its drawback is an energy spread of approximately 0.6 eV [112], which has implications on resolution, discussed below. A cold field-emission emitter can reduce the energy spread

to approximately 0.25 eV due to the absence of a thermal energy spread and improve the resolution. Its drawbacks include ultra-high vacuum (UHV) requirements to prevent ions of residual gas atoms damaging the filament and a shorter lifetime [114].

The illumination column contains a number of condenser lenses that produce a demagnified image of the source at the objective back-focal plane [112]. This parallel beam of electrons illuminates an area, the FOV, from 1 μm up to 100 μm . An illumination aperture can limit the illuminated area down to 0.2 μm and is used for selected-area diffraction [112].

The objective lens consists of two parts. The first is an accelerating lens that slows down the incident electrons and subsequently accelerates the electrons reflected at the surface. Secondly, a focusing component exists that forms a magnified image of the reflected electrons [112]. The LEED pattern forms at the back-focal plane of the objective lens. The objective lens contains the main resolution-limiting aberrations, discussed below.

Because the imaging electrons are reflected from the surface, they follow the same path as the incident electrons. This requires a beam separator to split the two beams into their respective lens columns. The simplest scheme is a magnetic dipole. Most modern-day LEEM's use an array of magnetic dipoles to split the beams [112].

The imaging column contains lenses to image the pre-determined FOV. A contrast aperture is also contained in the imaging column at the transfer lens. Typically, e.g., in TEM, the contrast aperture is placed at the back-focal plane. However, for LEEM this would obstruct the illumination of the sample. Thus, placement in the imaging column allows one to image the (00) beam or to perform dark-field imaging without obstructing the illumination of the sample.

3.1.3 LEEM resolution

The main limits to the resolution are the chromatic and spherical aberrations of the objective lens. Both aberrations are inversely proportional to the strength of the electrostatic field between the sample and the objective lens [115]. In practice, this field strength is limited to 10-20 keV/mm; higher field strengths result in ionization and arcing between the sample and the objective [112]. Thus, any improvements in resolution requires eliminating the electron beam energy spread or correcting the aberrations. For standard electron optics (not aberration-corrected) with a LaB₆ filament, typical resolutions are on the order of 10 nm [115]. By using a cold field-emission filament, the chromatic aberration can be significantly reduced and the resulting resolution can reach less than 5 nm [115].

More recently, aberration-corrected lenses have been designed for LEEM. The main effort is driven by Rudd Tromp of IBM on the IBM/Specs LEEM [115]. The most successful approach has been the use of electron mirrors. These mirrors are electrostatic lenses that reflect electrons and their advantage is that they have opposite chromatic and spherical aberrations than that of the objective lens [112]. Current aberration-corrected LEEM's have reached a resolution of 2 nm, with further improvements to 1 nm possible [115].

3.1.4 Film growth in LEEM

One of the main advantages of LEEM is the ability to produce a real-space, real-time image of film growth. Films can be grown by physical vapor deposition from sources inside the chamber or by chemical vapor deposition by introducing gasses into the chamber. Imaging can be performed up to pressures of 1×10^{-6} torr [112]. Large areas of the sample can be observed due to the range of FOV's and the ability to move the sample with the sample manipulator. Sample temperature is controlled by electron bombardment from a tungsten filament underneath the sample, and can range from liquid nitrogen (77 K) to over 1770 K. These characteristics provide many options for studying film growth and phase transitions.

Selected-area LEED is also very advantageous in LEEM. Regions of interest (down to 0.2 μm) can be selected by use of the illumination aperture from which a LEED pattern is formed. A dark-field condition can be created where only one diffracted beam is used to create the resulting real-space image, resulting in an image that spatially shows where the specific phase is present.

3.1.5 Quantifying adatom concentrations in LEEM

Recently, LEEM has been used to quantify adatom concentrations on surfaces. Because low-energy electrons are sensitive to the surface, it is not surprising that adatoms can sufficiently scatter electrons and produce changes in reflectivity. The technique works by quantifying changes in the intensity of the specular beam due to the presence of surface adatoms, similar to thermal He scattering [116]. The technique in LEEM provides the significant advantage of determining adatom concentrations *spatially*. The first use of LEEM to measure adatom concentrations was performed for Ag adatoms on W(110) [87]. A clean surface is prepared and the specular beam is used to form the image and the surface intensity is monitored. Adatoms are then deposited at a constant flux. In the Ag/W(110) case, a linear decrease in intensity was initially observed, indicating that the scattering of each adatom is independent of the other adatoms [87]. The intensity decreases because the adatoms scatter the electrons outside the isolated specular beam, and was confirmed experimentally [117].

Carbon adatoms on Ru(0001) and Ir(111) similarly affect LEEM reflectivity [20, 61]. The quantification of C adatom densities on these metals was performed in the following way [20, 61]. First, the substrate was cleaned to ensure a C-free surface. A constant power was applied to a C rod for evaporation, conditions in which a constant flux was assumed and a linear decrease in the reflectivity was observed. The slope of this decrease depended on the power applied to the C rod, i.e., the C flux. C was deposited at constant power until graphene islands nucleated and grew to ~ 0.3 ML. The total amount of C deposited was determined by measuring the area of graphene islands over a large area (500 μm x 500 μm) and accounting for the adatom sea.

In order to quantify the reflectivity change with adatom concentrations, a proportionality factor needs to be determined. The rate of change of the intensity is proportional to the

flux,

$$\frac{d(I/I_0)}{dt} = -\lambda F \quad (3.1)$$

where I is the intensity, I_0 is the initial intensity, F is the flux, and λ is the proportionality factor. The flux is determined by dividing the total C deposited, as discussed above, by the total time of deposition. The intensity rate of change is experimentally determined, and thus λ is easily determined. The resulting adatom concentration is given by

$$c = \frac{1}{\lambda} \frac{I_0 - I(t)}{I_0}. \quad (3.2)$$

The sensitivity of the adatom concentration determined by LEEM reflectivity changes is on the order of 10^{-4} monolayers [61, 87].

Because the reflectivity is sensitive to the incoming electron energy, λ is applicable to the precise start voltage used while performing this calibration. To determine which start voltage to use, the reflectivity of the surface can be compared before and after deposition of adatoms. In this method, images are recorded as a function of the start voltage for a clean surface and then again with adatoms on the surface. By plotting the reflectivity as a function of the start voltage, the energies at which the reflectivity is most sensitive to the adatoms can be determined by simple comparison. For C on Ir(111), $\lambda = 0.189$ at 17.0 eV [21].

3.2 Low-energy electron diffraction (LEED)

When the incident electron beam impinges on an ordered surface, it diffracts. The wavelength of low-energy electrons is on the order of 1-2 Å and thus are suitable for diffraction of crystalline solids. Because the low-energy electrons do not penetrate deeply into the sample, LEED probes the two-dimensional periodicity of the substrate surface. As mentioned previously, low-energy electrons undergo multiple scattering events. This results in much more complex diffraction patterns than those seen in TEM and X-ray diffraction. This is especially true for surfaces that undergo complex reconstructions [118]. For example, a superstructure diffraction spot can be displaced in k -space by a second scattering event of the first-order periodicity of the substrate. This results in a superstructure LEED spot near the (00) and also near the (01), for example R0 graphene shown in Figure 3.2. Oftentimes, these reconstructions are made up of domains of various in-plane rotation angles relative to the substrate, resulting in even more complex LEED patterns [118]. In theory, any combination of reciprocal lattice vectors can produce a diffraction spot; however, in practice, only the shortest combinations are typically observed [118]. Selected-area diffraction within LEEM has helped improve the interpretation of LEED patterns by isolating small areas (in contrast to LEED experiments performed before the realization of LEEM).

In X-ray diffraction, the intensity of the allowed diffracted beams gives significant information on the atomic arrangement within the unit cell [118]. This is not true for LEED, and

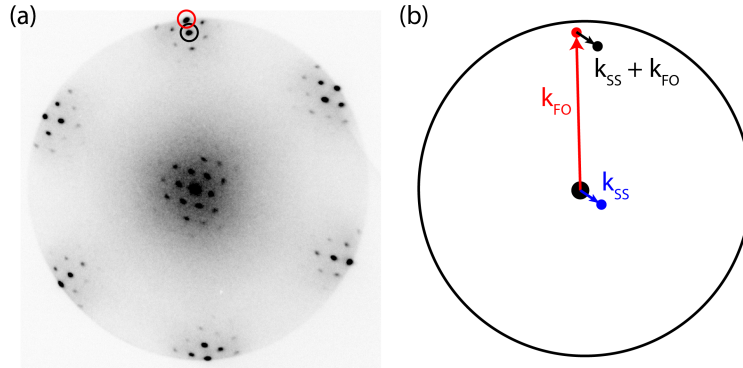


Figure 3.2: (a) LEED pattern of R0 graphene on Ir(111) exhibits multiple superstructure spots. The first order graphene and Ir(111) spots are highlighted by the red and black circles, respectively. (b) The spots surrounding the first-order spots can be understood by multiple elastic scattering events. The satellite spots around the first order spot are a summation of the reciprocal lattice vectors for the first-order diffraction and superstructure diffraction, k_{FO} and k_{ss} , respectively.

is again due to the multiple elastic scattering of low-energy electrons. To gain information on atomic positions, a dynamical scattering treatment must be used. Information can be gained by performing I-V analysis of the LEED pattern, i.e., recording the spot intensities as the electron energy is varied [119].

3.2.1 Determining the zigzag orientation for graphene islands

The shapes of islands and growth kinetics are intimately linked. Understanding how the island shape corresponds to important crystallographic directions is important. For example, during growth, the slowest growing edges will prevail and understanding the structure of these edges is important in characterizing the growth mechanisms. For graphene, two noteworthy crystallographic directions are those along the ‘zigzag’ and the ‘armchair’ directions. Using LEEM and LEED, the orientation of these directions can be plotted on the real-space LEEM image for a given graphene island orientation. As one sees in Figure 3.3(a), the graphene reciprocal lattice vectors point to the zigzag termination in real-space. Thus, by placing the LEED pattern on top of the real-space LEEM image (Figure 3.3(b)), the vectors from (00) to the first-order LEED spots are perpendicular to the zigzag termination.

However, because the Elmitec LEEM uses magnetic lenses, the electrons rotate between the back-focal plane, where the LEED pattern forms, and the image plane of the phosphor screen. This rotation must be accounted for in order to compare the LEED and LEEM images. This can be determined by tilting the sample in the x- or y-direction and recording how the LEED pattern shifts. The difference in the direction of the LEED shift compared to the real-space LEEM shift is equal to the net rotation angle. For the Elmitec LEEM

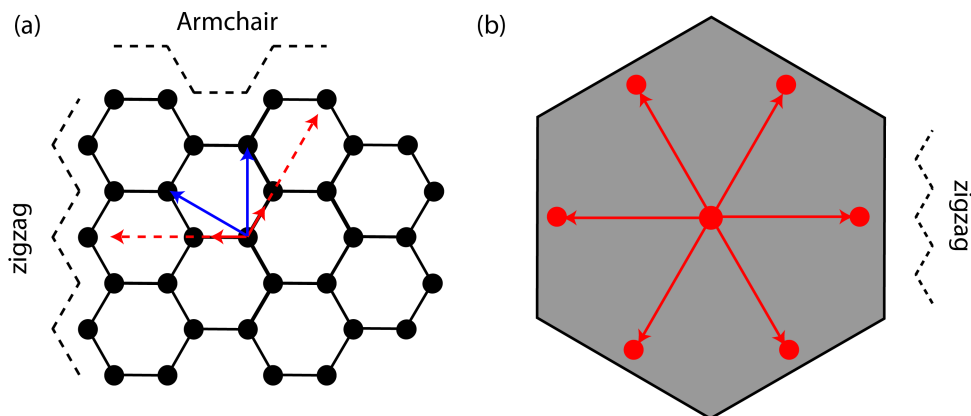


Figure 3.3: (a) The graphene honeycomb with lattice vectors (blue) and reciprocal lattice vectors (red); dashed arrows are to assist the eye. The reciprocal lattice vectors are perpendicular to the real space zigzag termination. The external dashed lines represent the zigzag and armchair directions for the graphene lattice. (b) If an island has zigzag termination, its LEED pattern would be positioned such when the electron rotation between the back-focal plane and the image plane is accounted for.

used here, this was previously performed and the rotation was determined to be 63° counter-clockwise [120], i.e., when the LEEM image is rotated by 63° counter-clockwise, it can be directly compared to the LEED pattern.

Chapter 4

Orientation-dependent growth mechanisms of graphene on Ir(111)

The growth mechanisms of graphene and two-dimensional materials are not well understood. Within the attachment-limited growth regime (Ir(111) [21], Ru(0001) [61], Pt(111) [13], Pd(111) [104], Cu(100) [73], and Cu foils [23]), only growth on Ru(0001) has been extensively characterized [61] and was the first LEEM study in which monitoring the adatom concentration in real-time was used to investigate growth kinetics. Significant advances in the understanding of graphene growth were made, including a proposed growth mechanism that involves C clusters as the attachment species, specifically a 5-atom cluster [61]. Significant questions still remain, however, including precisely how these C-clusters are involved in growth.

Graphene on Ru(0001) has only a single rotational variant, R0. As discussed in Chapter 1, graphene on other substrates tend to have various in-plane rotational variants, which can exhibit different growth rates [13, 21]. In this chapter, LEEM is used to investigate the growth mechanisms of graphene rotational variants on Ir(111). By analyzing LEEM images, it is shown that the island shape also depends on orientation. The growth kinetics of rotational variants are investigated by simultaneously correlating island edge morphology, growth rate, and the C adatom concentration. Fundamental insight into the growth mechanism, the attachment species, and the source of the different growth behaviors is given.

Section 4.1 discusses a method for determining the orientation of graphene rotational variants using LEED with improved accuracy. Section 4.2 presents a technique used to quantifiably distinguish graphene island shapes. Based on these results, the growth kinetics of R0 and rotated graphene domains are presented in Section 4.3, along with a discussion of the different growth mechanisms and their relation to the edge binding strength of the graphene island to the Ir substrate. Next, the analysis for determining the size of the attachment species responsible for growth is presented in Section 4.4. A summary and the significance of these findings are discussed in Section 4.5.

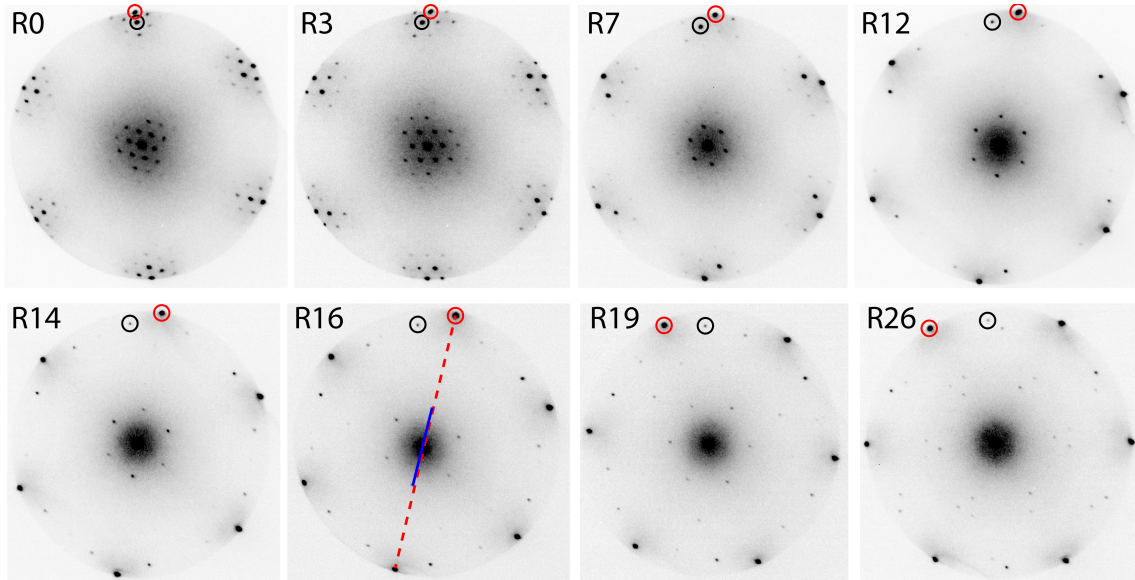


Figure 4.1: LEED patterns of graphene rotational variants on Ir(111). The red and black circles highlight the first-order graphene and Ir spots, respectively. The R16 LEED pattern shows representative length measurements of superstructure (blue line) and first-order graphene diffraction spots (dashed red line).

4.1 Assigning graphene island orientations: LEED analysis

Six rotational variants have been reported for graphene on Ir(111): R0, R14, R19, R22, R26, and R30 [20, 67]. The nomenclature adopted here is such that the number following the letter ‘R’ indicates the degree of rotation from the Ir(111) lattice. At times it is necessary to denote the sense of rotation, clockwise or counterclockwise, relative to the Ir(111) LEED spots, denoted by (+) or (-), respectively. For example, R14⁺ and R14⁻ implies a rotation of 14° clockwise and 14° counterclockwise, respectively. In addition to R0, R14, and R19, rotations of R3, R4, R7, R8, R9, R11, R12, R16, and R20 were observed. Select LEED patterns are shown in Figure 4.1. The moiré superstructure spots change significantly with island orientation.

Angles measured from LEED patterns are estimated to be accurate to $\pm 2^\circ$. However, small changes in the graphene rotation result in large changes in the moiré superstructure spots [11]. The changes in the moiré are used to improve the estimated accuracy to $\pm 0.5^\circ$. The distance between each pair of moiré superstructure LEED spots was measured (blue line, Figure 4.1) and normalized by the distance between the corresponding pair of first-order graphene LEED spots (red, dashed line). This ratio was computed for the three pairs of spots per each LEED pattern and then averaged together. Over 47 LEED patterns were measured and orientations were assigned based on this ratio. The assigned angles were

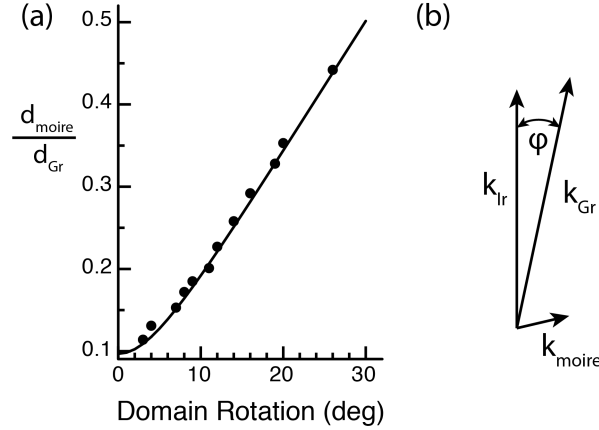


Figure 4.2: (a) Average of the measured ratio of the separation distance between moiré LEED spots and the first-order graphene LEED spots as a function of the misorientation between the graphene domain and the Ir(111) lattice. Solid line is the expected ratio. (b) As the misorientation angle increases, the length of the moiré k -vector increases.

rounded to the nearest whole number. The average of the ratios for each rotation angle are plotted as function of the rotation angle in Figure 4.2(a). The standard deviation of the averaged ratios was less than 0.01.

The expected ratio between the moiré spots and first-order graphene spots can be estimated based on a simple vector model. Figure 4.2(b) illustrates the moiré k -vector, k_{mo} , associated with a graphene domain rotated by an angle ϕ with respect to the Ir(111) lattice, where $k_{mo} = k_{Gr} - k_{Ir}$. For a frame of reference in which the origin is at the (00) LEED spot and the y -axis goes through an Ir(111) first-order LEED spot, the magnitude of k_{mo} is

$$\|k_{mo}\| = [(d_{Gr}\sin\phi)^2 + (d_{Gr}\cos\phi - d_{Ir})^2]^{1/2} \quad (4.1)$$

where d_{Gr} and d_{Ir} are the magnitudes of the graphene and Ir(111) k -vectors, respectively, and are inversely proportional to the repeat distance of C atoms in the graphene sheet and Ir atoms in the Ir(111) plane, respectively. For R0 graphene on Ir(111), the C repeat distance is $2.452 \pm 0.004 \text{ \AA}$ [11]. This can vary slightly as the moiré changes, where the graphite in-plane lattice parameter of 2.461 \AA [27] is an upper limit, an error of less than 0.4%. The nearest-neighbor distance of Ir atoms in the Ir(111) plane is 2.715 \AA [99]. The expected ratio as a function of ϕ is given by

$$\frac{2d_{mo}}{2d_{Gr}} = \left[1 + \left(\frac{d_{Ir}}{d_{Gr}} \right)^2 - 2 \frac{d_{Ir}}{d_{Gr}} \right]^{1/2} \quad (4.2)$$

where d_{mo} is the magnitude of k_{mo} . This ratio is plotted with the experimental data in Figure 4.2(a). There is excellent agreement between the experimental and expected ratios.

4.2 Island shape analysis

Growth kinetics and resulting island shapes are linked. For example, diffusion-limited growth typically results in dendritic islands, whereas attachment-limited growth maintains compact islands. In general, the slowest growing island edges will prevail [121]. Understanding the atomic make-up of these low energy edges is important to fully understand the growth mechanisms. In this section, a method to quantify island shapes is presented. Specific emphasis is given to island edge orientations relative to the zigzag direction.

4.2.1 Method: Fourier transform of island shapes

In order to compare island shapes, an analysis based on the Fourier transform (FT) of the island shape was developed. The method is illustrated by applying it to defined shapes. In Figure 4.3(a), a circle and hexagon are shown, along with the result when their FT is taken. The FT of the circle is uniform in the polar angle about the center. However, the FT of the hexagon has bright streaks that are perpendicular to the hexagon edges. The real-space island image has a step-function intensity change that requires many frequency components in order to be modeled in the frequency domain. The components for a straight edge have a single orientation in the FT and add together, resulting in coherent streaks, whereas the rounded edges of the circle result in a diffuse intensity. The resulting FT was converted to an intensity plot by integrating the pixel values along the radius as a function of the polar angle, Θ , as shown in 4.3(b). The curves were normalized by subtracting the minimum intensity for each curve. For the circle, the FT intensity is relatively constant and featureless. The FT intensity for the hexagon exhibits peaks with large changes in magnitude.

4.2.2 Results

This FT method was applied to graphene islands grown between 750 °C - 900 °C. Graphene islands were nucleated on Ir(111) by exposing the heated substrate to ethylene gas (C_2H_4). The temperature was measured by a W-Rh thermocouple in contact with the substrate and confirmed by an external pyrometer. After nucleation, the islands were grown for approximately one minute, the ethylene was turned off, and the islands were allowed to come to equilibrium.

Figure 4.4(a) and 4.4(b) present LEEM images of representative graphene islands. The rotated island consists of multiple domains with different orientations relative to the Ir(111) substrate, identified by selected-area LEED, whereas R0 islands are single-domain. Figure 4.4(c) and 4.4(d) are thresholded LEEM images that highlight only the island shape. Differences in island shape are qualitatively apparent when compared to their respective zigzag terminations, which are denoted by the solid, exterior lines, i.e., a zigzag terminated edge would be parallel to the lines, their orientation determined by applying the analysis in Section 3.2.1. The rotated island has faceted edges near the zigzag, whereas the R0 island has more rounded edges that do not necessarily align with the zigzag. This distinction is

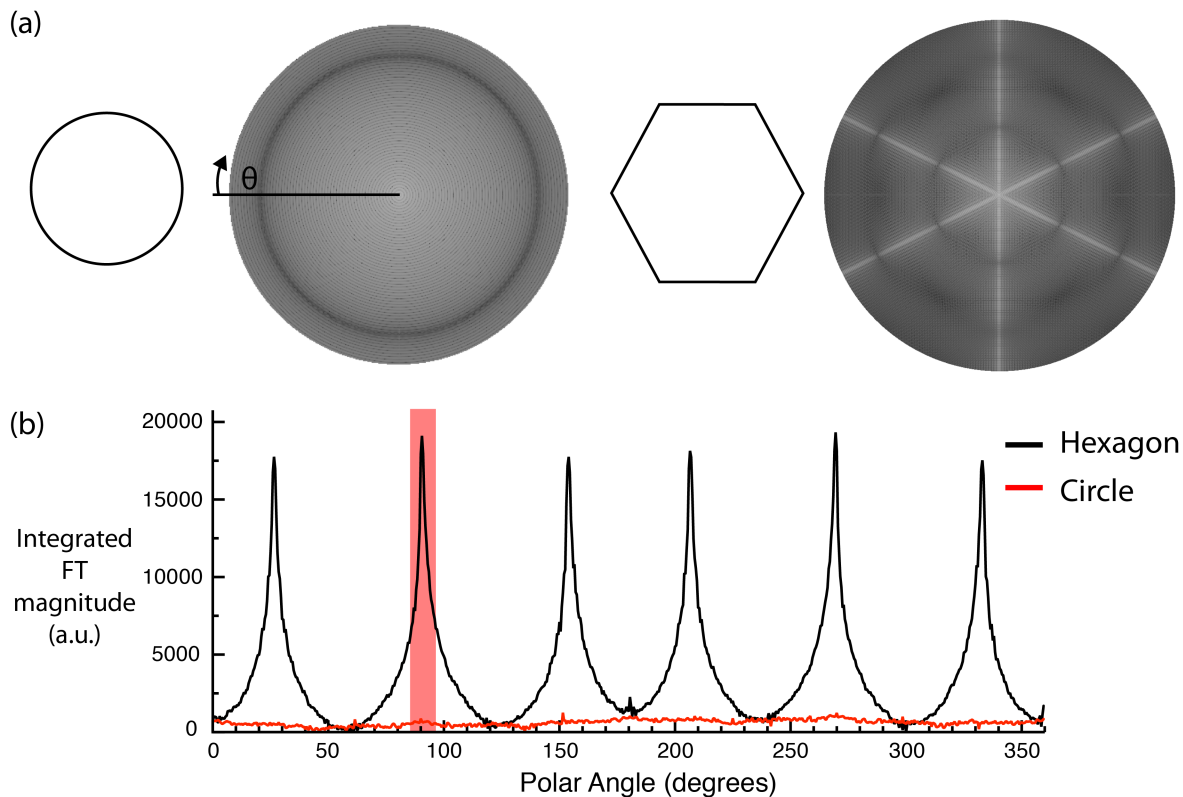


Figure 4.3: Fourier transform (FT) shape analysis applied to a circle and hexagon. (a) Shape is shown on the left and its corresponding FT is shown on its right. (b) FT intensity as a function of the polar angle. Due to the angular spread in the FT intensity peaks for the hexagon, only 50% of the total intensity is within $\pm 5^\circ$ of each peak center (red box).

quantified by taking the Fourier transform (FT) of the island images, shown in Figure 4.4(e) and 4.4(f). The rotated island FT has coherent streaks that emanate from its center with an orientation perpendicular to the island step edges, whereas the R0 island has more diffuse streaks in its FT. The FT was converted to an intensity plot by integration. In this form, the FT streaks are converted to peaks in the intensity plot shown in Figure 4.4(g). With the corresponding zigzag termination denoted by the vertical lines, one clearly sees that the rotated island has prominent peaks centered near the zigzag, whereas the R0 intensity has less prominent features that do not correlate with the zigzag.

To quantitatively compare island shapes, a metric is used in which the FT intensity was integrated $\pm 5^\circ$ about each known zigzag, summed, and then divided by the total integrated intensity. For the R0 island, 16% of its total intensity is within $\pm 5^\circ$ of its three zigzag terminations, whereas the rotated island has 41% within $\pm 5^\circ$ of its four zigzag terminations. After applying this FT analysis to 17 R0 islands and 12 rotated islands that spanned a temperature range of 750 °C to 900 °C, the results in Figure 4.4(h) clearly show that rotated

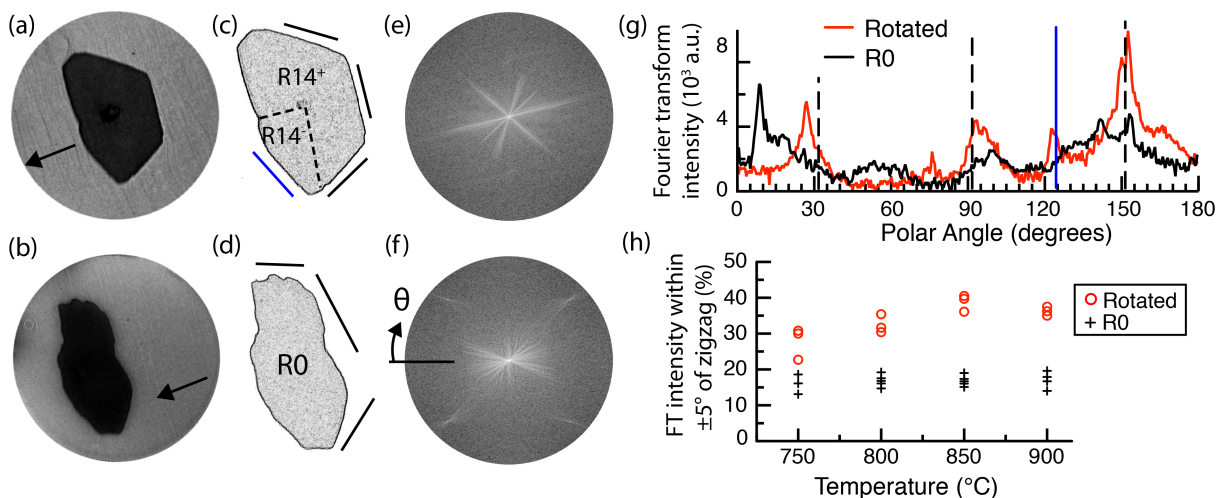


Figure 4.4: LEEM image of a rotated (a) and R0 (b) graphene island on Ir(111) at 850°C . The vertical lines that traverse the LEEM images are Ir step bunches. The arrows depict the uphill direction of the staircase of Ir steps. FOV = $30\ \mu\text{m}$. (c)-(d) Thresholded LEEM image of (a) and (b), respectively. Zigzag termination denoted by the solid, exterior lines. The dashed, interior lines in (c) denote a domain boundary; each domain was rotated 14° oppositely to the Ir substrate ($R14^+$, $R14^-$). (e)-(f) Fourier transform (FT) of the rotated and R0 island, respectively. (g) FT intensity as a function of the polar angle; vertical lines denote the corresponding zigzag (rotated domain polar angle was adjusted to align the zigzag terminations between R0 and $R14^+$; solid blue line corresponds to the zigzag for the single facet of $R14^-$). (h) Comparison of the FT intensity within $\pm 5^\circ$ of the zigzag for R0 and rotated islands.

islands have more of their perimeter within $\pm 5^\circ$ of the zigzag than R0 islands (See Appendix A.1 for analyzed island shapes).

Applying this $\pm 5^\circ$ integration procedure to the hexagon in Figure 4.3 results in only 50% of the total FT magnitude being accounted for, whereas one would expect 100% for a perfect hexagon. The difference is due to the relatively large full width at half max ($\sim 7^\circ$) of the peaks in Figure 4.3(b). This 50% maximum is taken to be an approximate upper bound for the graphene island analysis.

The percentage of the island perimeter within $\pm 5^\circ$ of the zigzag is independent of the island size for the islands measured here. As shown in Figure 4.5, the data for the rotated and R0 islands exhibited no dependence on island area.

Rotated islands typically consist of multiple domains, where misorientations of a few degrees are possible. Due to the angular spread in the peaks of the FT intensity, two closely spaced peaks can overlap each other. Furthermore, in the analysis of the FT intensity within $\pm 5^\circ$ of the zigzag, the peak tails should not be counted to ensure an accurate comparison with other islands that do not have overlapping peaks. Three analyzed islands met these

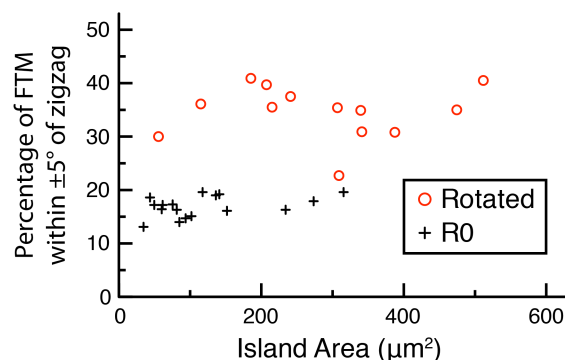


Figure 4.5: R0 and rotated island perimeter within $\pm 5^\circ$ of the zigzag exhibit no dependence on island area.

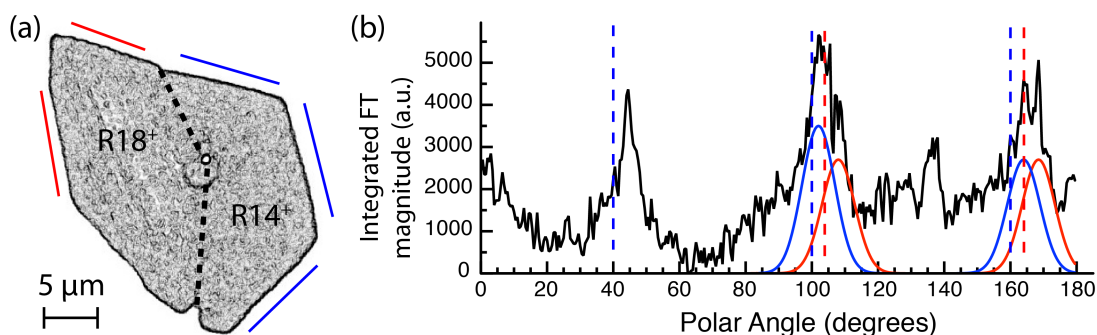


Figure 4.6: (a) 2-domain rotated island with internal domain boundary (dashed line) and corresponding zigzag orientations (external, solid lines). The domains are separated by only four degrees in their relative orientations (R18, R14). (b) The corresponding Fourier transform intensity for the island. Since only four degrees separate the corresponding zigzag orientations, denoted by the dashed, vertical lines, their respective peaks overlap each other. The individual contributions were determined using a multi-peak fitting analysis with Gaussian curves. Each individual curve (blue and red lines) were used to integrate within $\pm 5^\circ$ of the zigzag, i.e., the red curves were not included when integrating within $\pm 5^\circ$ of the blue zigzag lines, and vice versa.

conditions. Therefore, for these three islands, the intensity was fit using a Gaussian curve to separate the individual contributions, as seen in Figure 4.6. Although the peaks are not strictly Gaussian, a reasonable fit was obtained. The individual, fitted peaks were then used for the integration about its respective zigzag, preventing the peak tails of other orientations being counted. This small correction was on the order of a few percent.

4.3 Comparison of R0 and rotated island growth

To connect these differences in growth morphology with growth mechanisms, the growth velocities as a function of the C adatom concentration, c^{ad} , are determined and correlated with edge morphology. The experimental process used to grow the graphene islands is discussed, followed by the method to determine local edge velocities, and finally the results and analysis are presented.

4.3.1 Island growth experimental process

After nucleating graphene islands, selected islands were imaged while growing by further ethylene exposure. The LEEM base pressure was 1×10^{-10} torr and the maximum ethylene pressures used during growth experiments were $\sim 6 \times 10^{-9}$ torr (Figure 4.7(a)). The adatom concentration was determined by monitoring the reflectivity of the Ir surface as shown in 4.7(b) [21, 61, 87], and as discussed in Section 3.1.5. The C adatom concentration was modified by changing the ethylene pressure, i.e., c^{ad} was changed from the value where the islands were not growing (c^{eq}) via manipulation of the ethylene flow. The measured C adatom concentration had a standard deviation less than 0.0002 monolayers (ML), where 1 ML is equal to the density of C atoms in a graphene sheet on Ir(111). This was determined by computing the standard deviation of the reflectivity of the Ir surface with graphene islands at equilibrium. Reflectivity data were extracted using Interactive Data Language (IDL) software (Appendix B).

4.3.2 Measuring local edge velocities

LEEM images were recorded at one second intervals. Local step velocities were determined by measuring the island edge displacement with time. The LEEM images were loaded into ImageTool, a custom program written for Igor Pro (see Appendix B). All images were loaded into a single three-dimensional data set (x and y are the spatial coordinates of the LEEM image and the third dimension is time). ImageTool takes slices in one of these planes: $x - t$ or $y - t$, thus providing the perpendicular step edge displacement with time along a single chosen line (the LEEM images are rotated accordingly). The displacement data is then differentiated with time. The error in the velocity measurement was determined by measuring the fluctuation in pixel intensity of a stationary island edge. The velocity as a function of time is combined with the C adatom concentration as a function of time to produce the plots of velocity as a function of the C adatom concentration.

4.3.3 Results

Figure 4.8(a) and 4.8(b) present stacks of selected LEEM images taken over time that illustrate the growth of graphene islands at 850 °C. These stacks were created by removing the background (Ir substrate) of the LEEM images and then stacking them on top of each

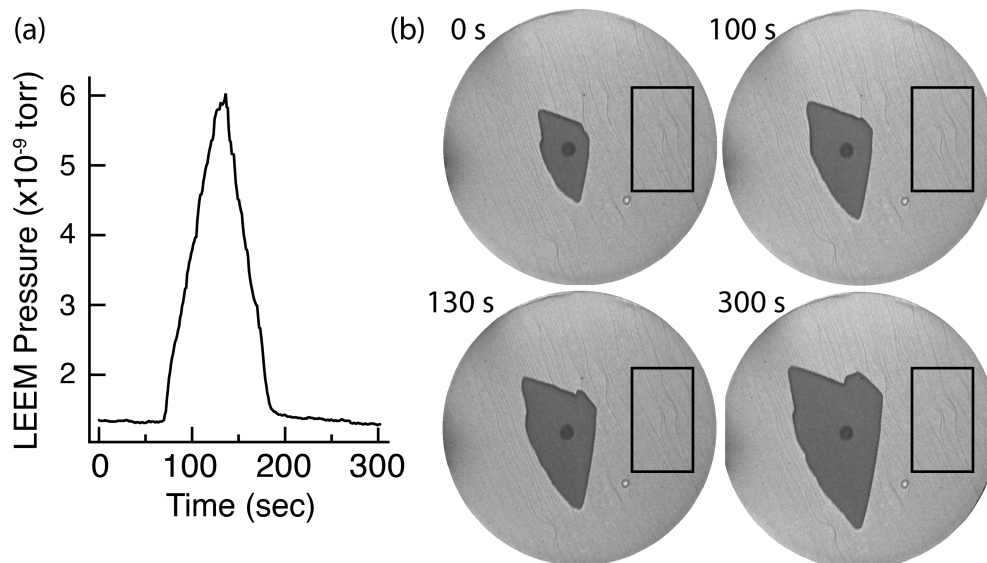


Figure 4.7: (a) Ethylene pressure during a typical graphene growth experiment. (b) Selected LEEM images taken from a growth experiment at 900 °C, FOV = 75 μm . The time is denoted in the upper-left corner. The box indicates the area of the Ir substrate that was monitored for reflectivity measurements.

other. Perhaps the most obvious difference between R0 and rotated islands is that the R0 growth is impeded in the uphill direction [21, 62]—seen by the compressed edge contours on the left side of the image stack in Figure 4.8(a)—while the uphill and downhill velocities of the rotated island in Figure 4.8(b) are comparable. To eliminate these substrate step effects on the following analysis, local velocities of R0 and rotated islands were determined in similar directions relative to the substrate steps and are shown in Figure 4.8(c) - 4.8(e).

The comparisons highlight three distinct differences between rotated and R0 islands and show that the velocity of rotated islands is not simply a function of the C adatom concentration. First, the rotated island velocities display hysteresis with the C adatom concentration: the step velocity was faster as the C adatom concentration was increased. This hysteretic behavior was confirmed for the other two facets of this rotated island as well as for three other rotated islands (see Appendix A.2). The hysteresis establishes that the growth rate is not simply a function of the C adatom concentration; instead, it also depends on how the C adatom concentration is varied. R0 islands did not exhibit hysteresis. Second, Figure 4.8(d) confirms that the growth velocity of rotated islands are relatively unaffected by uphill substrate steps in contrast to R0 islands. Third, as seen in Figure 4.8(e), the velocity of an edge for the rotated island significantly increased at a constant adatom concentration ($c^{ad} = 0.0065$ ML).

Further confirmation that the velocity is not simply a function of the C adatom concentration for rotated islands is gained by examining the image stack of the rotated island

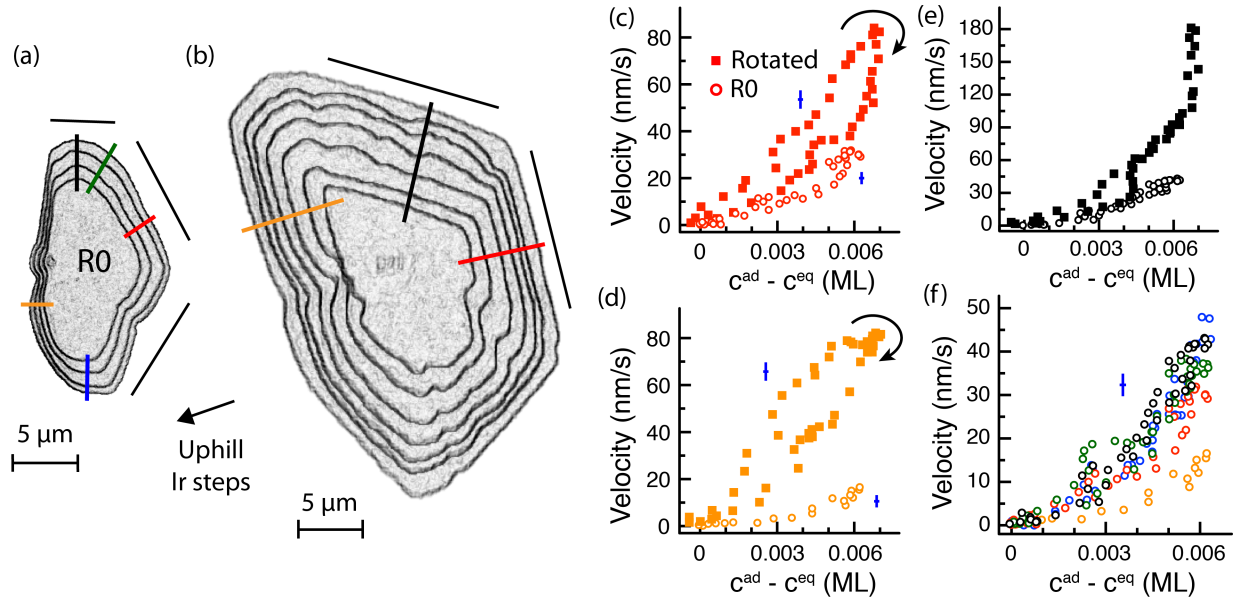


Figure 4.8: LEEM image stacks of a R0 (a) and a rotated (b) island grown at 850 °C. Innermost contour is the starting island; last contour is the final island after growth. Contours are not constant in time but are chosen only to illustrate edge morphology. Arrow depicts the direction of uphill Ir steps; zigzag represented by the exterior, black lines. (c)-(e) Comparison of local velocity measurements for R0 and rotated islands, where 1 ML equals the C atom density in a graphene sheet on Ir(111). Approximate directions relative to the substrate steps: downhill (c), uphill (d), and parallel (e). (f) Comparison of R0 local step edge velocities taken along the correspondingly colored lines in (a). Error bars in (c)-(f) denoted by the blue crosses next to each data set; error in (e) less than symbol size.

in Figure 4.9(a). For this experiment, the C adatom concentration was increased and then held constant. During growth, a protrusion developed in the lower facet. The protrusion was tracked in time by applying the FT technique and one sees in Figure 4.9(b) that the lower facet shifted further from the zigzag by 14 degrees and then returned to its original position. Correspondingly, the step velocity significantly increased (Figure 4.9(c)) when the protrusion was present despite a constant C adatom concentration. In contrast, R0 island growth velocity is independent of edge deviation from the zigzag. Five local R0 velocities were determined along the colored lines in Figure 4.8(a) and plotted together in Figure 4.8(f). Except for the uphill substrate step direction, the R0 velocities are similar along its entire perimeter, irrespective of the local edge deviation relative to the zigzag.

For rotated domains, the most dramatic examples of edge roughening and resulting changes in edge velocity occur for those island edges that lie parallel to the uphill substrate step direction. However, the local velocity measurement is sensitive to the local edge morphology. As shown in Figure 4.9(d), two local velocities were measured for a facet that did

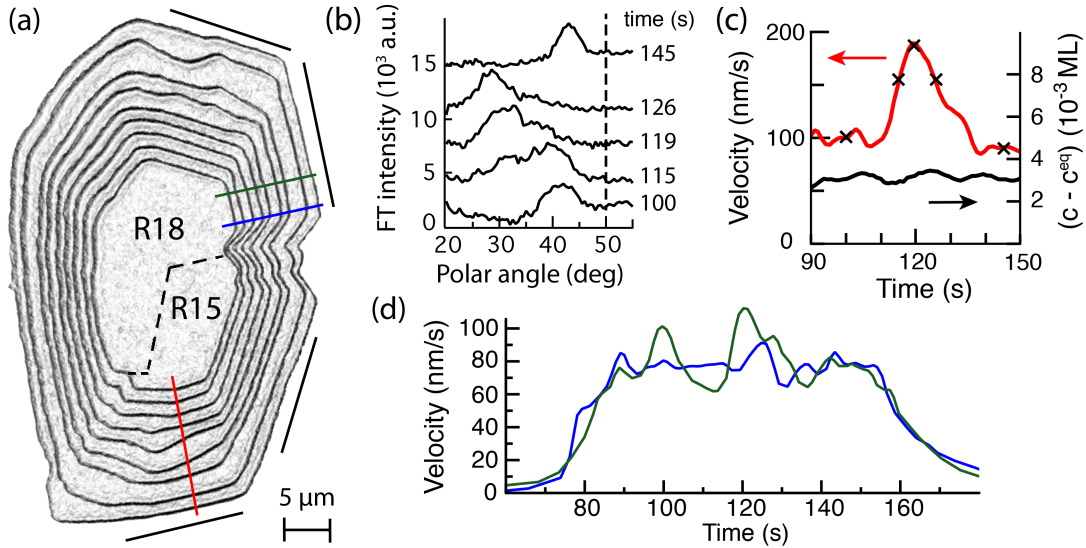


Figure 4.9: (a) LEEM image stack of a rotated island grown at 950 °C. Zigzag termination denoted by the black lines. (b) Lower facet FT intensity during growth, zigzag termination denoted by the vertical, dashed line. (c) Local step velocity measured along the red line in (a) and c^{ad} as a function of time; markers (X) correspond to when the FT intensities in (b) were taken. (d) Local velocity measurements of a single facet taken along the blue and green lines in (a)

not undergo significant morphological changes but their velocities exhibit discrete differences during growth.

4.3.4 Growth model: kink-nucleation- vs. kink-advancement-limited

These observations indicate that the growth of the more faceted rotated islands is highly sensitive to the edge morphology. To explain why, these observations are interpreted in terms of the standard terrace-step-kink model of crystal growth (Section 2.1.1). In this model, growth species attach to kink sites at the crystal step edge. The step velocity is

$$v_s = a\rho_k v_k \quad (4.3)$$

where a is the kink depth, ρ_k is the kink density, and v_k is the kink velocity. The crucial issue is the rate at which kinks nucleate relative to the rate at which kinks advance by attachment.

Consider the velocity measurement in Figure 4.8(e) and Figure 4.9(c). At a constant C adatom concentration, the step velocity of the rotated island significantly increases when the edge deviates from the zigzag. In the terrace-step-kink model, the step velocity at constant C adatom concentration depends only on the kink density. As the edge deviates from the

zigzag, the kink density increases and the step velocity correspondingly increases. Because the roughness was kinetically unstable (i.e., fast growing edges are eliminated from growing crystals [121]), the edge flattened. This demonstrates that the edge grows faster if more kinks are present and places rotated islands in the regime where kink nucleation is relatively slow compared to kink advancement. The observed faceting is presumably a consequence of slow kink nucleation and fast attachment to kinks: once a kink nucleates, it rapidly moves until it annihilates by colliding with other kinks or by reaching the crystal edge.

The direction of the hysteresis in growth velocity for rotated islands indicates that increasing the C adatom concentration causes the step velocity to be above its steady-state value. This increase is attributed to differences in kink density: by increasing the C adatom concentration, more kinks are nucleated before their concentration reaches steady state by annihilation, resulting in a higher growth velocity (because rough edges have a kink density, no hysteresis would be expected for the velocity in Figure 4.8(e), which underwent large morphological changes).

R0 islands behave differently. As seen in the image stack in Figure 4.8(a), R0 edges can exhibit large deviations from the zigzag. In the context of the kink model, these deviations from the zigzag reflect a high kink density. However, the step velocity is independent of the edge deviation from the zigzag direction. For example, the R0 velocity taken along the green and black lines in Figure 4.8(a) and compared in Figure 4.8(f) are similar even though the green data are from an edge highly deviated from the zigzag. This result suggests that the R0 edge has a high kink density along the entire island perimeter (perhaps indicating that kink energies are on the order of the thermal energy, kT). This roughness occurs at a length scale smaller than the LEEM resolution limit of ~ 10 nm; nonetheless, meandering R0 island edges on Ir(111) have been observed in STM [62]. In this high-kink-density regime, the step velocity is limited only by attachment kinetics to kinks, not kink nucleation. The absence of hysteresis and the lower degree of faceting along the zigzag for R0 islands support the scenario of a more kinked edge in which growth does not depend on kink nucleation kinetics.

Thus, these results indicate that rotated and R0 islands grow in different kinetic regimes in the temperature range of 750 °C to 900 °C: kink-nucleation-limited and kink-advancement-limited, respectively, as depicted in Figure 4.10.

4.3.5 Graphene edge binding to the substrate

Why does the growth mechanism change with graphene orientation? This is ascribed to relative differences in the graphene edge binding strength to the substrate. Graphene edges can bind tightly to metal substrates [3, 4, 103]. Furthermore, the moiré corrugations in the graphene sheet caused by interactions with the substrate change markedly with orientation [20]. Given the large unit cells of the moirés, it is difficult to predict how bonding of the edges will depend on orientation, but it is reasonable to expect the change in bonding with orientation will also be large. This would cause kink energies and kink densities to depend on orientation. Further evidence that the edge binding strength depends on island orientation is revealed in the R0 LEEM image stack in Figure 4.8(a); R0 growth is significantly slower

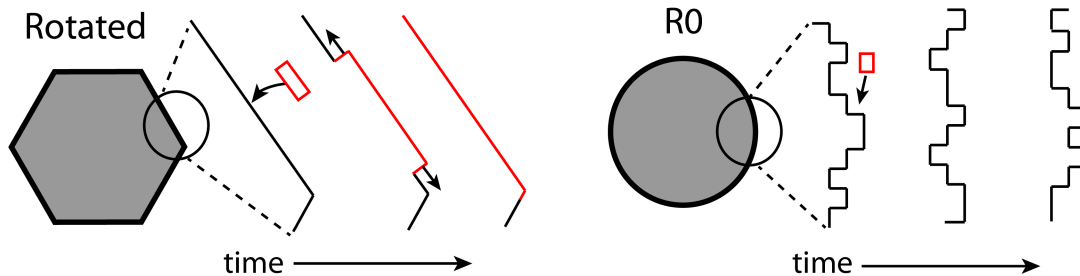


Figure 4.10: Orientation-dependent graphene growth model on Ir(111). Rotated domains are kink-nucleation-limited, resulting in straight edges that lie near the zigzag. R0 domains are rounded with a high density of kinks and growth is kink-advancement-limited.

in the uphill Ir step direction. This is because the R0 edge forms a stronger bond with an uphill substrate step due to the increased overlap of the graphene edge states and the metal step states than on the substrate terrace or at a downhill step [10, 62]. Rotated islands, on the other hand, grow both up and down Ir steps at the same rates (Figure 4.8(b)), reflecting that the R0 edge has a stronger interaction with substrate steps than rotated islands.

In general, the growth of islands that have large, isotropic kink densities, such as R0 islands, should result in circular island shapes. However, Figure 4.8(f) shows that the R0 island velocity varies around its perimeter and results in a non-circular island. These velocity variations are due to the effect of substrate steps on the growth rate. An interesting result of graphene on Ru(0001) is worth noting here. Growth of graphene on Ru(0001) is severely restricted in the uphill substrate step direction [10, 61], more-so than R0 islands on Ir(111). However, after Ar⁺ sputtering the Ru crystal, island growth resulted in circular islands [122]. The sputtering purportedly creates bubbles of Ar beneath the surface, but it is unclear how this exactly affects the Ru steps. Nonetheless, graphene islands with edges that are strongly bound to the substrate can result in round, isotropic island shapes.

4.4 Graphene growth by cluster attachment

The velocities in Figure 4.8(c)-4.8(f) are non-linear functions of the C adatom concentration. As discussed in Section 2.1.3, this non-linearity can have multiple sources, including the kink-nucleation kinetics of rotated domains. In contrast, R0 has a high kink density. In the high kink density limit, the step velocity is directly proportional to the kink velocity (Equation 2.1) and the non-linearity suggests a critical size for kink propagation. In this section, the R0 local velocities are analyzed to determine this size of the attachment species to kinks.

Due to the high kink density, Equation 2.15 models the growth behavior of R0 domains:

$$v_s = B \left[\left(\frac{c^{ad}}{c^{eq}} \right)^n - 1 \right].$$

This equation is used to fit the velocity data as a function of the C adatom concentration. To apply this equation, the equilibrium adatom concentration, c^{eq} , must be known and its experimental determination is presented in the following section.

4.4.1 Determining the equilibrium adatom concentration

The LEEM reflectivity was used to determine the equilibrium adatom concentration, following the method applied to graphene on Ru(0001) in Ref. [61]. The Ir substrate was thoroughly cleaned of dissolved C by segregating C from the bulk and then removing by oxidation. This was performed until no graphene nucleation was observed after holding the substrate at the temperatures of interest (750 °C - 850 °C) for at least 12 hours, i.e., C segregation was slow enough such that no nucleation occurred after 12 hours. To perform the experiment, the substrate was flashed to ~ 1200 °C, brought to the temperature of interest, and then immediately imaged to establish a baseline reflectivity. It was assumed that this starting surface (reflectivity) was devoid of C adatoms. The reflectivity was converted to an adatom concentration by using the predetermined proportionality factor, λ , as shown in Figure 4.11(a). The unchanging initial baseline indicates that C segregation from the bulk was negligible. After a baseline was established, ethylene was introduced into the chamber. The adatom concentration increased until islands nucleated, as shown in Figure 4.11(a). After nucleation, the islands consume adatoms until a steady-state growth rate is achieved, resulting in a decrease in the adatom concentration. Growth was continued for approximately one minute and then the ethylene was turned off, at which point the islands consumed the adatoms until they came into equilibrium.

The difference in reflectivity between the C-free surface and the sub-ML graphene surface is directly proportional to the equilibrium adatom density and can be directly calculated from Figure 4.11, where $c^{eq} = 0.0055$ ML for this experiment at 800 °C. These large nucleation and equilibrium adatom concentrations are consistent with graphene on Ru(0001) [61]. Equilibrium adatom concentrations were determined between the temperatures of 750 °C and 850 °C. The results are plotted in the Arrhenius form in Figure 4.11(b). The slope multiplied by the Boltzmann constant gives the enthalpy of adatom formation, E_f , i.e., the energy difference between a carbon atom in the graphene sheet and a carbon adatom. The data yield $E_f = 0.50 \pm 0.07$ eV. This is in agreement with a previous first-principles result of $E_f = 0.5$ eV [21] and indicates that C adatoms are tightly bound to the Ir substrate (on the order of ~ 7 eV when using the cohesive energy of C in graphite (7.4 eV) for graphene [88]). For the following fitting analysis, it was assumed that $c^{eq} = e^{\frac{-0.5\text{eV}}{kT}}$.

4.4.2 Determining the attachment species for R0

With c^{eq} known as a function of temperature, Equation 2.15 can now be applied to the velocity data. Multiple local velocity measurements were taken for each R0 growth between 750 °C - 900 °C (see Appendix A.2). Measurements taken parallel to the Ir substrate steps are plotted in Figure 4.12(a) to illustrate the R0 growth rate as a function of temperature.

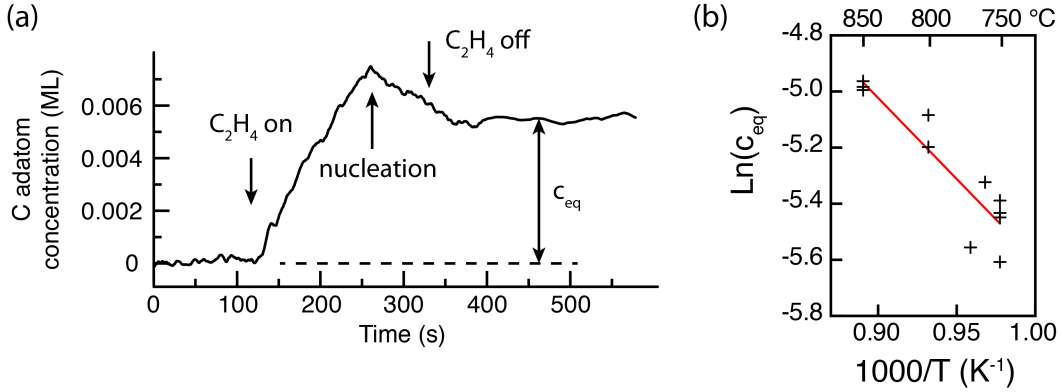


Figure 4.11: (a) A LEEM experiment to determine the C adatom concentration in equilibrium with graphene islands at 800 °C by converting the reflectivity to adatom concentration. At the start, there is no C on the surface. Introducing ethylene gas causes an increase in the adatom concentration until nucleation occurs. After the ethylene is turned off, the concentration comes into equilibrium with the islands and remains constant. (b) Results from c^{eq} experiments as a function of inverse temperature. The slope of the linear fit (red line) multiplied by the Boltzmann constant gives E_f .

To determine the cluster size for growth, Equation 2.15 was applied to each locally measured velocity. The experimentally obtained c^{eq} values were input into Equation 2.15, and B and n were optimized to fit the velocity data (Figure 4.12(b)). The individual fitting results are shown in Table 4.1. The average extracted value for n was 4.1 ± 1.0 , where the error is the standard deviation. Interestingly, STM of graphene on Ir(111) observed the kink structure depicted for the R0 island in Figure 4.12(c) [123]. Attachment of an even-numbered cluster (2, 4, 6 atoms) would not alter the kink morphology, i.e., the number of dangling bonds, and thus a four-atom cluster provides a simple interpretation of the cluster responsible for kink propagation.

Table 4.1: R0 local velocity fitting results. The direction of the local velocity measurement relative to the substrate steps is denoted. c^{eq} was fixed to 0.0034 ML, 0.0045 ML, 0.0057 ML, and 0.0071 ML for fitting at 750 °C, 800 °C, 850 °C, 900 °C, respectively.

Direction	750 °C		800 °C		850 °C		900 °C	
	B (nm/s)	n						
Parallel	0.1	4.5	1.4	3.6	4.1	3.4	9.4	4.4
Downhill	0.2	3.8	0.3	5.5	2.0	4.2	2.0	6.7
Uphill	0.01	5.8	0.7	2.3	0.4	4.9	0.3	6.5
Other	0.3	3.2	2.8	3.0	7.5	2.4	18	3.6
Other					3.6	3.1	5.3	4.1

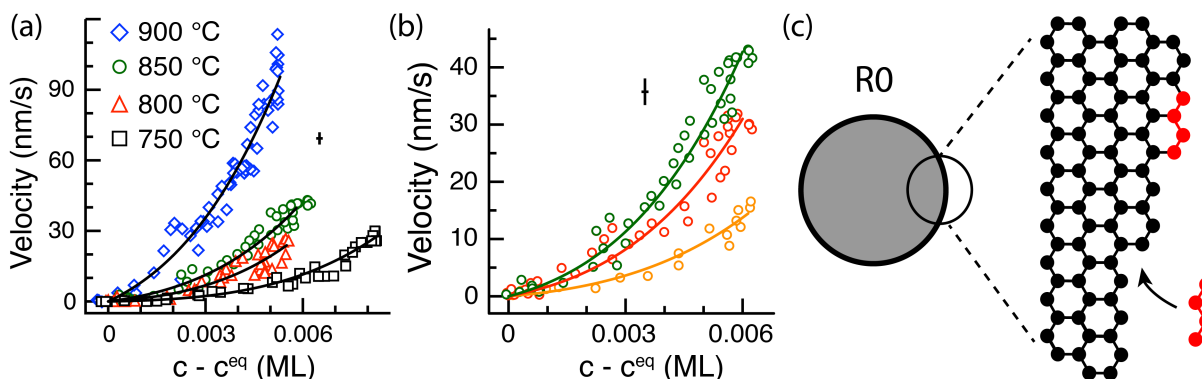


Figure 4.12: (a) Comparison of R0 local velocities taken in the direction parallel to substrate steps. Solid lines are fits using Equation 2.15 with $n = 4$. (b) Select local velocity measurements from the 850 °C R0 island with best fits. Local velocities were taken in the directions relative to the substrate steps: parallel (green), downhill (red), and uphill (orange). Error bars in (a) and (b) are denoted by the crosses. (c) R0 growth model by attachment of a 4-atom C cluster to kinks. The kink structure depicted has been observed in STM [123].

The variation in the local R0 step velocity around its perimeter does not affect the cluster size analysis. As seen in Figure 4.13(a), all of the R0 local velocities (from Figure 4.8(f)) scale directly onto each other when multiplied by a chosen constant. The cluster size for attachment is reflected in the non-linearity of the velocity with the C adatom concentration, which is preserved for all local velocity measurements. Instead, the scaling only affects the value of the kinetic coefficient, B .

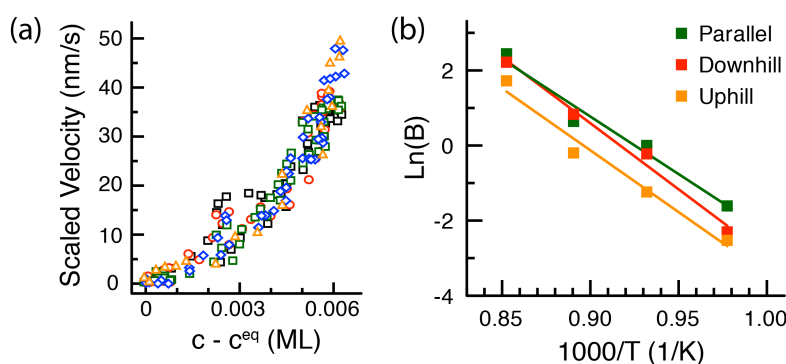


Figure 4.13: (a) All five of the local velocity measurements for the 850 °C R0 island (Figure 4.8(f)) scale onto each other when multiplied by a chosen constant. (b) Arrhenius plot of the kinetic coefficient, B , obtained by assuming $n = 4$ and applying the fitting analysis to the local velocities taken in the parallel, downhill, and uphill substrate step directions.

An Arrhenius analysis of the kinetic coefficient, B , gives the activation barrier for growth.

To determine B , the fitting procedure was repeated assuming $n = 4$ and optimizing B for the best fit. The results are plotted in Figure 4.13(b). From the slope of the line fits, the resulting activation barriers are 2.6 ± 0.3 eV in the parallel substrate direction, 3.0 ± 0.2 eV in the downhill step direction, and 2.8 ± 0.3 eV in the uphill substrate direction. Thus, the activation barrier for R0 island growth is ~ 2.8 eV.

4.4.3 Growth species for rotated domains

Analysis of the kink-nucleation-limited regime is more challenging. Here, kinks nucleate by the attachment of clusters to the step edge [85, 94], resulting in a kink density that depends on the C adatom concentration. In this regime, the step velocity is a convolution of the individual dependencies of the kink density and kink velocity on the C adatom concentration; see Equation 2.17. This increased complexity, coupled with the observations that the step edge velocity for rotated islands depends precisely on its morphology, which can vary during growth, prevents the application of a simple model to determine cluster sizes involved in kink nucleation and kink attachment for rotated islands.

Nonetheless, a few assumptions can greatly simplify the analysis and can offer some insight as discussed in Section 2.1.3. One assumption is a vanishing equilibrium kink density. Given that rotated islands have faceted edges near the zigzag before and after growth, this can be taken as a zeroth-order approximation. And if one further assumes that the highest-order term of the velocity dependence on the adatom concentration captures the behavior, then Equation 2.18 can be applied to the kink-nucleation-limited growth kinetics,

$$v_s \approx B_{J,nK} \left[\left(\frac{c^{ad}}{c^{eq}} \right)^{\frac{m+n}{2}} - 1 \right],$$

where $B_{J,nK}$ is the kinetic coefficient for the step velocity of a non-Kossel crystal and kink nucleation. Here, the non-linearity of the step velocity goes as $(m+n)/2$, where m is the cluster size responsible for kink nucleation.

In order to eliminate the effect of local variations in the edge morphology and growth rate of rotated domains during growth, an average step velocity is computed for rotated domains [61],

$$v_{ave} = (1/p) dA/dt \quad (4.4)$$

where p and A are the island perimeter and area, respectively. IDL was used to determine the island area and perimeter for each frame. The results are shown in Figure 4.14. The average velocity results still capture the hysteresis of rotated islands. However, experimentally, the returning C adatom concentration data is closer to steady-state because the rate of change of the C adatom concentration was slightly slower than when it was increased. Therefore, the velocity data for the returning C adatom concentration are used for the fitting analysis here.

Equation 2.18 was applied to the data using $c^{eq} = e^{-\frac{0.5\text{eV}}{kT}}$, as before, and optimizing for $B_{J,nK}$, m , and n . The results shown in Table 4.2 indicate that the quantity $(m+n) \approx 6$ to

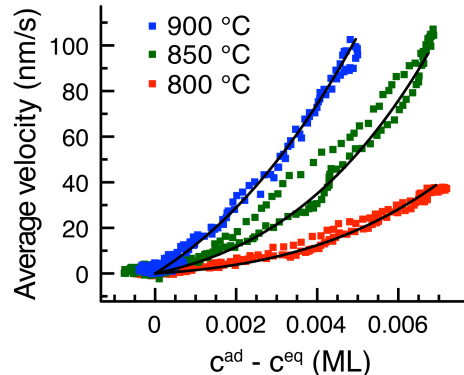


Figure 4.14: Average growth rate of rotated islands with resulting fit (solid line) using Equation 2.18

8. At this point, one is limited to speculation about possible scenarios. One scenario is to assume that a 4-atom cluster attaches to kinks for rotated domains, $n = 4$, as was concluded for R0. Then, m , the cluster responsible for kink nucleation, is on the order of 2, 3, or 4. It is stressed that the arrival to these values required multiple assumptions and the results should be interpreted with restraint.

Table 4.2: Fitting results using the average growth velocity of rotated domains.

Temperature ($^{\circ}\text{C}$)	c^{eq} (ML)	B (nm/s)	$(m + n)$
800	0.0045	1.4	7.3
850	0.0057	5.7	7.4
900	0.0071	25.7	6.1

4.4.4 Unifying cluster attachment to Ru(0001) and Ir(111)

The first observation of a non-linear growth velocity for graphene was on Ru(0001), where a similar analysis gave $n = 4.8 \pm 0.5$ [61]. It was concluded that this cluster was responsible for kink nucleation and a picture was presented in which an odd numbered cluster attached to a zigzag edge to nucleate kinks and the resulting kink advancement was by attachment of smaller clusters, e.g., two atoms. Thus, it was concluded that the rate-limiting step was the attachment of a 5-atom C cluster [61]. The work on Ru(0001) was a pioneering study of graphene growth and the first use of LEEM reflectivity to investigate growth kinetics. However, based on the results and analysis here, it is proposed that graphene growth on Ru(0001) follows the same mechanism as R0 on Ir(111). Graphene islands on Ru(0001) are rounded [61], not faceted as one would expect for kink-nucleation-limited growth, and indicates that they have a high kink density. Based on this, one would then be inclined to

conclude that the attachment species was a 4-atom cluster to kinks, not a 5-atom cluster attachment to a kinkless zigzag step edge.

4.5 Summary and significance of findings

The data and analysis in this chapter have shown that graphene exhibits distinct growth mechanisms that depend on its in-plane orientation relative to the Ir(111) lattice: kink-nucleation- and kink-advancement-limited. These different growth mechanisms are reflected in the island shape and how the edge morphology affects the growth rate. This dependence is surprising given that the van der Waals interactions with the substrate presumably do not significantly depend on orientation. Instead, it is proposed that the graphene edge binding strength to the substrate is orientation-dependent and significantly affects the growth process.

The growth species was determined by analyzing step velocities as a function of the C adatom concentration. R0 domains grow by the attachment of a 4-atom C cluster to kinks. The clusters involved in the growth of rotated domains is significantly more challenging to determine; a zeroth-order approximation indicates that the clusters responsible for kink nucleation and kink attachment sum to 6 to 8, i.e., $(m + n) \approx 6$ to 8.

The relationship between growth shapes and edge binding strength that is observed here is consistent with observations of graphene on other substrates. Graphene islands on Ru(0001) are rounded and their growth is strongly inhibited in the uphill substrate step direction [61], an indication of strong edge binding. Graphene islands on Pt(111) [13], Ni(111) [65], and Cu foils [23] are faceted and their growth is significantly less affected by substrate steps. The structure and properties of grain boundaries that form when grains coalesce will depend on these growth shapes. Thus, this work demonstrates that the optimal substrate for the growth of 2D materials can be dictated by how strongly island edges bind with the substrate, not just its interior.

Chapter 5

Reorientation of graphene domains on Ir(111)

As discussed in Chapter 1, attempts to grow large, structurally pristine two-dimensional materials such as graphene and transition-metal dichalcogenides are often frustrated by the fact that different rotational variants nucleate and grow, leading to a polycrystalline film. This is not surprising given the weak film-substrate interactions that are inherent in the van der Waals epitaxy of these materials on lattice-mismatched substrates. What is interesting, however, is that rotational disorder (mosaicity) in graphene films greatly varies with the substrate. A single orientation exists on Ru(0001) [61, 124] and graphene on Au(111) has shown exceptional rotational order [12]. Graphene on copper spans an $\sim 8^\circ$ range of orientations centered about R0 [22]. As seen here, on Ir(111) graphene assumes essentially a continuum of orientations. In the case of Ge(110), a single orientation has been achieved but only after optimization of the growth conditions [15]. The fundamentals that dictate this mosaicity with various substrates are unknown. Numerous questions arise: does a preferred orientation exist? If so, what is it and what dictates it?

One approach to investigate these questions is through thermal annealing to attain an energetically preferred orientation. However, such reorientation has not been observed, and given the weak interaction between the growing 2D material and the substrate, it is not clear if the driving force for domain alignment is sufficiently large.

In this chapter, LEEM is used to observe the behavior of graphene rotational variants on Ir(111) during thermal annealing. The experimental process is laid out in Section 5.1. It is observed that graphene domains can change their orientation by three mechanisms, which are shown in Section 5.2. These results are interpreted in the attachment-limited growth regime of graphene on Ir(111) in Section 5.3. In Section 5.4, it is shown that a preferred orientation exists and section 5.5 presents a method to determine the driving force for reorientation and includes the results. Sections 5.6 and 5.7 discuss two of the mechanisms in more detail. Insight is given by an atomic model of the changing corrugation of the graphene sheet with orientation and is presented in Section 5.8. These results, and the experimental data, are compared to density functional theory (DFT) results in Section 5.9. Finally, the significance

is discussed in Section 5.10.

5.1 Experimental process

Graphene islands were nucleated by heating the Ir substrate to 800 °C - 900 °C and introducing ethylene gas into the LEEM chamber. After nucleation, the islands were grown for approximately one minute and then the ethylene was turned off. An area with multiple co-existing graphene domains was found and their orientation was determined by LEED. The domains were then imaged while annealing. The temperature was adjusted as necessary and was measured by a W-Rh thermocouple welded directly to the Ir crystal. The spatial extent of individual domains of a given orientation can be deduced from differences in the reflectivity within the graphene islands [20], as shown in Figure 5.1(a).

5.2 Results

In the absence of an external C flux, three mechanisms in which domain orientation changed were observed. The first, shown in Figure 5.1(a) and 5.1(b), was that some orientations grew while other orientations shrank simultaneously. Figure 5.1(c) compares the two frames and highlights the changes after 155 minutes. R0 and R11 domains grew while the R12 domain simultaneously dissolved.

The second process appeared upon further annealing. After 200 minutes the reflectivity of the R12 domain circled in Figure 5.1(b) changed in time and is highlighted by the series of LEEM images in Figure 5.1(c). This transformation occurred *continuously* over ~ 80 minutes as shown by the recorded reflectivity in Figure 5.1(f). Selected-area LEED (Figure 5.1(g)) revealed that this entire region underwent a change in orientation from R12 to R4. Interestingly, the initial R12 domain dissolved as the newly created R4 domain grew. It is noted that a *rate* of transformation should not be inferred from the rate of reflectivity change in Figure 5.1(f) because reflectivity is not directly proportional to orientation [20]. Instead, the continual change in reflectivity indicates that the entire region underwent a continual change in orientation, i.e., a boundary did not move through the region.

The third process is shown in Figure 5.1(h). As the first two processes were occurring, the boundary between the R11 and R12 domain, denoted by the red arrows, moved into the R12 domain. The boundary curvature changed as it moved and is discussed further below.

Twenty such annealing experiments were performed at constant temperature in which these domain reorientation mechanisms were observed. More highly rotated domains always dissolved while less-rotated domains grew. Within those 20 experiments, the continuous lattice rotation was observed five times and domain boundary motion was observed only once (See Appendix A.3 for other data sets). Typically, an hour-long annealing step eliminated half of the rotational variants.

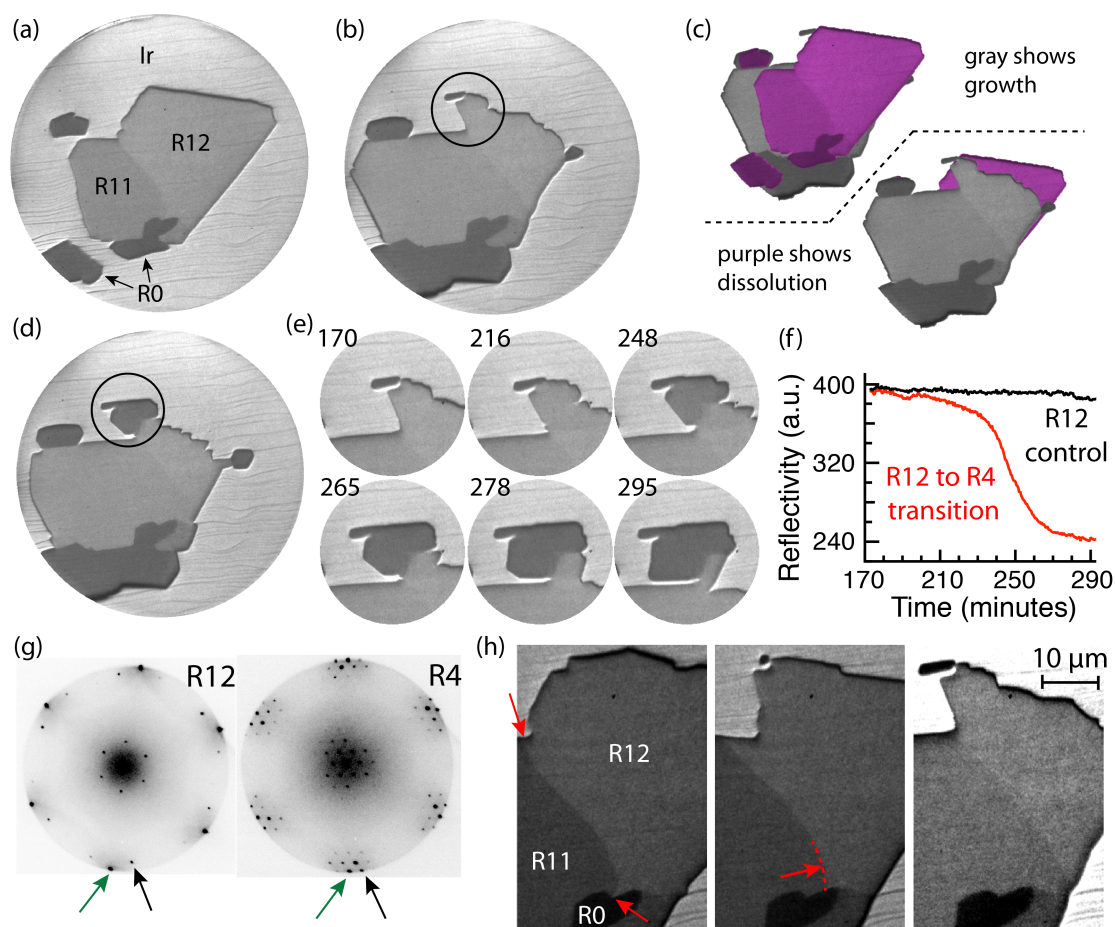


Figure 5.1: LEEM image of a sub-monolayer graphene film on Ir(111) at 1050 °C (75 μm field of view (FOV)). (b) Evolution of graphene islands after annealing at 1050 °C for 155 minutes. (c) Image stacks of (a) and (b) after removing the background shows how the islands evolved. With the initial frame (false-colored purple) on top, exposed areas show growth, reversing the image order exposes areas that dissolved. (d) LEEM image after annealing for 257 minutes; circles in (b) and (d) mark a section of the R12 domain that gradually transformed into a R4 domain. (e) LEEM images that further highlight the R12 to R4 transformation; 25 μm FOV, time in minutes is noted with each image. (f) Island reflectivity monitored in time for the R12 domain and the R12 to R4 transition region. (g) Selected-area LEED taken before and after the reflectivity change. Arrows: graphene (green) and Ir(111) (black) first-order LEED spots. (h) Domain boundary motion between R11 and R12. Middle frame highlights the radius of curvature of the boundary as it moved (red arrow). Time, from left to right: 55, 102, 165 minutes.

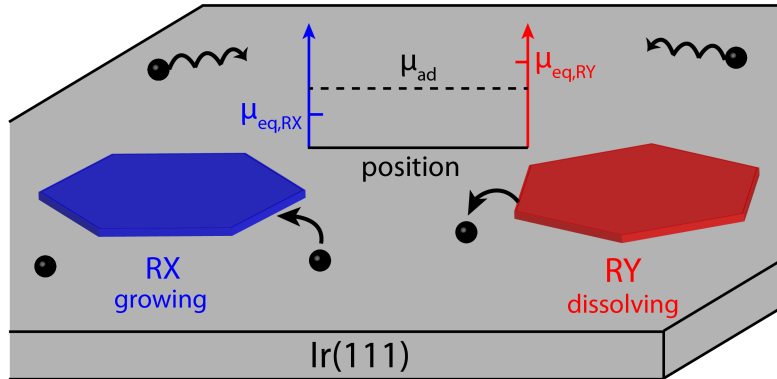


Figure 5.2: Interpretation of the simultaneous growth and dissolution of graphene domains, RX and RY respectively, for a spatially uniform C adatom concentration.

5.3 Discussion of ripening results

In general, growth or dissolution is dictated by the surface adatom concentration adjacent to the island, c^{ad} , relative to the equilibrium adatom concentration for the graphene domain, c^{eq} . Growth results when $c^{ad} > c^{eq}$ and dissolution occurs when $c^{ad} < c^{eq}$. For an ideal adatom lattice gas, the chemical potential difference associated with growth or dissolution is $\Delta\mu \approx kT \ln(c^{ad}/c^{eq})$ [92]. LEEM reflectivity measurements show that the adatom concentration around each island is the same throughout the regions of observation (tens of microns), which is consistent with attachment-limited growth of graphene on Ir [21]. Therefore, the simultaneous growth of a domain of one orientation and dissolution of another with a different orientation indicates that the equilibrium adatom concentration of a given domain depends on its orientation relative to the substrate and, correspondingly, that the chemical potential is orientation dependent as illustrated in Figure 5.2.

5.4 Relative graphene chemical potential as a function of orientation

The relative chemical potential of different rotations can be immediately determined by combining the experimental results and is shown in Figure 5.3. For example, if one experiment shows that $\mu_{RX} > \mu_{RY}$ and another experiment shows that $\mu_{RY} > \mu_{RZ}$, then the two experiments can be combined: $\mu_{RX} > \mu_{RY} > \mu_{RZ}$. Based on the 20 ripening experiments, all observations indicate that domains aligned with the Ir substrate, R0, have the lowest chemical potential and the chemical potential increases as the angle of rotation increases from R0. Multiple rotations on one line indicate that these rotation couples have not been observed together in the same experiment and cannot be further distinguished, e.g., from multiple experiments it has been observed that both R11 and R8 grew while R20, R16, R14, and R12

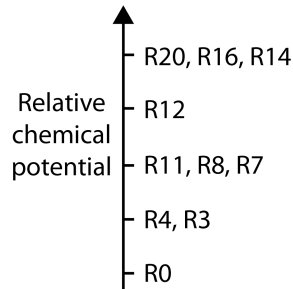


Figure 5.3: Relative chemical potential of graphene rotational variants on Ir(111).

simultaneously dissolved, and R11 and R8 dissolved while R4, R3, and R0 simultaneously grew, but R8 and R11 themselves were not observed together and thus further conclusions cannot be made.

This picture is consistent with the observed spontaneous change in domain orientation shown in Figure 5.1(d). A domain can lower its chemical potential by reducing its rotation angle. With its new orientation, the R4 domain had a lower equilibrium adatom concentration compared to the R12 domain, which resulted in the subsequent growth of the R4 domain after the transformation while the remaining R12 domain continued to dissolve.

5.5 Quantitative differences in chemical potential

The first process, simultaneous growth and dissolution, was temperature sensitive. At lower temperatures, all domains grew, while at high temperatures all domains shrank. This temperature dependence is used to estimate quantitative differences in chemical potential between the rotational variants.

As one sees in Figure 5.4, graphene islands were imaged as the temperature was varied in steps of ~ 5 K. The domain areas were measured with time and are plotted in Figure 5.4(b). At 997 °C (200-800 seconds), all domains grew; increasing to 1005 °C (800-1000 seconds) resulted in the R14 domain dissolving while the R8 domain continued to grow. Increasing the temperature further ended the simultaneous dissolution and growth between the R14 and R8 domains: at 1030 °C the R8 domain ceased growing (2800-3200 seconds). However, as depicted in Figure 5.4(c), the standalone R0 island grew the entire time.

This temperature dependence can be explained by the C dissolved in the Ir crystal. A small C solubility in Ir exists and exponentially increases with temperature [125]. That is, the C solubility limit in the Ir substrate varies with the substrate temperature. For a given C concentration in the bulk, c_{bulk} , C will segregate from or dissolve into the bulk depending on c_{bulk} relative to the temperature-dependent solubility limit (because of the size of the Ir bulk relative to the surface, it is assumed that dissolution or segregation of C from the bulk does not appreciably alter c_{bulk}). Thus, by adjusting the temperature one can vary

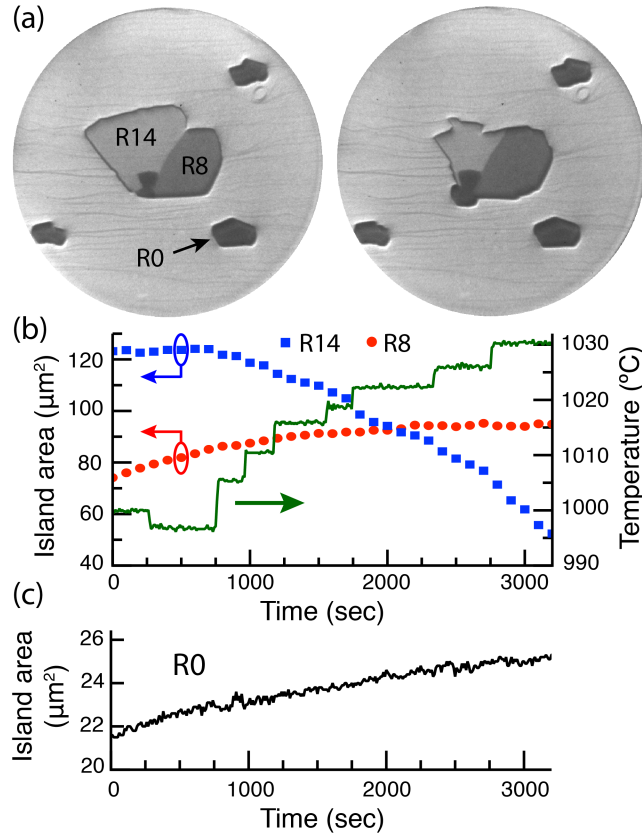


Figure 5.4: (a) LEEM images ($50 \mu\text{m}$ FOV) of graphene islands at 500 sec (left) and 3200 sec (right) during temperature-controlled ripening. (b) R14 and R8 domain areas were measured every 10th frame (100 seconds); substrate temperature was adjusted in steps of $\sim 5^{\circ}\text{C}$. (c) Standalone R0 island area was measured every frame (10 seconds).

the relationship between c^{ad} and c^{eq} , i.e., at lower temperatures, bulk segregation causes the carbon adatom chemical potential to be above the equilibrium value of all islands and as the temperature increases, the segregation flux to the surface decreases and the adatom concentration decreases below the equilibrium value.

It is noted that this does not alter the interpretation of a spatially uniform surface adatom concentration. Because the barrier for bulk C diffusion in Ir is $\sim 2.5 \text{ eV}$ [126], surface diffusion is still sufficiently rapid to eliminate any surface concentration gradients as C adatoms dissolve into the bulk. Furthermore, graphene growth or dissolution depends on the surface adatom concentration, not c_{bulk} [88, 127].

What is the magnitude of the driving force for a rotated domain RX to realign itself to R0? To determine their differences in chemical potential, the temperature-controlled ripening experiment described above is used to estimate the differences in equilibrium adatom concentrations between different rotations.

The growth rate of R0 domains is given by

$$v_{R0} = B(T) \left[\left(\frac{c^{ad}}{c^{eq,R0}} \right)^n - 1 \right] \quad (5.1)$$

where $c_{eq,R0}$ is the equilibrium adatom concentration for the R0 island, n is the cluster size for attachment to a kink and is equal to four, and $B = \exp(31 - (33800 \pm 1300)/T)$ nm/s is the kinetic coefficient for the absolute temperature, T (see Section 5.5.1 below for determining $B(T)$). Converting the $A(t)$ plot of Figure 5.4(c) into a growth velocity¹ allows one to determine the adatom concentration at the times when the R14 and R8 domains are stationary and in equilibrium with the adatoms. If a rotated domain, RX, is stationary while a standalone R0 island continues to grow, the difference in chemical potential can be estimated by

$$\mu_{RX} - \mu_{R0} \approx kT \ln \frac{c^{eq,RX}}{c^{eq,R0}} \approx kT \ln \left[\left(\frac{v_{R0}}{B} + 1 \right)^{\frac{1}{n}} \right]. \quad (5.2)$$

When the R14 domain was stationary, the R0 velocity was 540 ± 36 nm/hr (at 1000 °C), where the error is from the standard deviation of the dA/dt line fit. When the R8 domain was stationary from 2800-3200 seconds (at 1030 °C), the R0 velocity decreased to 144 ± 36 nm/hr. Using Equation 5.2 it is determined that the R14 domain had a chemical potential of 0.07 ± 0.01 meV/C above R0, and R8 was 0.01 ± 0.01 meV/C above R0.

Five temperature-controlled experiments were conducted in the same manner. The experimental data are shown in Table 5.1 and the estimated differences in chemical potential relative to R0 are shown in Figure 5.5. The results were reproducible across the different experiments. The chemical potential increased with rotation from R0, as expected. The trend is not linear, with small differences in chemical potential for small rotations and larger increases in chemical potential as the rotation angle increases. Due to the uncertainty in $B(T)$, the absolute scale of the chemical potential may be a factor of two larger or a quarter smaller. Island evolution driven by such small driving forces at elevated temperatures is not unprecedented; the driving force for Ostwald ripening of 2D silicon islands on Si(001) was estimated to be on the order of 0.1 meV/Si [128]. Because chemical potential differences were determined, these values are the driving force for all three reorientaton mechanisms.

5.5.1 Determining average island growth rates

Previously in Chapter 4, the growth rate for R0 islands was determined locally as a function of temperature and the C adatom concentration. These velocities were then modeled using Equation 2.15. Because the ripening velocities observed here are much slower, an average growth rate is computed by measuring the island perimeter, p , and the island area, A , [61]

$$v_{ave} = \frac{1}{p} \frac{dA}{dt}. \quad (5.3)$$

¹The average R0 velocity was computed by measuring its island area, A , and perimeter, p , with time: $v_{ave} = (1/p_{ave})dA/dt$ where dA/dt is the slope of a line fit to the area vs. time data for the time interval in question, and p_{ave} was the average perimeter over the time interval

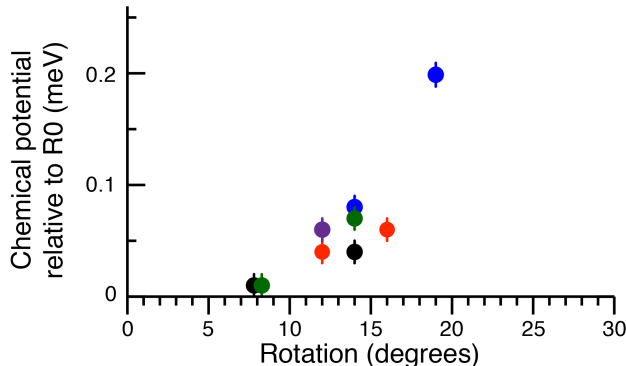


Figure 5.5: Quantitative differences in chemical potential relative to R0. Individual experiments are color-coded; R8 data were offset in x-axis for clarity.

Table 5.1: Results from temperature-controlled ripening experiments.

Experiment	Rotation	v_{R0} (nm/s)	T (°C)	B (nm/s)	$\Delta\mu$ (meV/C)
051013b	R14	0.15	1000	61.5	0.07
	R8	0.04	1028	109	0.01
051313a	R14	0.07	990	49.9	0.04
	R8	0.04	1075	270	0.01
052013a	R12	0.24	1035	125	0.06
052213a	R16	0.21	1019	91.0	0.06
	R12	0.19	1045	153	0.04
052213b	R19	0.32	985	44.7	0.20
	R14	0.21	1010	75.7	0.08

The average growth velocities for R0 were determined and are shown in Figure 5.6(a). These data were then modeled using Equation 2.15 in order to extract the kinetic coefficient, B , by assuming $n = 4$, using the pre-determined c^{eq} data, and then optimizing B for a best fit. The results for B are shown in Figure 5.6(b). A line fit yields $B = \exp(31 - (33800 \pm 1300)/T)$ nm/s. The slope multiplied by the Boltzmann constant gives 2.9 eV, which is consistent with the previously reported local B values (Section 4.4.2). It is noted that v_{ave} for 850 °C and 900 °C growth temperatures exhibit a small gap between the velocities for the increasing and decreasing adatom concentrations. This difference is within the error bars [black, vertical line in Figure 5.6(a)] and is not attributed to any hysteresis, which is consistent with no observed hysteresis in the local velocity measurements in Figure 4.8.

5.5.2 Effect of island edge energies

Since the R0 island ripening velocity was used to estimate differences in chemical potential, it is important to understand the contribution of edge energies, if any. In general, no influence

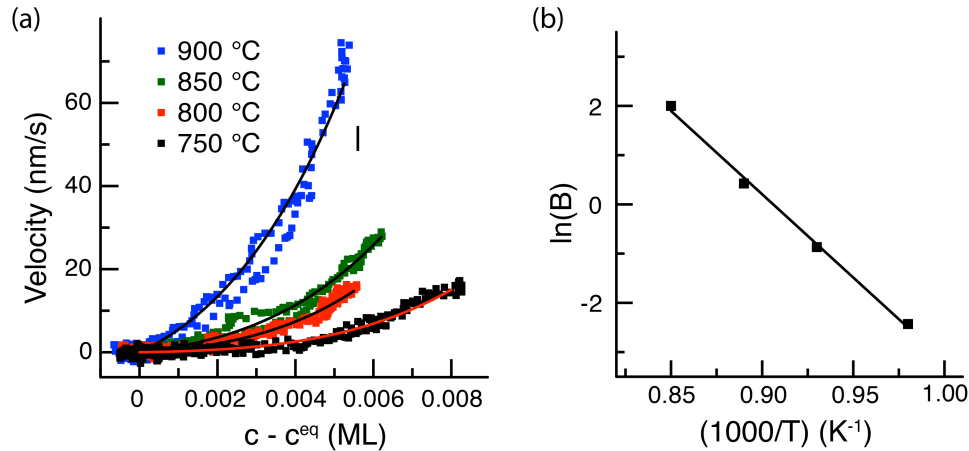


Figure 5.6: (a) Average R0 island growth rate. The solid lines are the resulting fits as discussed in the text. The vertical, black line is the error in the velocity measurement. (b) Arrhenius plot of the kinetic coefficient, B , extracted from the fitting analysis of the average R0 growth rates in (a).

of R0 island size on ripening velocity was observed, which suggests that edge energies are not a significant factor. The R0 areas varied in size from 17 to 90 μm^2 among the various experiments. For example, in one experiment, a R14 domain was stationary at 1010 $^\circ\text{C}$, while the R0 velocity was 0.20 nm/s and had an area of 76 μm^2 . In another experiment, a R14 domain was stationary at 1000 $^\circ\text{C}$, while the R0 velocity was 0.15 nm/s and had an area of 22 μm^2 . Their velocity ratio is ~ 1.3 ; if the velocity was influenced by edge energies, the velocity ratio should depend on the ratio of the island radii of ~ 1.9 . Instead, the velocities can be accounted by the ratio of the kinetic coefficients, $B(1010\text{ }^\circ\text{C})/B(1000\text{ }^\circ\text{C}) \approx 1.2$, indicating that the R0 velocity was independent of island size for these island sizes.

5.6 Domain boundary motion discussion

The reported differences in chemical potential are further supported by analyzing the curvature of the moving domain boundary shown in Figure 5.1(h). Initially, the boundary has a structure in which the curvature changes sign, i.e., the curvature inverts, an artifact attributed to the initial growth of the island. When the boundary began to move, the curvature changed such that the boundary extended into the R12 domain only. This curvature is attributed to pinning by the lower R0 domain. Indeed, as the bottom end of the boundary moved beyond the R0 domain, the boundary straightened (Figure 5.1(h), right frame). The radius of curvature of the boundary while it was moving, but partially pinned, was $\sim 9\ \mu\text{m}$, as seen in the middle frame of Figure 5.1(h). This curvature is used to estimate the difference in chemical potential between the two domains.

Consider an idealized situation in which two phases with different chemical potentials meet at a boundary with both ends pinned. The boundary will move in response to the chemical potential difference, but because its ends are pinned, it will become curved and resultantly lengthen. Equilibrium is achieved when the free energy cost of further increasing the boundary length is equal to the free energy gain by transferring mass from the phase of higher to lower chemical potential, in which the difference in chemical potential is given by

$$\Delta\mu = \frac{\Omega\gamma}{R} \quad (5.4)$$

where Ω is the atomic volume, γ is the domain boundary energy per unit length, and R is the radius of curvature.

Although the boundary is moving in the example shown in Figure 5.1(h), the equilibrium picture is used to estimate a lower bound of the difference in chemical potential, i.e., if the boundary was pinned completely, the radius of curvature would decrease, and thus increase $\Delta\mu$. Ab-initio calculations have previously estimated γ as a function of misorientation between two graphene domains. For a misorientation of 1° , the results from Ref. [129] are extrapolated and gives $\gamma \approx 0.05$ eV/Å. Given the graphene atomic density of 3.8×10^{15} cm⁻² and the 9 μ m radius of curvature between the R11 and R12 domain, the resulting difference in chemical potential between R11 and R12 is ~ 0.002 meV/C. To compare with the results obtained from the velocity analysis, the reported values for R14 and R12 in Figure 5.5 are averaged and their difference taken. Assuming a linear relationship between $\Delta\mu$ and rotation angle in this narrow region, the data give 0.007 meV/C per degree of misorientation. As expected, this result is higher than that obtained from the domain boundary motion. More importantly, the domain boundary analysis supports the order of magnitude of the reported values in Figure 5.5.

TEM has previously been used to determine the atomic structure of graphene domain boundaries [130–132]. In general, the findings indicate a 5-7 defect structure. Previously, domain boundary motion in graphene has only been observed in TEM, where the energy of the electron beam was sufficient to cause atomic motion of the atoms, resulting in boundary motion [131]. Because high energy electrons (80 keV) were required to initiate boundary motion, it is surprising here that boundary motion was observed with only thermal energy on the order of $kT \approx 0.1$ eV. However, the boundary motion was only observed in the case of one degree difference in rotation: it seems that domain boundary mobility must decrease with relative misorientation and limit this mechanism of coarsening.

5.7 Comment: Continuous lattice rotation

The continuous lattice rotation is arguably the most dramatic domain reorientation mechanism observed. The continuous reorientation of a ~ 100 μm^2 domain from R12 to R4 required $\sim 1 \times 10^9$ C atoms to shift. Apparently the driving force was sufficient to drive this reorientation, even at the cost of forming a new domain boundary between the R12 and newly created

R4 domain. The exact mechanisms of this shifting is unknown and provides opportunities for using atomic-scale modeling in order to better understand this reorientation mechanism. It is worth noting that the continuous rotation was seen five times and was active when grain boundary motion was not.

5.8 Orientation-dependent flexure model of graphene on Ir(111)

To understand the origin of the orientation-dependent chemical potential and the extent to which it can be generalized, the corrugation of the graphene sheet is considered. A review of the literature led to the realization that the atomic corrugations of graphene on Ir(111) depend on its orientation, as observed by STM [20]. In that work, a simple geometric model was developed by Dr. Konrad Thürmer of Sandia National Laboratories to replicate the STM images. This section outlines a significantly improved geometric model and its application to the ripening results obtained in collaboration with K. Thürmer.

First, it is assumed that the rotated domains are incommensurate, stress-free honeycomb layers of graphene forming moirés with the substrate. In incommensurate, undistorted moirés, all equivalent positions of C with respect to the substrate are occupied with equal probability, independent of the layer's rotation [133], suggesting an equal energy for all rotational variants. Changing lattice misfit with the substrate does not alter this conclusion; so it is doubtful that lattice misfit determines the preferred orientation. However, it is experimentally observed that graphene sheets are not undistorted 2D sheets. Various techniques, e.g., STM [11, 20, 105, 106], He atom diffraction [105], LEED [11], X-ray diffraction [107], and DFT [102, 106], have shown that graphene sheets on metals are corrugated. STM images of R14, R19 [134], and R30 [20] graphene on Ir(111) reveal that, in addition to the large-scale modulation with moiré periodicity, the graphene topography also exhibits a pronounced fine-scale corrugation (in the case of R30 with a periodicity of ~ 5 Å), which is absent in the R0 phase.

The reason for this corrugation is that the preferred distance of the graphene sheet from the substrate varies locally, depending on the lateral position of the C atoms with respect to the substrate (whether the C atom is at an atop position, a threefold hollow site, etc. See Figure 2.4.) To maximize its binding to the substrate, the graphene sheet flexes slightly in an effort to follow a contour of minimum C-Ir potential. Due to the bending rigidity of the graphene, the carbon atoms are further away from their optimal positions as the wavelength of the corrugation shortens. So the short-wavelength corrugations observed experimentally for rotated graphene would lead to an energy cost.

To estimate the magnitude of this effect, a simple model for the observed corrugations is constructed. For simplicity, it is assumed that the graphene is incommensurate with respect to the Ir substrate, i.e., that the possible energy reduction due to locking into a (higher order) commensurate lattice is not sufficient to overcome the energy cost of straining

the graphene from its preferred lattice constant. Further, it is assumed that the preferred distance z_0 of carbon atoms from the Ir(111) substrate is represented by a two-dimensional sinusoid which has opposite extrema at the atop sites and hollow sites. The force on each carbon atom is taken to be proportional to how far the atom is displaced from the preferred distance and assume that the spring constant k_s is uniform. In the relaxed configuration, this force is balanced by the forces caused by bending the graphene sheet. The equilibrium sheet corrugation is given when this bending force balances the displacement force.

To determine this bending contribution, consider the curvature around atom i and assume atom i and its three nearest-neighbors (NN) lie on a paraboloid (\sim sphere with radius $r = 1/k$ where k is the curvature) with a coordinate system centered at atom i and the x-y plane tangential to the paraboloid. Consider everything to be relatively flat and approximate lengths by their projections, $z = (1/2)(k_1x^2 + k_2y^2)$ and assume $k_1 = k_2 = k = 1/r$. Let the x-axis point to a neighboring atom's projection. This neighbor (and all other nearest neighbors) are higher than atom i by

$$\Delta z_i = z_i = \frac{1}{2}k_i d^2 \quad (5.5)$$

with C-C distance $d = 1.42 \text{ \AA}$. The curvature at atom i is

$$k_i = \frac{2z_i}{d^2} \text{ or } k_i^2 = \frac{4z_i^2}{d^4} \quad (5.6)$$

In the continuum limit, the energy due to bending is [135]

$$E_b = \frac{1}{2}\lambda_b \int K^2 dS \quad (5.7)$$

where λ_b is the mean bending rigidity, $\sim 1.4 \text{ eV}$ for graphene [136], K is the mean curvature, and noting that the Gaussian bending vanishes for a 2D, periodic sheet [136]. Converting the integral to a sum over i gives

$$E_b = \frac{1}{2}\lambda_b \sum k_i^2 S_0 \quad (5.8)$$

where the footprint of a C atom in a graphene sheet is $S_0 = 3d^2\sqrt{3}/4$. Substituting for k_i (Equation 5.6) and S_0 ,

$$E_b = \frac{3\lambda_b\sqrt{3}}{2} \sum \left(\frac{z_i}{d}\right)^2 \quad (5.9)$$

or the bending energy per atom

$$\frac{E_b}{N} = \frac{3\lambda_b\sqrt{3}}{2N} \sum \left(\frac{z_i}{d}\right)^2. \quad (5.10)$$

The force due to bending, F_b , is obtained by taking the derivative of Equation 5.9 with respect to z giving

$$F_b = \frac{3\lambda_b\sqrt{3}\Delta z_i}{d^2} \quad (5.11)$$

where Δz_i is the height difference between atom i and the average of its surround three nearest neighbors.

This model has only two parameters, the amplitude of the sinusoidal preferred C atom distance and the spring constant k_s . To apply this model to graphene on Ir(111), DFT calculations (containing van der Waals contributions) were performed in order to determine the value of these two parameters. DFT was performed to model graphene rotational variants (R0, R7.5, R15, R22.5, and R30) on an Ir(111) substrate. The Ir(111) slab consisted of three atomic layers, which helped minimize computational cost and allowed for the full graphene moiré to be modeled. Full DFT details are contained in Section 5.9 below. As seen in Figure 5.7(a), the DFT reproduces the observed experimental trends of increasing short-wavelength corrugations with increasing rotation angle seen in STM.

To determine the two parameters required for the moiré corrugation model, the DFT results for R0 graphene on Ir(111) are used. First, the DFT results give the equilibrium corrugation. Second, DFT was also performed on a graphene sheet that was constrained to be flat and held at the average separation distance from the Ir substrate, and the resulting forces on each C atom in this configuration were obtained. To calibrate the moiré corrugation model, the amplitude of the sinusoidal preferred separation distance and the spring constant k_s we adjusted to exactly reproduce the amplitude of the corrugation of the relaxed sheet and the root mean square of the forces on the flat sheet. Given these parameters, the corrugation for domains rotated by 7.5, 15, and 30 degrees were then predicted. Height profiles extracted from the moiré corrugation model along the close-packed zigzag direction are shown in Figure 5.7(b). The agreement between this prediction and DFT calculations is striking. It reproduces the position of all C atoms in the profiles in Figure 5.7(b) to within 0.05 angstroms, with most atoms within 0.01 angstroms.

The good agreement makes it plausible that it correctly captures the energy due to C atom displacement and bending of the graphene sheet with changing orientation. And indeed, as shown in Figure 5.8, despite its extreme simplicity, the model correctly reproduces the observed stability of R0 and it easily accounts for the magnitude of the measured energy differences. That the model tends to overestimate the energy differences is not surprising given that the model does not allow lateral relaxation of atomic positions and the factor of two in the uncertainty of the scale of the experimental data (Figure 5.5). (Such small energy differences are generally difficult to compute directly with DFT because of the large moiré unit cells; however, DFT was used to estimate the binding energy difference between R30 and R0 and it was found to be less than ~ 1 meV/C, consistent with the moiré corrugation model and experiment. See Section 5.9). Thus the driving forces for the post-nucleation reorientations that were observed can be explained by the orientation dependence of the moiré corrugation. This driving force applies to all three observed reorientation mechanisms.

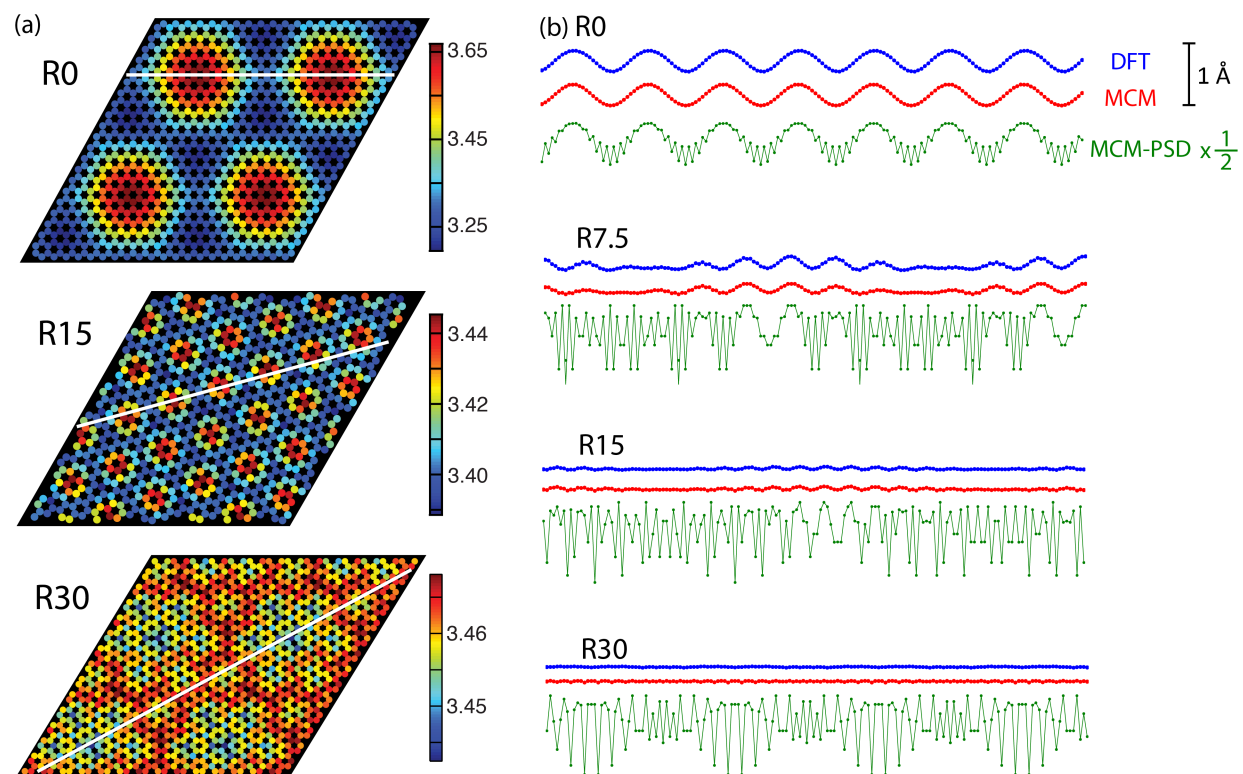


Figure 5.7: (a) Distance of C atoms from the Ir(111) substrate obtained from DFT calculations for graphene rotated by 0, 15, and 30 degrees relative to the Ir(111) lattice. Scale bar is in angstroms. (b) Moiré corrugation model (MCM) results. Green line: the preferred separation distance of C atoms from the substrate (MCM-PSD) taken along the close-packed zigzag direction (representative white lines in (a)), where filled circles represent C atoms. Due to the bending rigidity of the graphene sheet, the C atoms cannot follow the short-wavelength corrugations and the resulting sheet corrugation from the MCM is given by the red line. Corrugation profiles taken from the DFT results are shown in blue for comparison. Scale bar applies to all three profiles for all four rotations. Note: the MCM-PSD profile is multiplied by $\frac{1}{2}$ for clarity.

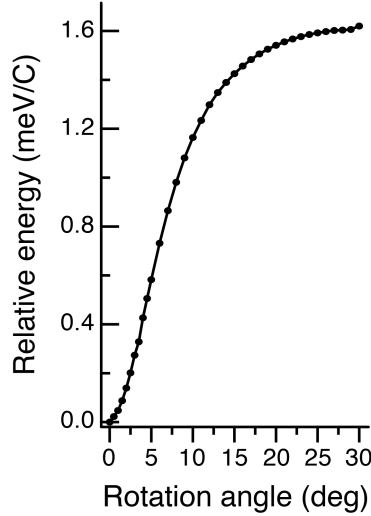


Figure 5.8: Energy per C atom relative to the R0 orientation as a function of rotation angle as determined from the moiré corrugation model.

5.9 Density functional theory results

Calculations using density functional theory were performed by Dr. Michael Foster of Sandia National Laboratories with the optB86b-vdW functional [137] with spin-polarization and using the projector-augmented-wave (PAW) GW-pseudopotentials supplied by VASP [138–141]. A cutoff energy of 400 eV for the plane-wave basis and the Brillouin zone was sampled using 1x1x1 and 2x2x1 k-point grids. The optB86b-vdW exchange-correlation functional was employed in order to account for van der Waals interactions that are required for a qualitative description of the intermolecular interactions between the graphene sheet and the Ir(111) surface. The functional is of the form:

$$E_{xc} = E_x^{optB86b} + E_c^{LDA} + E_c^{vdW-DF}, \quad (5.12)$$

where $E_x^{optB86b}$ is the exchange energy, E_c^{LDA} is the local density approximation (LDA) to the correlation energy, and E_c^{vdW-DF} is the non-local correlation energy term developed by M. Dion et al [142].

The Ir(111) surface was constructed from the optimized face-centered cubic structure, $a = b = c = 3.843 \text{ \AA}$, and the lattice of the surface was fixed during all simulations. The Ir(111) slab consisted of three atomic layers, which helped minimize computational cost and allowed for the full graphene moiré to be modeled. Five different graphene orientations were considered: R0 (542 atoms: 10x10 Ir supercell; 300 Ir and 242 C atoms), R7.5 (776 atoms: 12x12 Ir supercell; 432 Ir and 344 C atoms), R15 (437 atoms: 9x9 Ir supercell; 243 Ir and 194 C atoms), R22.5 (344 atoms: 8x8 Ir supercell; 192 Ir and 152 C atoms), and R30 (657 atoms: 11x11 Ir supercell; 363 Ir and 294 C atoms). Geometry optimizations were performed

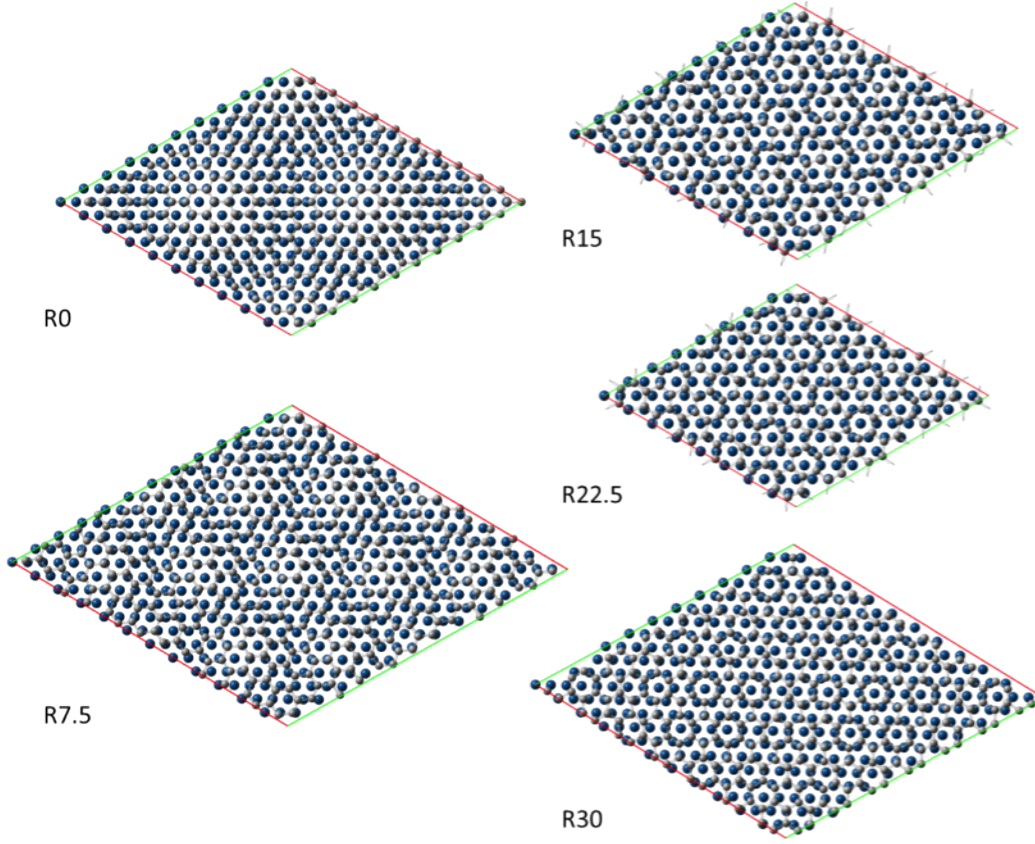


Figure 5.9: The optB86b-vdW optimized R0, R7.5, R15, R22.5, and R30 graphene structures on Ir(111).

until all forces were less than $0.05 \text{ eV}/\text{\AA}$ (optimized structures are shown in Figure 5.9); the total energy was converged to within $1 \times 10^{-6} \text{ eV}$ for both k-point samplings. The binding energies per carbon atom of the systems were determined as follows:

$$E_{BE} = \frac{E_{G@Ir111} - E_G - E_{Ir111}}{N}, \quad (5.13)$$

where $E_{G@Ir111}$ is the total energy of the system (R0, R7.5, R15, R22.5, or R30 on the Ir(111) substrate), E_G and E_{Ir111} are the total energies of the optimized isolated graphene layer and the Ir(111) surface and N is the total number of carbon atoms. The graphene deformation energies (bending energies) were determined from the difference between the single-point energy of the optimized graphene sheet on the Ir(111) surface and the fully optimized graphene sheet within the same unit cell.

The computed graphene deformation energies and binding energies per C atom, determined using the two different k-point grids, are reported in Table 5.2. The larger $2 \times 2 \times 1$ k-point grid was used to test whether the predicted energies from the $1 \times 1 \times 1$ k-point grid

Table 5.2: The optB86b-vdW predicted graphene deformation energies (bending energies), absolute and relative binding energies, and difference in the predicted values using a 1x1x1 and a 2x2x1 k-point grid ($\Delta E/\Delta k$).

k-points	Graphene deformation energy per C atom (meV)			Binding energy per C atom (meV)			Relative binding energy per C atom (meV)	
	1x1x1	2x2x1	($\Delta E/\Delta k$)	1x1x1	2x2x1	($\Delta E/\Delta k$)	1x1x1	2x2x1
R0	0.70	0.63	-0.07	-77.11	-76.68	0.43	0.00	0.00
R7.5	0.87	0.88	0.00	-77.82	-77.39	0.43	-0.71	-0.71
R15	0.23	0.24	0.01	-76.36	-76.48	-0.12	0.75	0.19
R22.5	0.10	0.12	0.01	-77.04	-76.62	0.42	0.07	0.05
R30	0.33	0.33	0.00	-76.93	-76.19	0.74	0.18	0.48

were converged with respect to k-space. The results indicate that the computed graphene deformation energies are converged, however, the binding energies are not. This conclusion was reached by comparing the difference in energies with respect to k-space ($\Delta E/\Delta k$). For the deformation energies, ($\Delta E/\Delta k$) is much smaller than the magnitude of the values. On the other hand, the relative binding energies between the different orientations (R0, R7.5, R15, R22.5, and R30) are smaller than ($\Delta E/\Delta k$). Based on this analysis, it is concluded that the predicted ordering of the deformation energies is statistically significant, but the relative binding energies between orientations is not significant. As a result, the orientation with the greatest binding energy per C atom cannot reliably be determined from these results. Increasing k-space sampling much further is computationally intractable; moreover, each system has different lattice dimensions that affect the relative k-point spacing. Computationally determining differences of one-tenth of a meV is difficult given the various numerical approximations used within DFT (i.e., k-points and energy cutoffs).

5.10 Summary and significance

In summary, it was shown that graphene domains on Ir(111) reorient themselves by three distinct mechanisms during annealing. The driving force for the alignment can be as small as 0.1 meV/C, much less than the total binding strength of graphene to metal surfaces. It is proposed that the origin of the preferential alignment is caused the varying degree to which carbon atoms can attain the preferred distance from the substrate: the graphene bending rigidity prevents the sheet from following the short wavelength corrugations inherent in highly rotated domains.

These results have significant implications on the nature of rotational disorder of graphene islands on various substrates. STM shows that graphene on Au(111) [74] and Cu(111) [75] exhibits the same trend of increasing nearest-neighbor corrugation with rotation angle as seen on Ir(111). One would expect the R0 orientation to be energetically preferred. As

expected, like Ir(111) [21], the majority orientation on Cu(111) [22] and Au(111) [12] is indeed R0. This is especially noteworthy for Au(111), where R0 has a lattice mismatch of 17% [12] and clearly supports the conclusion that the moiré corrugation dictates the resulting island orientation. This raises the possibility that in the systems where good alignment is observed in as-grown films, e.g., Cu(111) [22], Ru(0001) [10, 124], Au(111) [12], and Ge [15], such alignment occurs after nucleation by the continuous lattice rotation mechanism when the islands are small.

Furthermore, these results imply that the rotational disorder of other 2D materials (hexagonal-BN, transition-metal dichalcogenides) can be controlled only when grown on substrates where corrugations exist, e.g., on metals [108–110, 143]. In fact, MoS₂ islands on Cu(111) have been grown with only a single orientation, R0 [109]. This calls into question continued growth efforts on substrates such as SiO₂, which many transition-metal dichalcogenides are currently grown on but corrugations are not observed [144–146].

Since graphene corrugations are ubiquitously observed, the driving force for the coarsening mechanisms on Ir reported here can be expected to be similar in other systems. Despite this small driving force for rotational alignment, these results suggest that post-nucleation annealing of epitaxial graphene can still improve rotational order.

Finally, the moiré corrugation model developed here can be efficiently applied to a broad range of substrates. To implement the model, DFT only needs to be performed for one graphene orientation on any substrate. Then, the DFT results can be used to calibrate the model, at which point the relative energy of all orientations can be easily determined.

Chapter 6

Conclusions and future work

In this final chapter, the results are summarized and the two main investigations, growth and reorientation, are discussed in a broader context. Finally, future directions that arise from these results are presented.

6.1 Summary of findings

Developing the science of van der Waals epitaxy is critical for the development and deployment of two-dimensional materials. In this dissertation, significant progress was made to this end by investigating the orientation-dependent van der Waals epitaxy of graphene on Ir(111). Fundamental insights were gained on factors that affect the growth of graphene and what governs the epitaxial relationship between islands and the substrate. In Chapter 4, the growth characteristics of graphene rotational variants on Ir(111) were investigated by low-energy electron microscopy. The real-time imaging of graphene growth and the unique ability of LEEM to simultaneously monitor the surface adatom concentration were critical to investigate the growth kinetics. By coupling local growth rates and the island edge morphology, it was determined that islands aligned with the substrate, R0, have a high kink density and grow in a kink-advancement-limited growth regime. In contrast, the local velocity of islands rotated with respect to the Ir lattice were highly sensitive to the edge deviation from the zigzag orientation, and were determined to grow in a kink-nucleation-limited growth regime. The source of these differences is attributed to the island edge binding strength to the substrate, where R0 domains have edges that are more tightly bound than rotated domains.

The determination of the growth species was also critically facilitated by LEEM. By determining the growth rate as a function of the C adatom concentration, it was determined that growth of R0 domains occurs by the attachment of a 4-atom C cluster to kinks. The kink-nucleation-limited growth of rotated domains is much more complex to model, and given significant simplification, it was determined that the sum of the cluster sizes for kink nucleation and kink advancement are of the order 6 to 8.

In Chapter 5, the evolution of graphene rotational variants on Ir(111) was observed during annealing. Three distinct mechanisms in which graphene domains reorient themselves were discovered. It was shown that the preferred orientation on Ir(111) is R0. The driving force for this reorientation was estimated by controlling the ripening with temperature and was determined to be on the order of 0.1 meV/C. A simple model of the atomic-scale corrugation and resulting energy of the graphene sheet was determined as a function of the rotation angle. The results were in good agreement with the experimental data. It is proposed that the origin of the preferential alignment is caused by the varying degree to which carbon atoms can attain the preferred distance from the substrate: the graphene bending rigidity prevents the sheet from following the short wavelength corrugations inherent in highly rotated domains. Furthermore, it suggests that in order to control the rotational order of 2D materials, they should be grown on substrates that induce these corrugations, e.g., metals. Finally, these results show that annealing graphene films immediately after nucleation can improve rotational order.

6.2 Unifying growth and reorientation results

The investigation into the growth kinetics was bifurcated: R0 and rotated. However, the ripening results show that the energetics are a continuous function of orientation. The question then arises for the growth kinetics: is there an abrupt change in growth mechanism (kink-advancement- to kink-nucleation-limited), or is there a gradual change as the rotation angle increases? The rotated islands investigated here were exclusively in the range of 12 to 18 degrees of rotation. These rotations were predominantly prevalent under the nucleation conditions used here. Some control over the nucleation is possible by adjusting the temperature. However, less rotated domains tended to be incorporated in islands that had many (4+) domains in them; for the growth experiments, islands with the fewest domains were chosen for simplicity and to mitigate the effects of domain boundaries on growth. Based on the results here, in the author's mind, it is safe to assume that R12-R30 are kink-nucleation-limited. The transition from kink-advancement-limited to kink-nucleation-limited is less clear. However, the ripening example presented in Figure 5.1 provides insight. When the R12 domain changed to R4, the island grows. Specifically, one of the original R12 edges quickly grows itself out. This supports a picture in which the growth of the R4 domain is controlled by kink density, and thus its growth is kink-nucleation-limited. This suggests that the growth mechanism transition may be limited to the narrow range of R0-R4. One possible investigation would be to analyze island shapes as a function of rotation angle. Since the growth kinetics are reflected in the resulting island shape, this analysis would provide insight, i.e., it would be straightforward to determine if the island shape abruptly or more continuously changes with rotation angle. Another potential investigation involves using STM to observe the graphene edges of various misoriented domains.

Finally, it is noted that the difference in equilibrium adatom concentrations between rotated domains and R0 does not appreciably affect the analysis of the growth kinetics in

Chapter 4. In general, it was assumed that before growth the islands were in equilibrium with the adatom concentration. Clearly, the ripening results indicate that this is never precisely true unless a single orientation exists on the substrate. However, a difference in chemical potential on the order of 0.1 meV/C translates to a difference in equilibrium adatom concentration on the order of 0.1% (10^{-5} ML for $kT \approx 0.1$ eV, an order of magnitude less than the standard deviation of the LEEM reflectivity measurement). Notably, this demonstrates the ability to minutely control the adatom concentration by adjusting the substrate temperature.

6.3 Future directions

In the following sections, possible future investigations that have arisen from the work here are presented and discussed.

6.3.1 Modeling the graphene edge/substrate interaction

As concluded in Chapter 4, the source of the different growth mechanisms is the variation in the graphene island edge binding strength to the substrate. Precisely why this depends on orientation and how exactly it affects kink formation are not entirely clear. What is known is that the moiré (corrugation) of the graphene sheet changes significantly with rotation and is potentially a significant contributing factor to the orientation dependence. Atomic-scale modeling of this edge interaction should prove fruitful in further understanding this interaction.

6.3.2 Domain boundaries between R0 and rotated domains

As mentioned previously, the formation of domain boundaries depends on the shapes of the coalescing islands. In particular, an interesting situation is the boundary formation between R0 and rotated islands. How do the the distinctly different edge morphologies (high kink density versus low kink density) affect the formation of the boundary and its resulting structure and electronic properties? Are the boundaries between R0/R0, R0/rotated, and rotated/rotated significantly different, and if so, how? How do the differences in edge binding strength affect the boundary formation? Scanning tunneling microscopy, transmission electron microscopy, and atomic modeling would provide further insight.

6.3.3 Modeling the continuous lattice rotation mechanism

Another atomic modeling effort is needed to further understand the continuous lattice rotation mechanism observed in Chapter 5. Many open questions remain on this mechanism. Are the atomic shifts accommodated by strain or bond breaking (dislocations). How is the rotation accommodated at the edges? In the example shown in Figure 5.1, and as discussed

above, an edge of a reoriented domain undergoes a period of non-steady growth as it assumes its new orientation. Given that the adatom concentration is constant, this suggests that the kink density drives the growth rate in this case. One possible scenario is the following: the edge is oriented for R12, the interior rotates and resultingly develops kinks at the edge, at which point the edge grows until the highly-kinked edge grows itself out and the edge reaches the typical orientation associated with R4.

6.3.4 Applying the moiré corrugation model to other systems

As noted in Chapter 5, the moiré corrugation model developed here can be applied to other substrates. The model only requires DFT to be performed for one orientation of graphene on a chosen substrate. Thus, one can consider other (111)-terminated materials (metals, germanium), but also other surface terminations, e.g., (110), (100), etc. This model is not limited to graphene either. Other 2D materials can be investigated. This requires knowing the bending rigidity of the 2D material. Such information is available; for example the bending rigidity of single-layer MoS₂ is estimated to be ~ 9.6 eV [147].

6.3.5 Ultra-fast LEED of graphene nucleation

It is possible that the continuous lattice rotation reorientation mechanism plays a significant role in the initial stages of nucleation and growth of graphene islands. In Chapter 5, it was suggested that this mechanism can explain why some substrates have significantly better rotational alignment than others. A way to probe this is ultra-fast LEED during graphene nucleation. Such a system has recently been developed [148]. In general, one could expose the substrate to a hydrocarbon at low temperature, such that the sticking coefficient is near one. The pump laser (~ 100 femtoseconds [148]) could be used to locally heat the substrate, dissociating the hydrocarbon and resulting in the nucleation of graphene islands. The probe signals (~ 100 electrons emitted from a tungsten tip and excited by the second-harmonic of the probe laser [148]) can then immediately collect the LEED pattern. The anticipated result is that one would initially see nucleation of many randomly oriented domains that then rotate to a preferred orientation.

6.3.6 Mosaicity in bilayer graphene

The next front in graphene growth is arguably the controlled synthesis of high-quality bilayer graphene. Large-scale production will require growth, not exfoliation and physical stacking of two graphene layers. Synthesis methods appear to be limited to physical vapor deposition (growth by segregation from the substrate has difficulty in controlling layer thickness). For example, CVD is self-limiting to a single monolayer. After that, C atoms would have to be deposited by evaporation. Based on the fact that the second layer of bilayer graphene grows between the substrate and the initial layer [67, 68], it is believed that C atoms can penetrate the top layer and become adatoms on the substrate, at which point they undergo typical

diffusion, nucleation, and growth. The question is if pristine bilayer graphene can be grown, i.e., what controls the orientation of the nucleation events of the second layer? Specifically, how does the top graphene layer affect the corrugation of the second layer? If this corrugation is severely diminished due to the interaction with the top layer, it may present significant, or even insurmountable, challenges in producing pristine bilayer graphene.

Appendix A

Supplementary data

This appendix contains the data that was used in this dissertation but not displayed in the previous chapters.

A.1 Islands used for shape analysis

A sample of the islands used for the Fourier transform shape analysis are shown below.

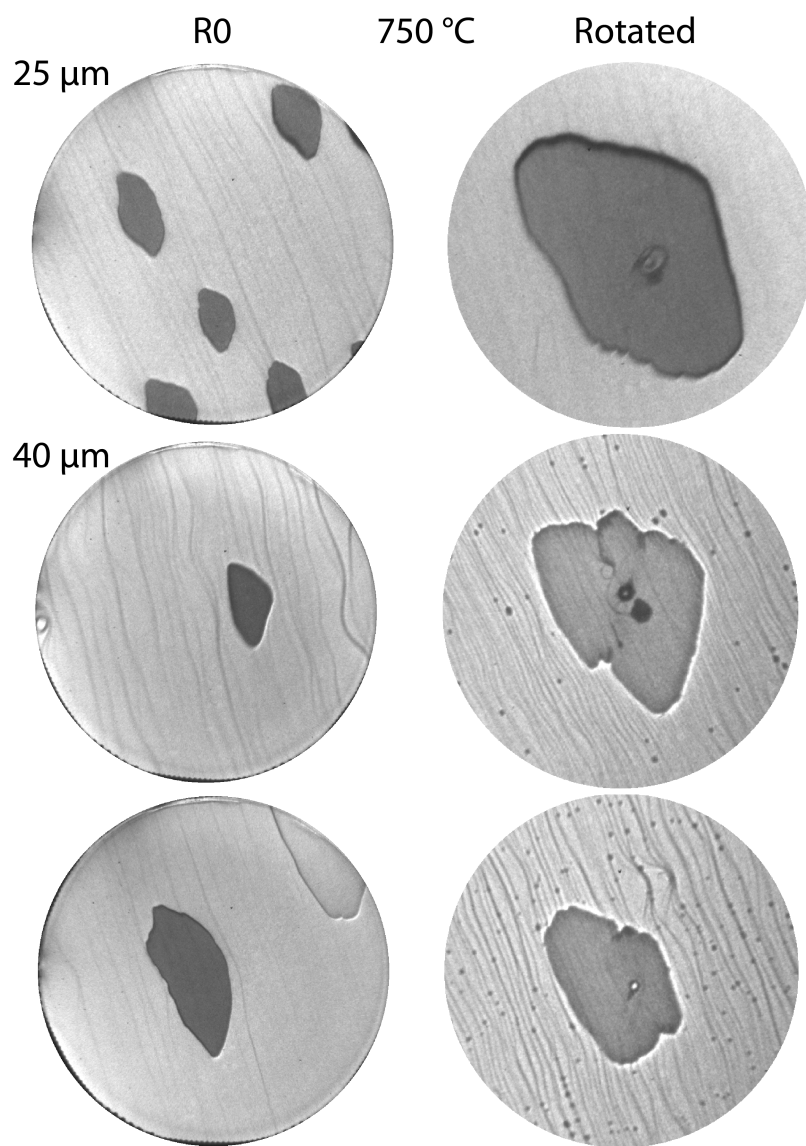


Figure A.1: R0 and rotated graphene island shapes at 750 °C. FOV = 50 μm unless otherwise noted.

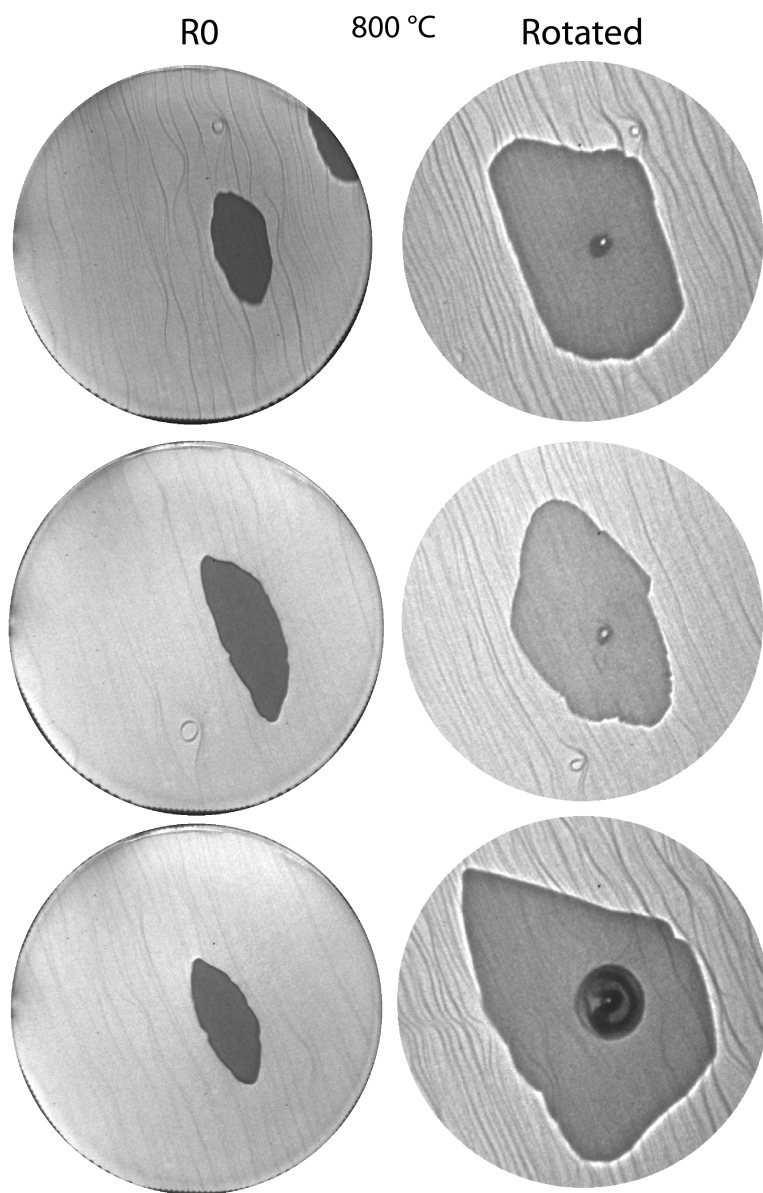


Figure A.2: R0 and rotated graphene island shapes at 800 °C. FOV = 50 μm .

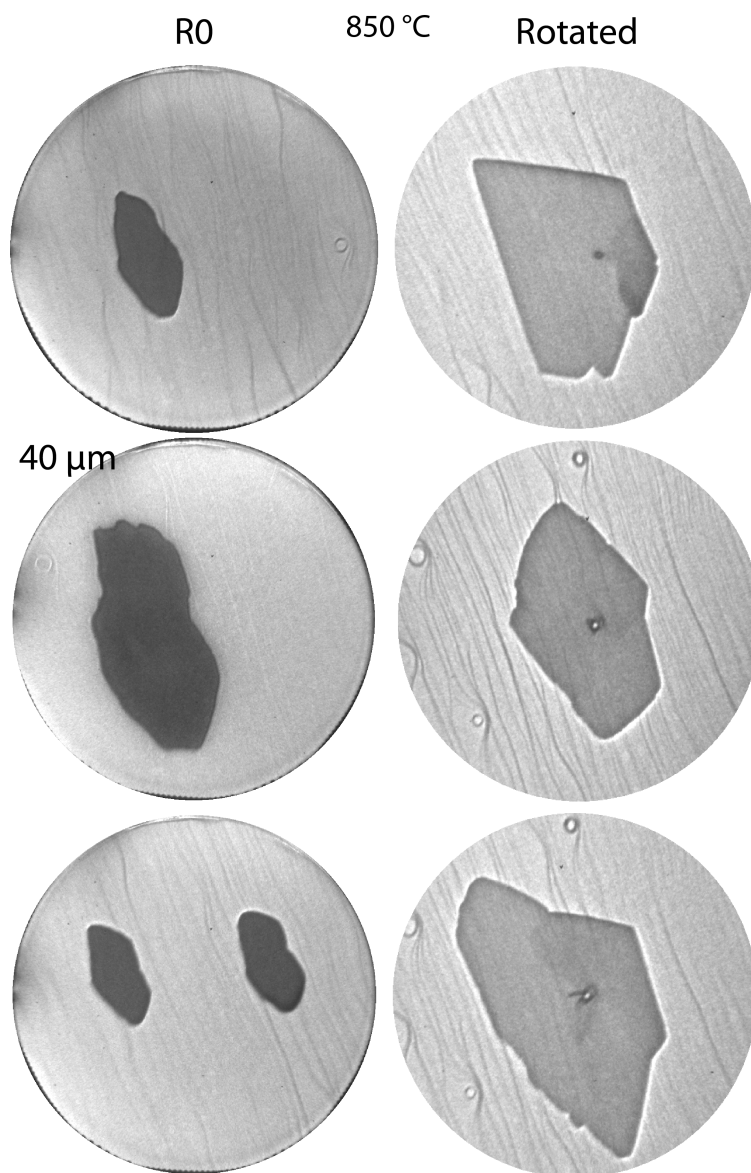


Figure A.3: R0 and rotated graphene island shapes at 850 °C. FOV = 50 μm unless otherwise noted.

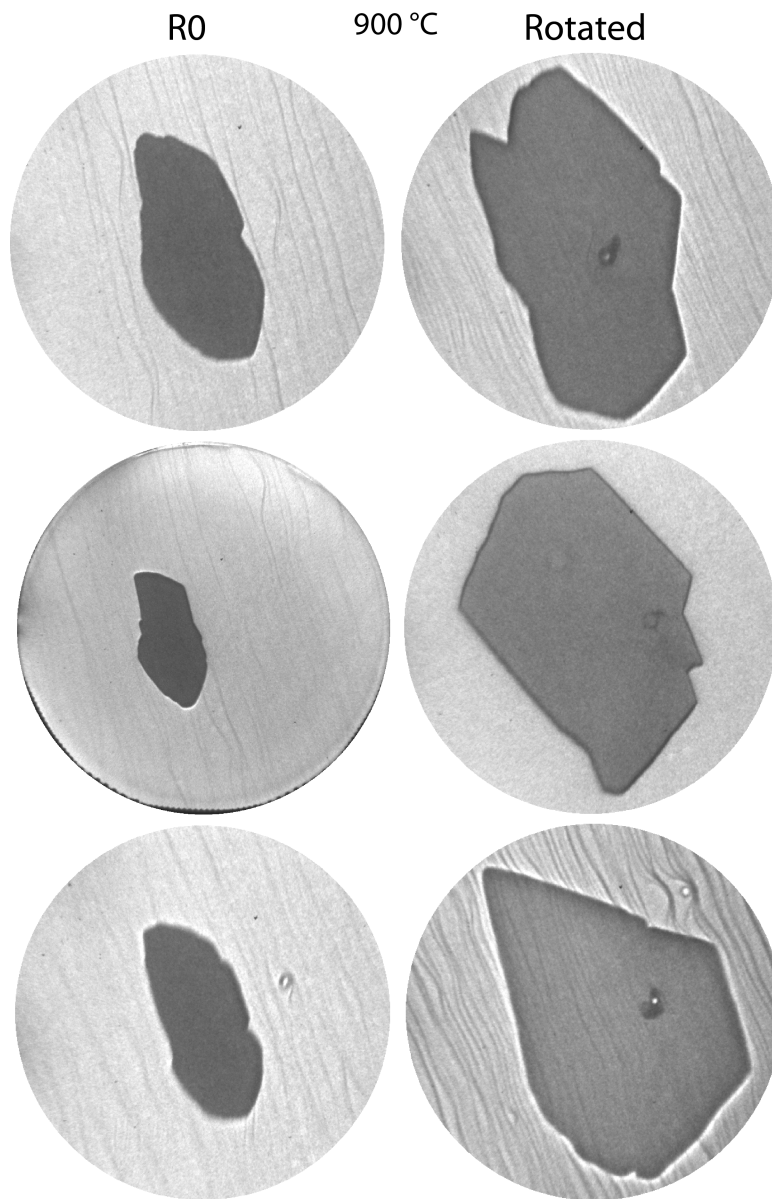


Figure A.4: R0 and rotated graphene island shapes at 900 °C. FOV = 50 μm .

A.2 Island growth experiments

The R0 and rotated island growths at the various temperatures are shown below. The 850 °C results are shown in Figure 4.8.

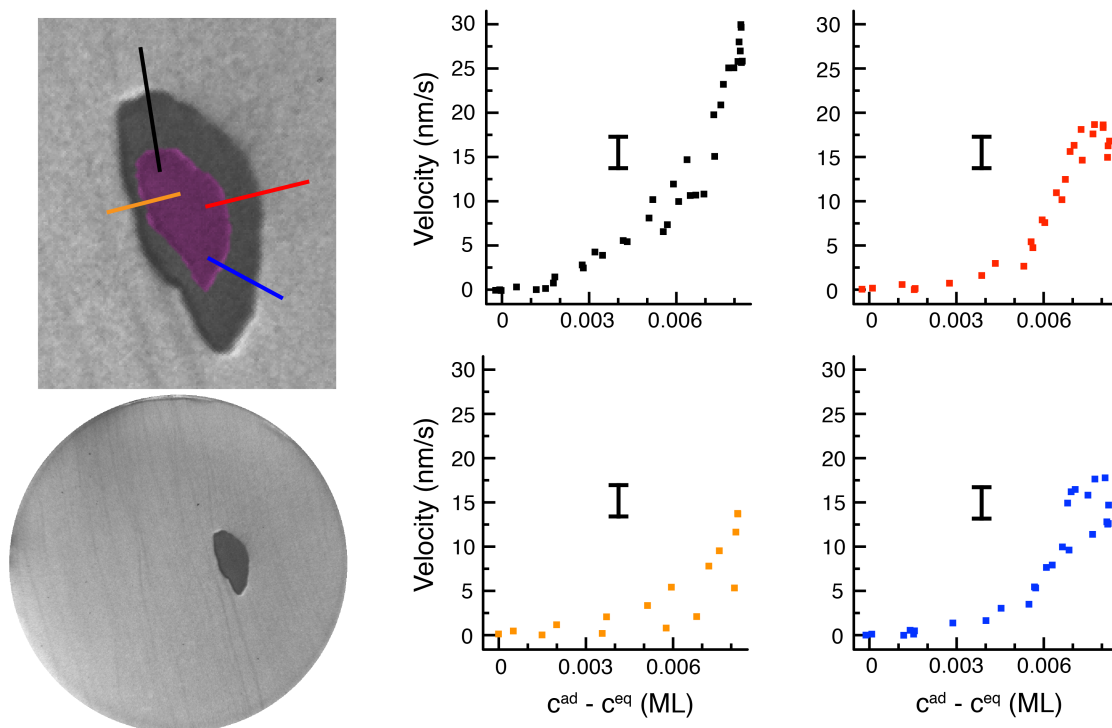


Figure A.5: 750 °C R0 island growth and local velocity measurements. Left side has the LEEM image stack and underneath is a LEEM image after growth (FOV = 40 μm). Right: local velocity measurements; colors correspond to lines in the image stack where velocities were measured.

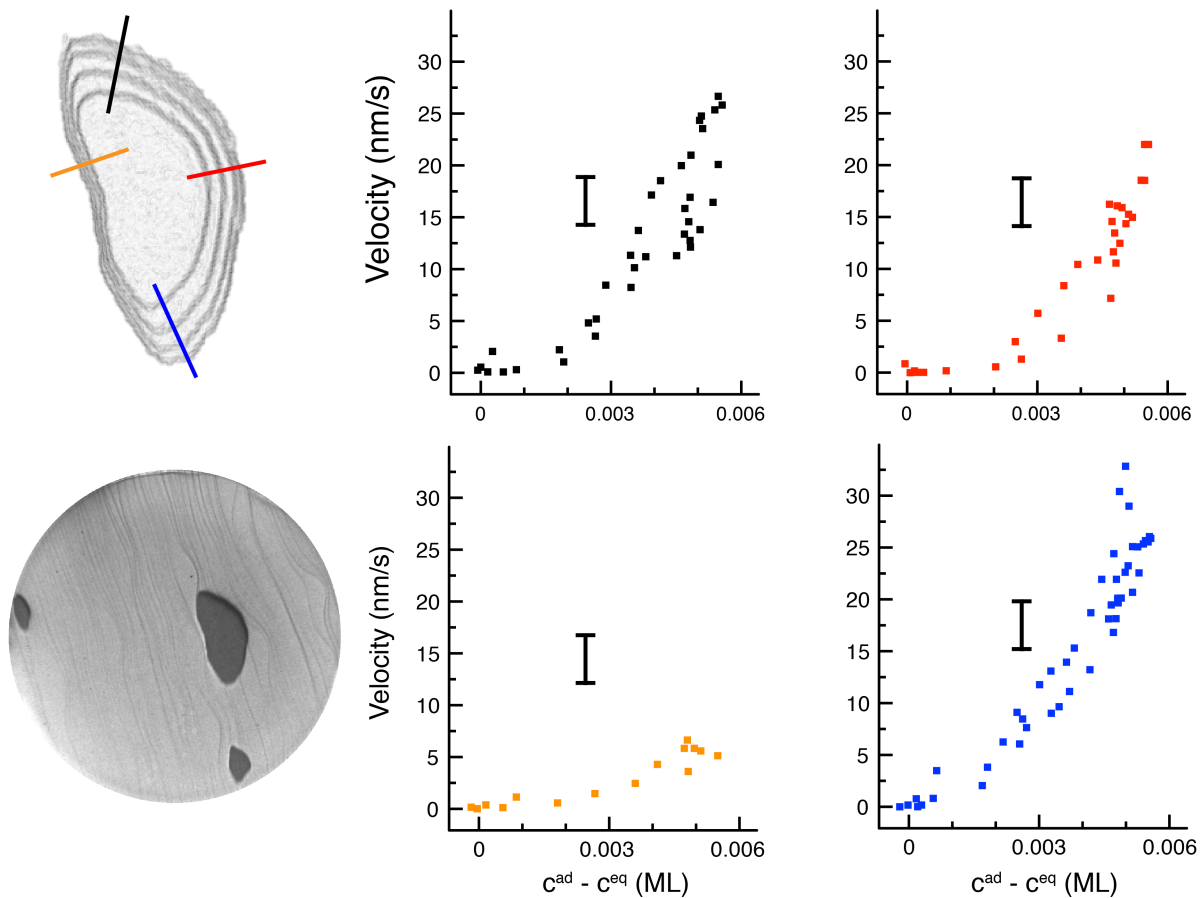


Figure A.6: 800 °C R0 island growth and local velocity measurements. Left side has the LEEM image stack and underneath is a LEEM image after growth (FOV = 50 μm). Right: local velocity measurements; colors correspond to lines in the image stack where velocities were measured.

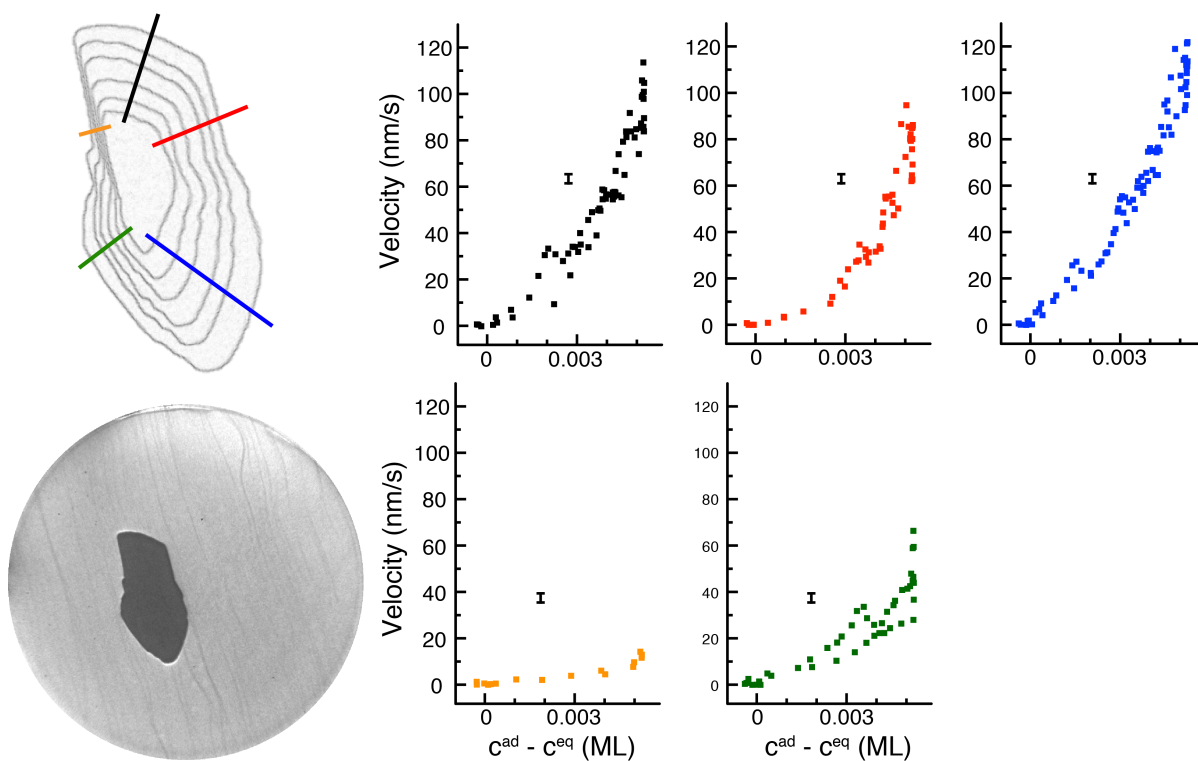


Figure A.7: 900 °C R0 island growth and local velocity measurements. Left side has the LEEM image stack and underneath is a LEEM image after growth (FOV = 50 μm). Right: local velocity measurements; colors correspond to lines in the image stack where velocities were measured. The green data do exhibit differences from other velocity measurements, but it is noted these were taken from an edge growing in the uphill step direction that underwent a change in orientation away from the uphill direction and started growing more quickly.

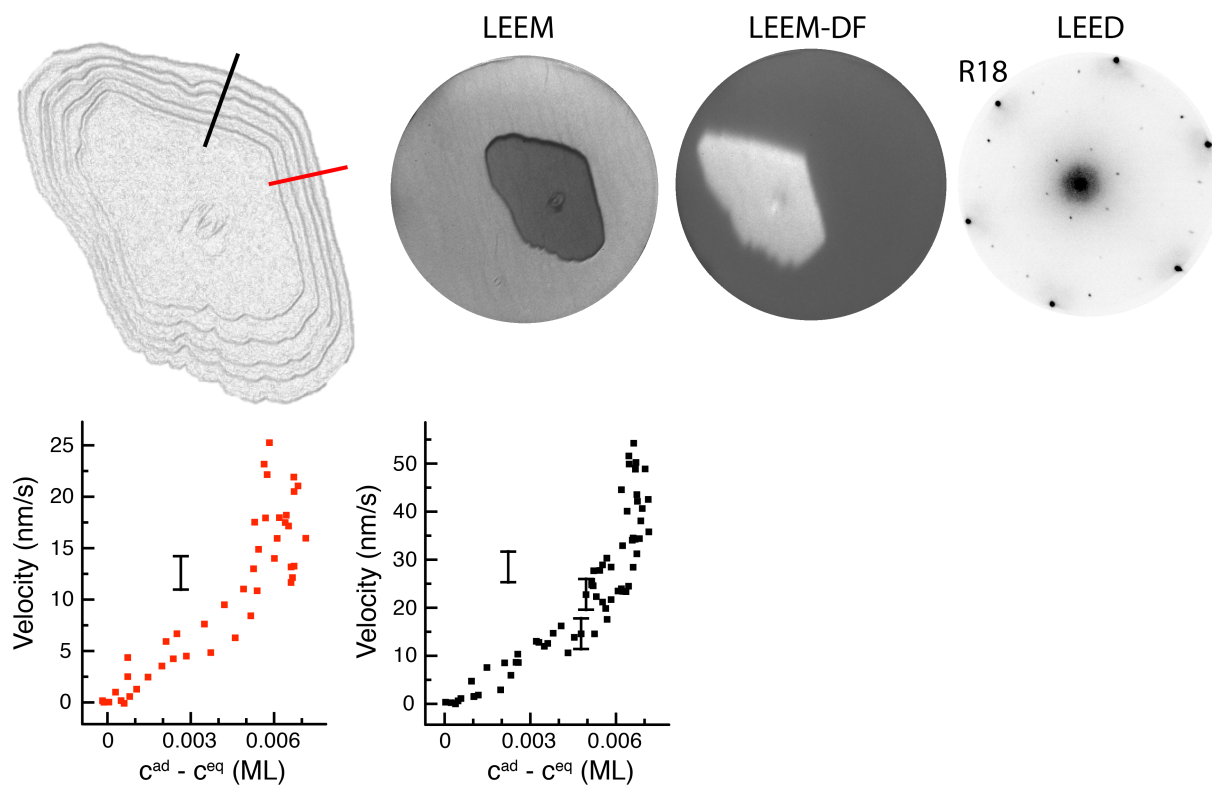


Figure A.8: 750 °C rotated island growth and local velocity measurements. Top: LEEM image stack, LEEM image of final island, LEEM dark field image of the island and the island LEED pattern. Bottom: local velocity measurements, color-coded to lines in the image stack.

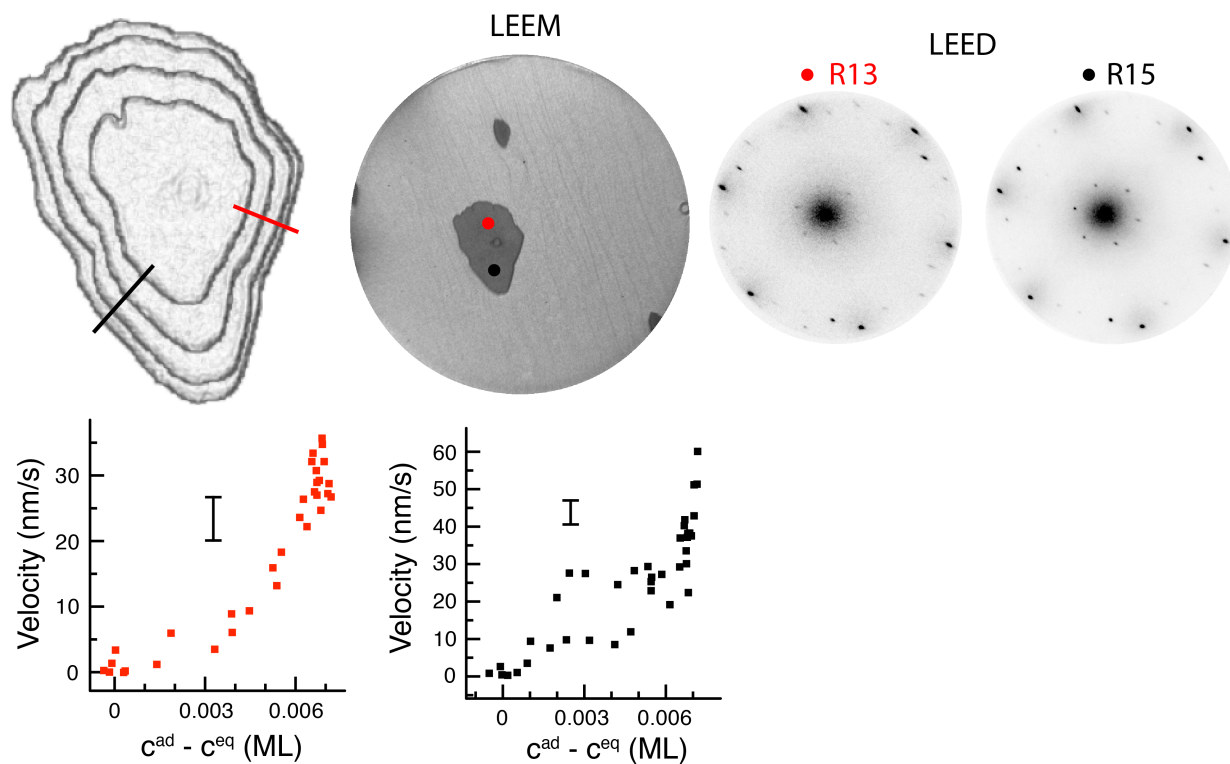


Figure A.9: 800 °C rotated island growth and local velocity measurements. Top: LEEM image stack, LEEM image of final island, and the LEED pattern of the island showing the orientations. Bottom: local velocity measurements, color-coded to lines in the image stack.

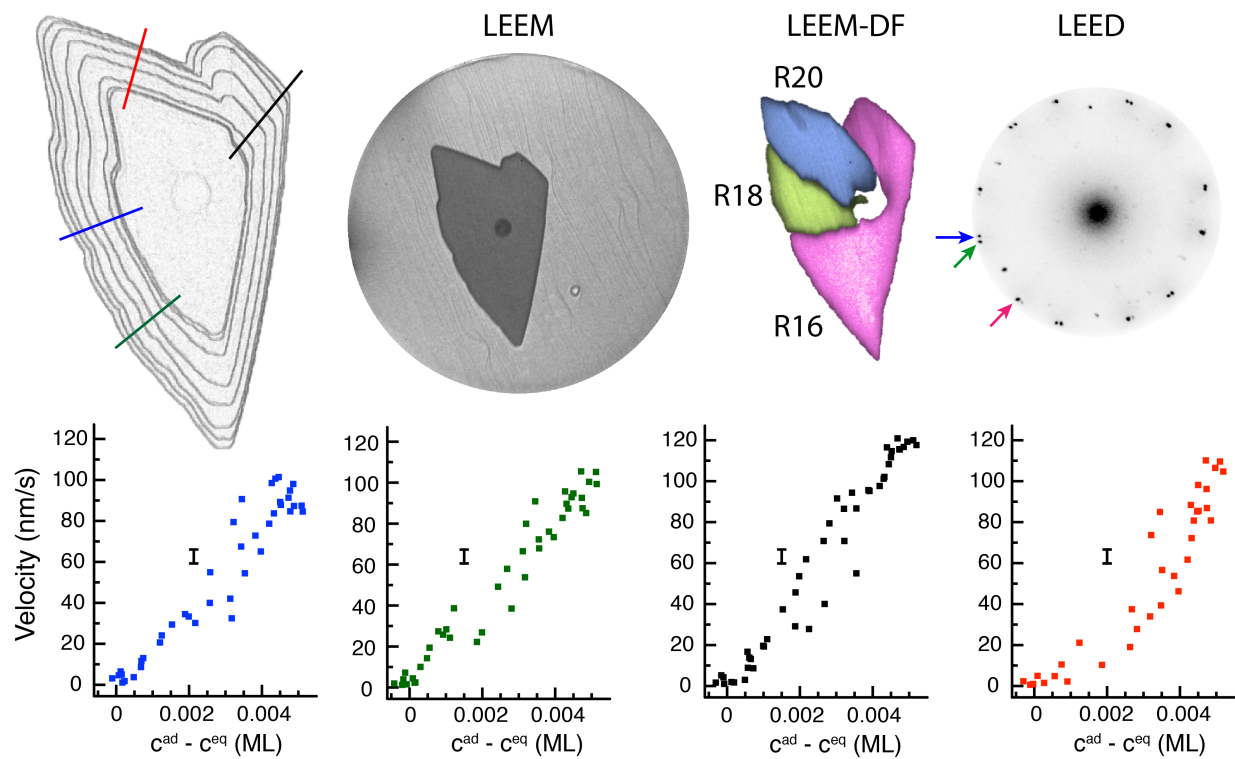


Figure A.10: 900 °C rotated island growth and local velocity measurements. Top: LEEM image stack, LEEM image of final island, false-colored dark-field LEEM images, and the LEED pattern of the island showing the orientations. Bottom: local velocity measurements, color-coded to lines in the image stack.

A.3 Ripening: Simultaneous growth and dissolution

This sections contains a few of the ripening experiments performed.

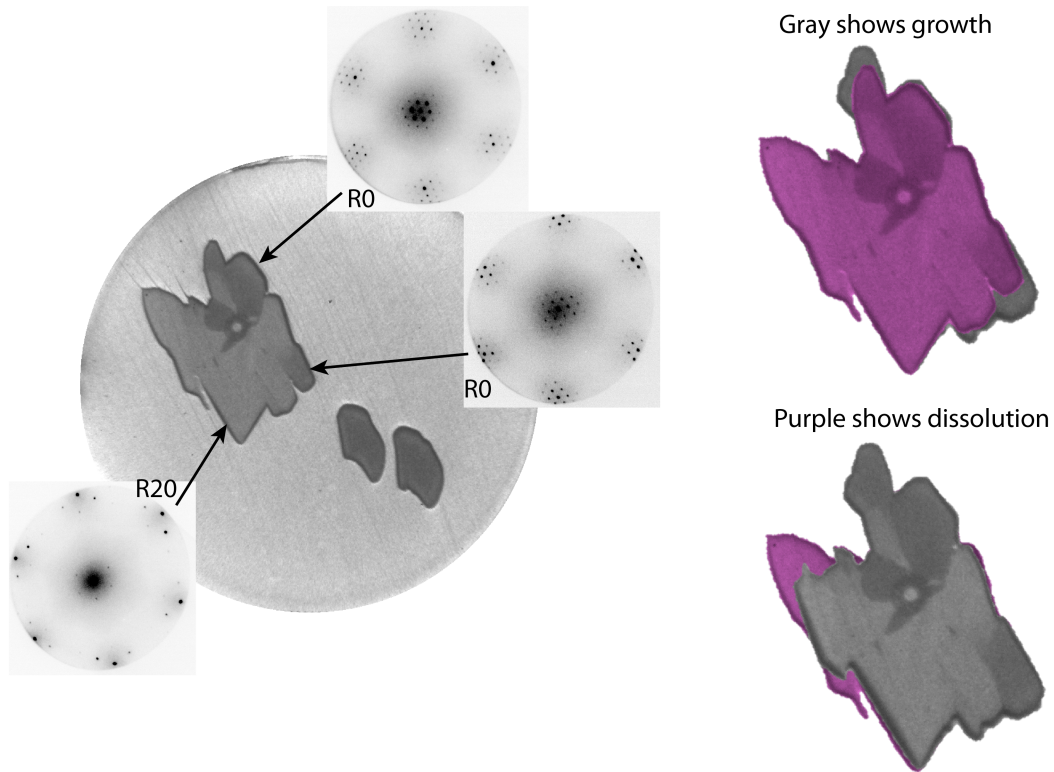


Figure A.11: An example of a ripening experiment at 860 °C, FOV = 50 μm . The R0 domains grew and the R20 domain shrank.

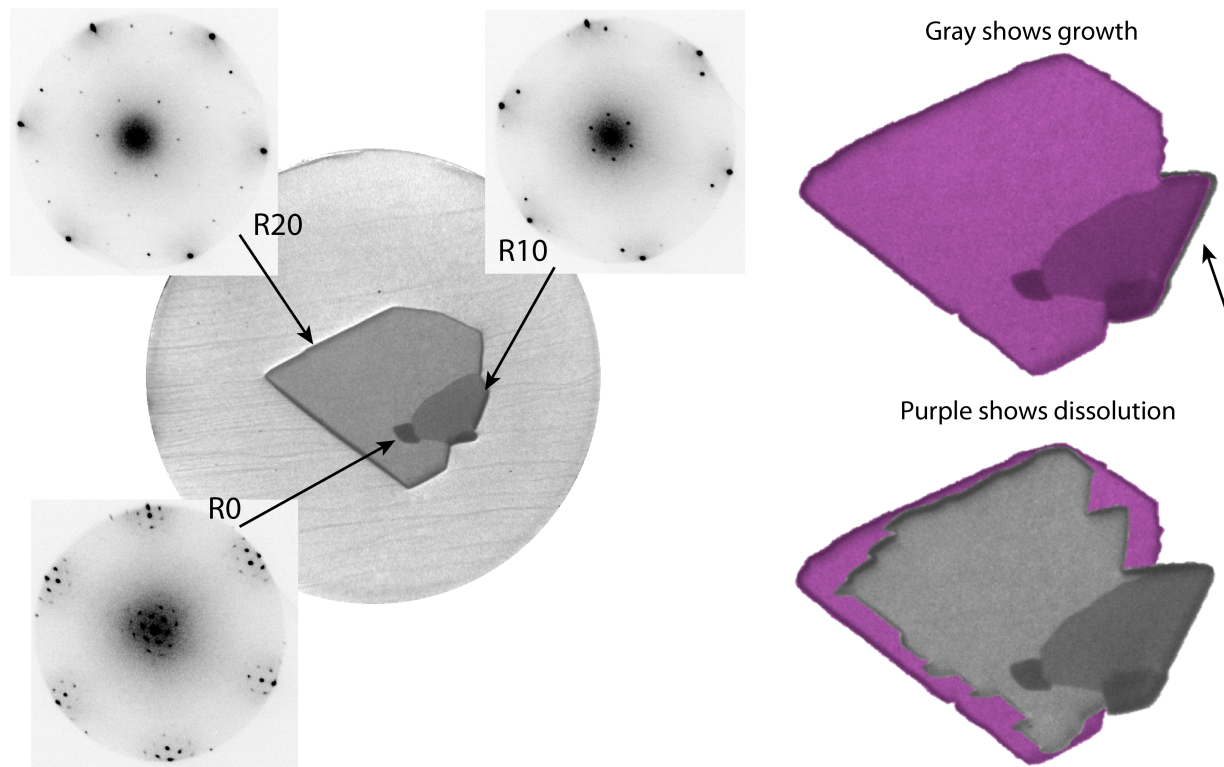


Figure A.12: An example of a ripening experiment at 1040 °C, FOV = 75 μm. The R10 domain grew slightly (highlighted by the arrow) and the R20 domain shrank.

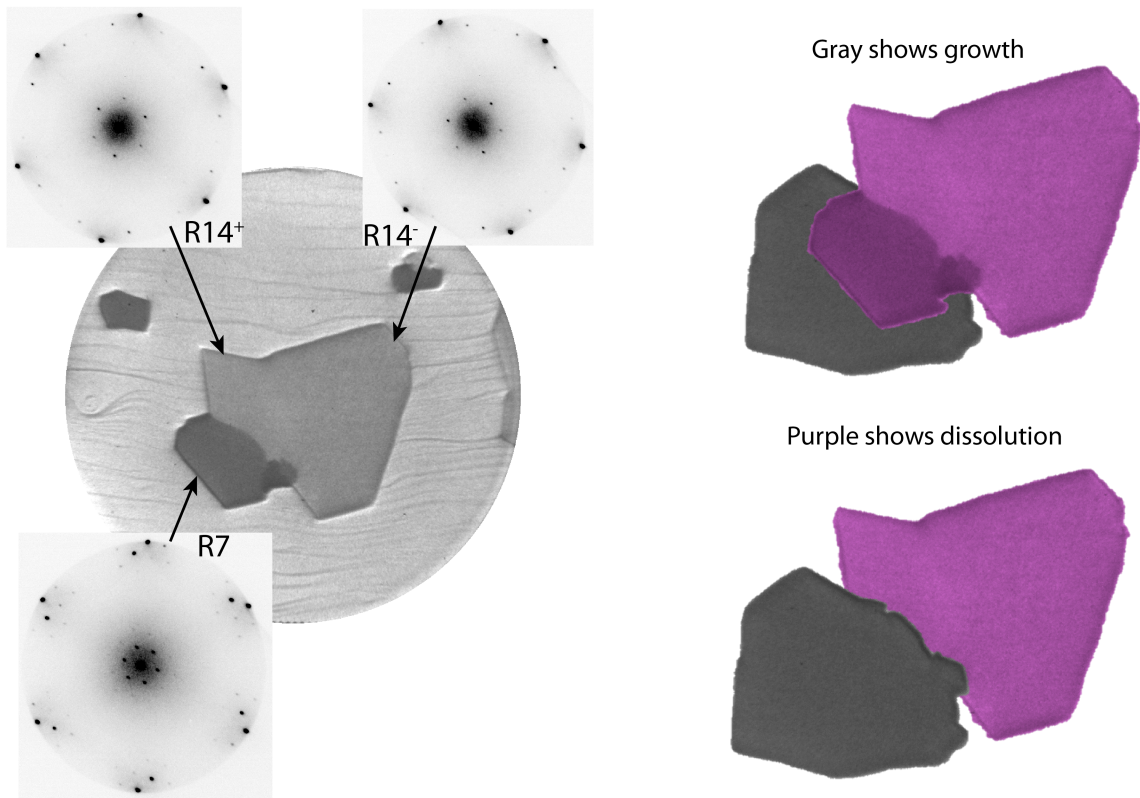


Figure A.13: An example of a ripening experiment at 1030 °C, FOV = 75 μm. The two R14 domains dissolved and the R7 domain grew.

A.4 Ripening: Continuous domain rotation

This section contains the other data sets in which the continuous lattice rotation ripening mechanism was observed.

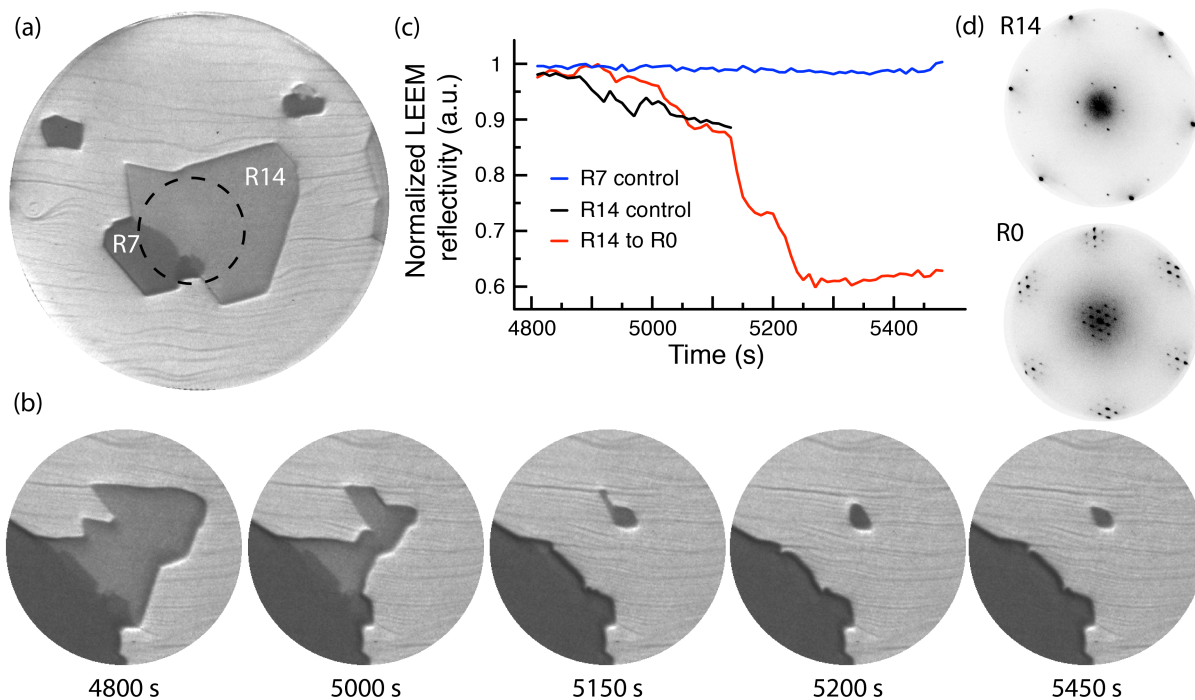


Figure A.14: An example of a continuous lattice rotation. (a) Starting LEEM image, FOV = 50 μm . (b) Domain evolution of the circled area in (a), FOV = 20 μm . As the R14 domain dissolves, a piece of graphene is left behind and undergoes a rotation to R0. (c) LEEM reflectivity shows the transition in time (R14 control data abruptly ends when the domain completely dissolves away). (d) LEED revealed that the remaining island was R0. Temperature was 1075 $^{\circ}\text{C}$.

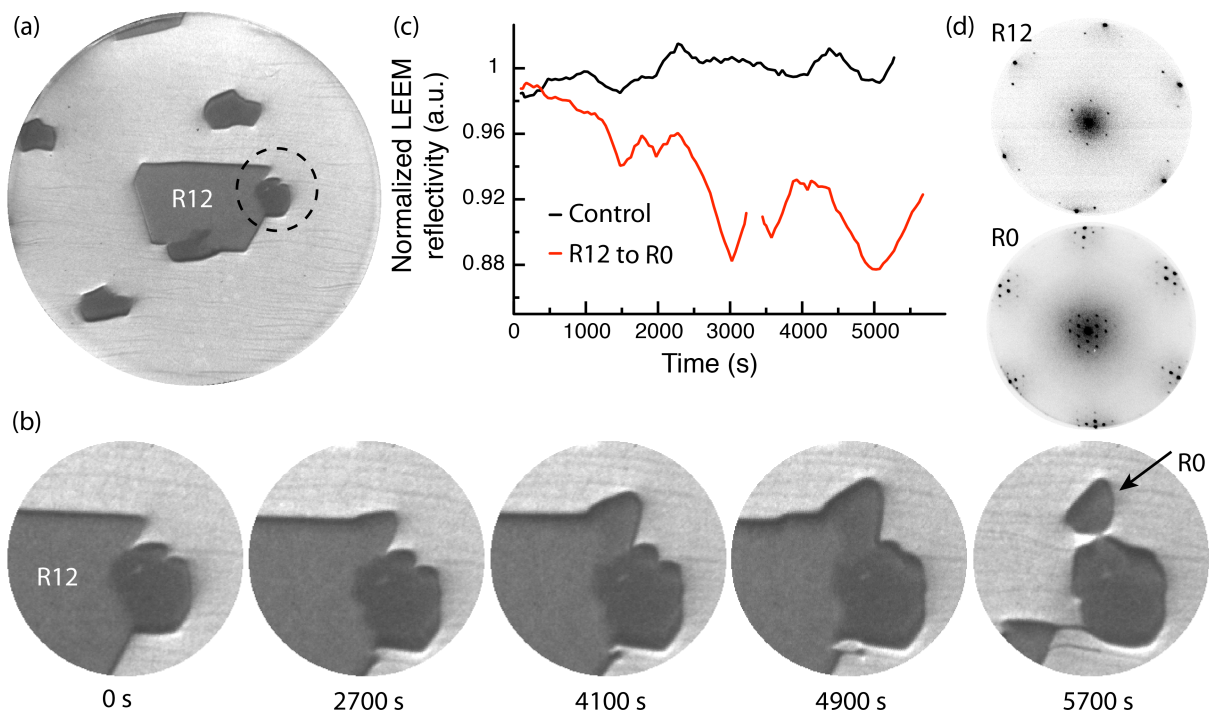


Figure A.15: An example of a continuous lattice rotation. (a) Starting LEEM image, FOV = 75 μm . (b) Domain evolution of the circled area in (a), FOV = 20 μm . A section of the R12 undergoes a rotation to R0. (c) LEEM reflectivity shows the transition in time. Because of thermal drift, two separate measurements of the transition region had to be combined, thus the discontinuity in the data. (d) LEED revealed that the section transformed to R0. This was a temperature-controlled ripening experiment, temperature ranged from 990 $^{\circ}\text{C}$ to 1115 $^{\circ}\text{C}$.

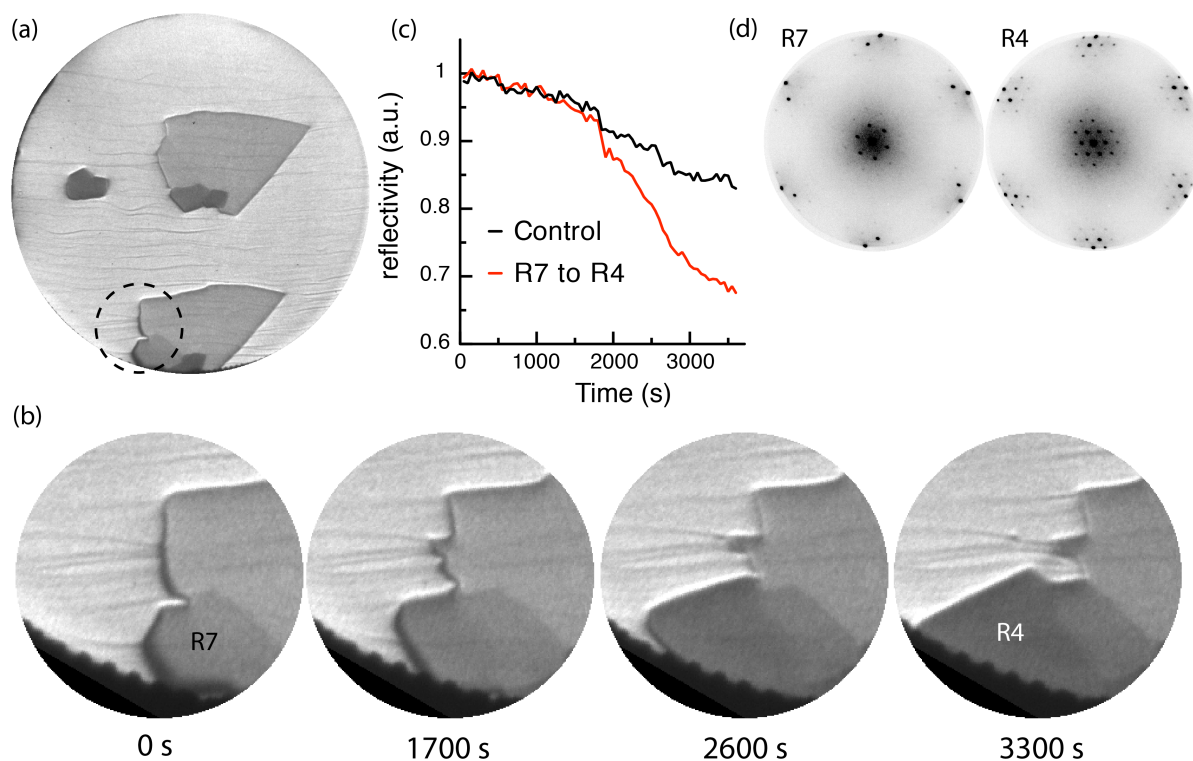


Figure A.16: An example of a continuous lattice rotation. (a) Starting LEEM image, FOV = 75 μm . (b) Domain evolution of the circled area in (a), FOV = 20 μm . A section of the R7 undergoes a rotation to R4. Note the change in edge orientation for the domain. (c) LEEM reflectivity shows the transition in time. (d) LEED revealed that the R7 domain transitioned to R4. This was a temperature-controlled ripening experiment, temperature ranged from 1020 $^{\circ}\text{C}$ to 1085 $^{\circ}\text{C}$.

Appendix B

Data analysis code

This appendix contains references to the code used for the data analysis throughout this dissertation. These files are electronically stored with the LEEM data.

B.1 Interactive Data Language (IDL)

LEEM reflectivity and general image information

Extract LEEM reflectivities, along with the general image information (temperature, start voltage, LEEM pressure, and time).

File: ivfixuvbox.pro

Island area and perimeter

The following programs were used to extract the island area and perimeter. In general, an edge-finding routine determines an outline of the island. A second program calculates the area and perimeter.

File: walk2_edge_smth.pro (edge-finding program)

File: ppsmth2.pro (area and perimeter calculation)

Converting LEEM images to island perimeters

To produce the LEEM image stacks, the LEEM images were modified such that an outline of the island image was produced and saved as a *.tiff file.

File: border_output.pro

B.2 Igor Pro code

The LEEM images were loaded into ImageTool written for Igor Pro. ImageTool was obtained from the Advanced Light Source community. Dr. David Siegel modified a procedure originally written by Dr. Taisuke Ohta to import the LEEM images into ImageTool, given below. The file is compiled and called in Igor Pro, for example “importLEEM(0,0,0,inf,1, “filename”)” imports all files in the chosen folder (pop-up window), starting at file 0 to all (infinity) files, with a step increase of 1.

File: DavidLEEMProcedures.ipf

B.3 ImageJ

An ImageJ macro was written for the shape analysis. The user imports an image stack of the desired files and then the following macro is run. The plugin ‘Oval Profile’ was downloaded from the internet.

File: FFT_Intensity_Profile.txt

File: Oval_Profile.java

Bibliography

- ¹K. S. Novoselov, A. K. Geim, S. V. Morozov, D. Jiang, Y. Zhang, S. Dubonos, I. Grigorieva, and A. Firsov, “Electric field effect in atomically thin carbon films”, *Science* **306**, 666–669 (2004).
- ²B. Nieuwenhuys, D. Hagen, G. Roviida, and G. Somorjai, “Leed, AES and thermal desorption studies of chemisorbed hydrogen and hydrocarbons (C₂H₂, C₂H₄, C₆H₆, C₆H₁₂) on the (111) and stepped [6(111)x(100)] iridium crystal surfaces; comparison with platinum”, *Surf. Sci.* **59**, 155–176 (1976).
- ³E. Rut’kov and A. Y. Tontegode, “A study of the carbon adlayer on iridium”, *Surf. Sci.* **161**, 373–389 (1985).
- ⁴A. Y. Tontegode, “Carbon on transition metal surfaces”, *Prog. Surf. Sci.* **38**, 201–429 (1991).
- ⁵N. Gall, E. Rut’Kov, and A. Y. Tontegode, “Two dimensional graphite films on metals and their intercalation”, *Int. J. of Mod. Phys. B* **11**, 1865–1911 (1997).
- ⁶A. Geim and K. Novoselov, “The rise of graphene”, *Nat. Mater.* **6**, 183–191 (2007).
- ⁷K. S. Novoselov, D. Jiang, F. Schedin, T. J. Booth, V. V. Khotkevich, S. V. Morozov, and A. K. Geim, “Two-dimensional atomic crystals”, *Proc. Nat. Acad. Sci. USA* **102**, 10451–10453 (2005).
- ⁸Q. Wang, K. Kalantar-Zadeh, A. Kis, J. Coleman, and M. Strano, “Electronics and optoelectronics of two-dimensional transition metal dichalcogenides”, *Nat. Nano.* **7**, 699–712 (2012).
- ⁹X. Li, W. Cai, J. An, S. Kim, J. Nah, D. Yang, R. Piner, A. Velamakanni, I. Jung, E. Tutuc, S. K. Banerjee, L. Colombo, and R. S. Ruoff, “Large-area synthesis of high-quality and uniform graphene films on copper foils”, *Science* **324**, 1312–1314 (2009).
- ¹⁰P. Sutter, J.-I. Flege, and E. Sutter, “Epitaxial graphene on ruthenium”, *Nat. Mater.* **7**, 406–411 (2008).
- ¹¹A. N’Diaye, J. Coraux, T. Plasa, C. Busse, and T. Michely, “Structure of epitaxial graphene on Ir(111)”, *New J. Phys.* **10**, 043033 (2008).

- ¹²J. M. Wofford, E. Starodub, A. Walter, S. Nie, A. Bostwick, N. C. Bartelt, K. Thürmer, E. Rotenberg, K. F. McCarty, and O. D. Dubon, “Extraordinary epitaxial alignment of graphene islands on Au(111)”, *New J. Phys.* **14**, 053008 (2012).
- ¹³P. Sutter, J. T. Sadowski, and E. Sutter, “Graphene on Pt(111): Growth and substrate interaction”, *Phys. Rev. B* **80**, 245411 (2009).
- ¹⁴Y. Murata, E. Starodub, B. B. Kappes, C. V. Ciobanu, N. C. Bartelt, K. F. McCarty, and S. Kodambaka, “Orientation-dependent work function of graphene on Pd(111)”, *Appl. Phys. Lett.* **97**, 143114, 143114 (2010).
- ¹⁵J.-H. Lee, E. K. Lee, W.-J. Joo, Y. Jang, B.-S. Kim, J. Y. Lim, S.-H. Choi, S. J. Ahn, J. R. Ahn, M.-H. Park, C.-W. Yang, B. L. Choi, S.-W. Hwang, and D. Whang, “Wafer-scale growth of single-crystal monolayer graphene on reusable hydrogen-terminated germanium”, *Science* **344**, 286–289 (2014).
- ¹⁶A. Koma, K. Sunouchi, and T. Miyajima, “Fabrication and characterization of heterostructures with subnanometer thickness”, *Microelectronic Engineering* **2**, Special Issue on Nanometer Structure Electronics, 129–136 (1984).
- ¹⁷A. Koma, K. Sunouchi, and T. Miyajima, “Fabrication of ultrathin heterostructures with van der Waals epitaxy”, *J. Vac. Sci. Technol. B* **3**, 724 (1985).
- ¹⁸A. Koma, “Van der Waals epitaxy - a new epitaxial growth method for a highly lattice-mismatched system”, *Thin Solid Films* **216**, 72–76 (1992).
- ¹⁹B. Parkinson, F. Ohuchi, K. Ueno, and A. Koma, “Periodic lattice distortions as a result of lattice mismatch in epitaxial films of two-dimensional materials”, *Appl. Phys. Lett.* **58**, 472–474 (1991).
- ²⁰E. Loginova, S. Nie, K. Thürmer, N. C. Bartelt, and K. F. McCarty, “Defects of graphene on Ir(111): Rotational domains and ridges”, *Phys. Rev. B* **80**, 085430 (2009).
- ²¹E. Loginova, N. C. Bartelt, P. J. Feibelman, and K. F. McCarty, “Factors influencing graphene growth on metal surfaces”, *New J. Phys.* **11**, 063046 (2009).
- ²²S. Nie, J. M. Wofford, N. C. Bartelt, O. D. Dubon, and K. F. McCarty, “Origin of the mosaicity in graphene grown on Cu(111)”, *Phys. Rev. B* **84**, 155425 (2011).
- ²³Y. Hao, M. S. Bharathi, L. Wang, Y. Liu, H. Chen, S. Nie, X. Wang, H. Chou, C. Tan, B. Fallahazad, H. Ramanarayan, C. W. Magnuson, E. Tutuc, B. I. Yakobson, K. F. McCarty, Y. W. Zhang, P. Kim, J. Hone, L. Colombo, and R. S. Ruoff, “The role of surface oxygen in the growth of large single-crystal graphene on copper”, *Science* **342**, 720–723 (2013).
- ²⁴Q. Yu, L. Jauregui, W. Wu, R. Colby, J. Tian, Z. Su, H. Cao, Z. Liu, D. Pandey, D. Wei, T. Chung, P. Peng, N. Guisinger, E. Stach, J. Bao, S.-S. Pei, and Y. Chen, “Control and characterization of individual grains and grain boundaries in graphene grown by chemical vapour deposition”, *Nat. Mater.* **10**, 443–449 (2011).

- ²⁵A. W. Tsen, L. Brown, M. P. Levendorf, F. Ghahari, P. Y. Huang, R. W. Havener, C. S. Ruiz-Vargas, D. A. Muller, P. Kim, and J. Park, “Tailoring electrical transport across grain boundaries in polycrystalline graphene”, *Science* **336**, 1143–6 (2012).
- ²⁶J. D. Bernal, “The structure of graphite”, *Proc. Royal Soc. A* **106**, 749 (1924).
- ²⁷C. Barrett and T. Massalski, *Structure of Metals*, 3rd (McGraw-Hill, 1966).
- ²⁸P. Wallace, “The band theory of graphite”, *Phys. Rev.* **71**, 622–634 (1947).
- ²⁹A. C. Neto, F. Guinea, N. M. R. Peres, K. S. Novoselov, and A. K. Geim, “The electronic properties of graphene”, *Rev. Mod. Phys.* **81**, 109–162 (2009).
- ³⁰L. Wang, I. Meric, P. Y. Huang, Q. Gao, Y. Gao, H. Tran, T. Taniguchi, K. Watanabe, L. M. Campos, D. A. Muller, J. Guo, P. Kim, J. Hone, K. L. Shepard, and C. R. Dean, “One-dimensional electrical contact to a two-dimensional material”, *Science* **342**, 614–617 (2013).
- ³¹F. Bonaccorso, Z. Sun, T. Hasan, and A. Ferrari, “Graphene photonics and optoelectronics”, *Nature Photonics* **4**, 611–622 (2010).
- ³²P. Blake, E. Hill, A. C. Neto, K. Novoselov, D. Jiang, R. Yang, T. Booth, and A. Geim, “Making graphene visible”, *Appl. Phys. Lett.* **91**, 063124 (2007).
- ³³C. Lee, X. Wei, J. W. Kysar, and J. Hone, “Measurement of the elastic properties and intrinsic strength of monolayer graphene”, *Science* **321**, 385–388 (2008).
- ³⁴L. Gomez De Arco, Y. Zhang, C. W. Schlenker, K. Ryu, M. E. Thompson, and C. Zhou, “Continuous, highly flexible, and transparent graphene films by chemical vapor deposition for organic photovoltaics”, *ACS Nano* **4**, 2865–2873 (2010).
- ³⁵B. J. Kim, H. Jang, S.-K. Lee, B. H. Hong, J.-H. Ahn, and J. H. Cho, “High-performance flexible graphene field effect transistors with ion gel gate dielectrics”, *Nano Lett.* **10**, 3464–3466 (2010).
- ³⁶T. Palacios, A. Hsu, and H. Wang, “Applications of graphene devices in RF communications”, *IEEE Commun. Mag.* **48**, 122–128 (2010).
- ³⁷R. Cheng, J. Bai, L. Liao, H. Zhou, Y. Chen, L. Liu, Y.-C. Lin, S. Jiang, Y. Huang, and X. Duan, “High-frequency self-aligned graphene transistors with transferred gate stacks”, *Proc. Nat. Acad. Sci. USA* **109**, 11588–11592 (2012).
- ³⁸E. W. Hill, A. Vijayaraghavan, and K. Novoselov, “Graphene sensors”, *IEEE Sens. J.* **11**, 3161–3170 (2011).
- ³⁹F. Schedin, A. Geim, S. Morozov, E. Hill, P. Blake, M. Katsnelson, and K. Novoselov, “Detection of individual gas molecules adsorbed on graphene”, *Nat. Mater.* **6**, 652–655 (2007).
- ⁴⁰K. Wakabayashi, M. Fujita, H. Ajiki, and M. Sigrist, “Electronic and magnetic properties of nanographite ribbons”, *Phys. Rev. B* **59**, 8271–8282 (1999).

- ⁴¹K. Nakada, M. Fujita, G. Dresselhaus, and M. S. Dresselhaus, “Edge state in graphene ribbons: Nanometer size effect and edge shape dependence”, *Phys. Rev. B* **54**, 17954–17961 (1996).
- ⁴²M. Y. Han, B. Özyilmaz, Y. Zhang, and P. Kim, “Energy band-gap engineering of graphene nanoribbons”, *Phys. Rev. Lett.* **98**, 206805 (2007).
- ⁴³E. V. Castro, K. S. Novoselov, S. V. Morozov, N. M. R. Peres, J. M. B. L. dos Santos, J. Nilsson, F. Guinea, A. K. Geim, and A. H. C. Neto, “Biased bilayer graphene: Semiconductor with a gap tunable by the electric field effect”, *Phys. Rev. Lett.* **99**, 216802 (2007).
- ⁴⁴Y. Zhang, T.-T. Tang, C. Girit, Z. Hao, M. C. Martin, A. Zettl, M. F. Crommie, Y. R. Shen, and F. Wang, “Direct observation of a widely tunable bandgap in bilayer graphene”, *Nature* **459**, 820–823 (2009).
- ⁴⁵Y. Kubota, K. Watanabe, O. Tsuda, and T. Taniguchi, “Deep ultraviolet light-emitting hexagonal boron nitride synthesized at atmospheric pressure”, *Science* **317**, 932–934 (2007).
- ⁴⁶E. Fortin and W. Sears, “Photovoltaic effect and optical absorption in mos₂”, *J. Phys. Chem. Solids* **43**, 881–884 (1982).
- ⁴⁷T. Roy, M. Tosun, J. S. Kang, A. B. Sachid, S. B. Desai, M. Hettick, C. C. Hu, and A. Javey, “Field-effect transistors built from all two-dimensional material components”, *ACS Nano* **8**, 6259–6264 (2014).
- ⁴⁸M. Xu, T. Liang, M. Shi, and H. Chen, “Graphene-like two-dimensional materials”, *Chem. Rev.* **113**, 3766 (2013).
- ⁴⁹Y. Zhang, Y.-W. Tan, H. L. Stormer, and P. Kim, “Experimental observation of the quantum Hall effect and Berry’s phase in graphene”, *Nature* **438**, 201–204 (2005).
- ⁵⁰E. Rollings, G.-H. Gweon, S. Zhou, B. Mun, J. McChesney, B. Hussain, A. Fedorov, P. First, W. De Heer, and A. Lanzara, “Synthesis and characterization of atomically thin graphite films on a silicon carbide substrate”, *Journal of Physics and Chemistry of Solids* **67**, 2172–2177 (2006).
- ⁵¹M. L. Bolen, S. E. Harrison, L. B. Biedermann, and M. A. Capano, “Graphene formation mechanisms on 4H-SiC(0001)”, *Phys. Rev. B* **80**, 115433 (2009).
- ⁵²R. Tromp and J. Hannon, “Thermodynamics and kinetics of graphene growth on SiC(0001)”, *Phys. Rev. Lett.* **102**, 106104 (2009).
- ⁵³M. K. Yakes, D. Gunlycke, J. L. Tedesco, P. M. Campbell, R. L. Myers-Ward, C. R. Eddy, D. K. Gaskill, P. E. Sheehan, and A. R. Laracuente, “Conductance anisotropy in epitaxial graphene sheets generated by substrate interactions”, *Nano Lett.* **10**, 1559–1562 (2010).
- ⁵⁴J. Hass, W. De Heer, and E. Conrad, “The growth and morphology of epitaxial multilayer graphene”, *J. Phys-Condens. Mat.* **20**, 323202 (2008).

- ⁵⁵F. Speck, J. Jobst, F. Fromm, M. Ostler, D. Waldmann, M. Hundhausen, H. Weber, and T. Seyller, “The quasi-free-standing nature of graphene on H-saturated SiC(0001)”, *Appl. Phys. Lett.* **99**, 122106 (2011).
- ⁵⁶J. A. Robinson, M. Hollander, M. LaBella III, K. A. Trumbull, R. Cavalero, and D. W. Snyder, “Epitaxial graphene transistors: Enhancing performance via hydrogen intercalation”, *Nano Lett.* **11**, 3875–3880 (2011).
- ⁵⁷E. Pallecchi, F. Lafont, V. Cavaliere, F. Schopfer, D. Maily, W. Poirier, and A. Ouerghi, “High electron mobility in epitaxial graphene on 4H-SiC(0001) via post-growth annealing under hydrogen”, *Sci. Rep.* **4** (2014).
- ⁵⁸J. Hass, R. Feng, T. Li, X. Li, Z. Zong, W. De Heer, P. First, E. Conrad, C. Jeffrey, and C. Berger, “Highly ordered graphene for two dimensional electronics”, *Appl. Phys. Lett.* **89**, 143106–143106 (2006).
- ⁵⁹M. Ohring, *Materials Science of Thin Films* (Academic press, 2001).
- ⁶⁰X. Li, C. W. Magnuson, A. Venugopal, R. M. Tromp, J. B. Hannon, E. M. Vogel, L. Colombo, and R. S. Ruoff, “Large-area graphene single crystals grown by low-pressure chemical vapor deposition of methane on copper”, *J. Am. Chem. Soc.* **133**, 2816–9 (2011).
- ⁶¹E. Loginova, N. C. Bartelt, P. J. Feibelman, and K. F. McCarty, “Evidence for graphene growth by C cluster attachment”, *New J. Phys.* **10**, 093026 (2008).
- ⁶²J. Coraux, A. T. N’Diaye, M. Engler, C. Busse, D. Wall, N. Buckanie, F.-J. Meyer zu Heringdorf, R. van Gastel, B. Poelsema, and T. Michely, “Growth of graphene on Ir(111)”, *New J. Phys.* **11**, 023006 (2009).
- ⁶³J. Coraux, A. T. N’Diaye, C. Busse, and T. Michely, “Structural coherency of graphene on Ir(111)”, *Nano Lett.* **8**, 565–570 (2008).
- ⁶⁴M. Olle, G. Ceballos, D. Serrate, and P. Gambardella, “Yield and shape selection of graphene nanoislands grown on Ni(111)”, *Nano Lett.* **12**, 4431–4436 (2012).
- ⁶⁵M. Li, J. B. Hannon, R. M. Tromp, J. Sun, J. Li, V. B. Shenoy, and E. Chason, “Equilibrium shape of graphene domains on Ni(111)”, *Phys. Rev. B* **88**, 041402 (2013).
- ⁶⁶G. Wang, M. Zhang, Y. Zhu, G. Ding, D. Jiang, Q. Guo, S. Liu, X. Xie, P. K. Chu, and Z. Di, “Direct growth of graphene film on germanium substrate”, *Sci. Rep.* **3** (2013).
- ⁶⁷S. Nie, A. L. Walter, N. C. Bartelt, E. Starodub, A. Bostwick, E. Rotenberg, and K. F. McCarty, “Growth from below: Graphene bilayers on Ir(111)”, *ACS Nano* **5**, 2298–2306 (2011).
- ⁶⁸S. Nie, W. Wu, S. Xing, Q. Yu, J. Bao, S.-s. Pei, and K. F. McCarty, “Growth from below: Bilayer graphene on copper by chemical vapor deposition”, *New J. Phys.* **14**, 093028 (2012).
- ⁶⁹Q. Yu, J. Lian, S. Siriponglert, H. Li, Y. P. Chen, and S.-S. Pei, “Graphene segregated on Ni surfaces and transferred to insulators”, *Appl. Phys. Lett.* **93**, 113103 (2008).

- ⁷⁰B. Predel, *C - Cu (Carbon - Copper)* (Madelung, O. (ed.). SpringerMaterials, 1992).
- ⁷¹W. Wu, Q. Yu, P. Peng, Z. Liu, J. Bao, and S.-S. Pei, “Control of thickness uniformity and grain size in graphene films for transparent conductive electrodes”, *Nanotechnology* **23**, 035603 (2012).
- ⁷²B. Kiraly, E. V. Iski, A. J. Mannix, B. L. Fisher, M. C. Hersam, and N. P. Guisinger, “Solid-source growth and atomic-scale characterization of graphene on Ag(111)”, *Nat. Commun.* **4** (2013).
- ⁷³J. M. Wofford, S. Nie, K. F. McCarty, N. C. Bartelt, and O. D. Dubon, “Graphene islands on Cu foils: The interplay between shape, orientation, and defects”, *Nano Lett.* **10**, 4890–4896 (2010).
- ⁷⁴S. Nie, N. C. Bartelt, J. M. Wofford, O. D. Dubon, K. F. McCarty, and K. Thürmer, “Scanning tunneling microscopy study of graphene on Au(111): Growth mechanisms and substrate interactions”, *Phys. Rev. B* **85**, 205406 (2012).
- ⁷⁵L. Gao, J. R. Guest, and N. P. Guisinger, “Epitaxial graphene on Cu(111)”, *Nano Lett.* **10**, 3512–3516 (2010).
- ⁷⁶N. Petrone, C. R. Dean, I. Meric, A. M. Van Der Zande, P. Y. Huang, L. Wang, D. Muller, K. L. Shepard, and J. Hone, “Chemical vapor deposition-derived graphene with electrical performance of exfoliated graphene”, *Nano Lett.* **12**, 2751–2756 (2012).
- ⁷⁷A. Reina, X. Jia, J. Ho, D. Nezich, H. Son, V. Bulovic, M. S. Dresselhaus, and J. Kong, “Large area, few-layer graphene films on arbitrary substrates by chemical vapor deposition”, *Nano Lett.* **9**, 30–35 (2008).
- ⁷⁸A. Reina, H. Son, L. Jiao, B. Fan, M. S. Dresselhaus, Z. Liu, and J. Kong, “Transferring and identification of single- and few-layer graphene on arbitrary substrates”, *J. Phys. Chem. C* **112**, 17741–17744 (2008).
- ⁷⁹J. Wofford, “Graphene growth on low carbon solubility metals”, PhD thesis (University of California, Berkeley, 2012).
- ⁸⁰[Http://eom.umicore.com/en/substrates/products/germaniumSubstrates/](http://eom.umicore.com/en/substrates/products/germaniumSubstrates/), 2014.
- ⁸¹[Http://www.cree.com/News-and-Events/Cree-News/Press-Releases/2012/August/150mm-wafers](http://www.cree.com/News-and-Events/Cree-News/Press-Releases/2012/August/150mm-wafers), 2012.
- ⁸²A. Dahal, R. Addou, P. Sutter, and M. Batzill, “Graphene monolayer rotation on Ni(111) facilitates bilayer graphene growth”, *Appl. Phys. Lett.* **100**, 241602 (2012).
- ⁸³A. Chernov, “Notes on interface growth kinetics 50 years after Burton, Cabrera and Frank”, *J. Cryst. Growth* **264**, 499–518 (2004).
- ⁸⁴A. Chernov, L. Rashkovich, and J. DeYoreo, “ABC of kink kinetics and density in a complex solution”, in *Perspectives on inorganic, organic, and biological crystal growth: From fundamentals to applications*, Vol. 916 (AIP Publishing, 2007), pp. 34–47.

- ⁸⁵L. N. Rashkovich, J. J. De Yoreo, C. A. Orme, and A. A. Chernov, “In situ atomic force microscopy of layer-by-layer crystal growth and key growth concepts”, *Crystallogr. Rep.* **51**, 1063–1074 (2006).
- ⁸⁶A. Chernov, L. Rashkovich, and P. Vekilov, “Steps in solution growth: dynamics of kinks, bunching and turbulence”, *J. Cryst. Growth* **275**, 1–18 (2005).
- ⁸⁷J. de la Figuera, N. Bartelt, and K. McCarty, “Electron reflectivity measurements of Ag adatom concentrations on W(100)”, *Surf. Sci.* **600**, 4062–4066 (2006).
- ⁸⁸K. F. McCarty, P. J. Feibelman, E. Loginova, and N. C. Bartelt, “Kinetics and thermodynamics of carbon segregation and graphene growth on Ru(0001)”, *Carbon* **47**, 1806–1813 (2009).
- ⁸⁹M. McCluskey and E. Haller, *Dopants and Defects in Semiconductors* (CRC Press, 2012).
- ⁹⁰R. E. Reed-Hill and R. Abbaschian, “Physical Metallurgy Principles”, (1973).
- ⁹¹J. J. De Yoreo and P. G. Vekilov, “Principles of crystal nucleation and growth”, *Rev. Mineral.* **54**, 57–93 (2003).
- ⁹²A. A. Chernov, *Modern Crystallography III: Crystal Growth* (Springer-Verlag, 1984).
- ⁹³J. De Yoreo, L. Zepeda-Ruiz, R. Friddle, S. Qiu, L. Wasylenki, A. Chernov, G. Gilmer, and P. Dove, “Rethinking classical crystal growth models through molecular scale insights: consequences of kink-limited kinetics”, *Cryst. Growth Des.* **9**, 5135–5144 (2009).
- ⁹⁴V. Voronkov, “The movement of an elementary step by means of the formation of one-dimensional nuclei”, *Sov. Phys. Crystallogr.* **15**, 8–13 (1970).
- ⁹⁵D. A. Porter and K. E. Easterling, *Phase Transformations in Metals and Alloys* (CRC press, 1992).
- ⁹⁶D. Rogilo, L. Fedina, S. Kosolobov, B. Ranguelov, and A. Latyshev, “Critical terrace width for two-dimensional nucleation during Si growth on Si(111)-(7x7) surface”, *Phys. Rev. Lett.* **111**, 036105 (2013).
- ⁹⁷W. Chung and M. Altman, “Kinetic length, step permeability, and kinetic coefficient asymmetry on the Si(111)(7x7) surface”, *Phys. Rev. B* **66**, 075338 (2002).
- ⁹⁸J. A. Venables, *Introduction to Surface and Thin Film Processes* (Cambridge University Press, 2000).
- ⁹⁹W. Pearson and G. Raynor, *A Handbook of Lattice Spacings and Structure of Metals and Alloys* (Pergamon Press, 1958).
- ¹⁰⁰J. Lauterbach, R. Boyle, M. Schick, W. Mitchell, B. Meng, and W. Weinberg, “The adsorption of CO on Ir(111) investigated with FT-IRAS”, *Surf. Sci.* **350**, 32–44 (1996).
- ¹⁰¹D. Hagen, B. Nieuwenhuys, G. Rovida, and G. Somorjai, “Low-energy electron diffraction, Auger electron spectroscopy, and thermal desorption studies of chemisorbed CO and O₂ on the (111) and stepped [6(111)x(100)] iridium surfaces”, *Surf. Sci.* **57**, 632–650 (1976).

- ¹⁰²C. Busse, P. Lazić, R. Djemour, J. Coraux, T. Gerber, N. Atodiresei, V. Caciuc, R. Brako, A. T. N'Diaye, S. Blügel, J. Zegenhagen, and T. Michely, “Graphene on Ir(111): Physisorption with chemical modulation”, *Phys. Rev. Lett.* **107**, 036101 (2011).
- ¹⁰³P. Lacovig, M. Pozzo, D. Alfé, P. Vilmercati, A. Baraldi, and S. Lizzit, “Growth of dome-shaped carbon nanoislands on Ir(111): The intermediate between carbidic clusters and quasi-free-standing graphene”, *Phys. Rev. Lett.* **103**, 166101 (2009).
- ¹⁰⁴H. S. Mok, A. Ebnonnasir, Y. Murata, S. Nie, K. F. McCarty, C. V. Ciobanu, and S. Kodambaka, “Kinetics of monolayer graphene growth by segregation on Pd(111)”, *Appl. Phys. Lett.* **104**, 101606, pages (2014).
- ¹⁰⁵B. Borca, S. Barja, M. Garnica, M. Minniti, A. Politano, J. M. Rodriguez-Garcia, J. J. Hinarejos, D. Farias, A. L. V. de Parga, and R. Miranda, “Electronic and geometric corrugation of periodically rippled, self-nanostructured graphene epitaxially grown on Ru(0001)”, *New J. Phys.* **12**, 093018 (2010).
- ¹⁰⁶E. N. Voloshina, E. Fertitta, A. Garhofer, F. Mittendorfer, M. Fonin, A. Thissen, and Y. S. Dedkov, “Electronic structure and imaging contrast of graphene moiré on metals”, *Sci. Rep.* **3**, 1072 (2013).
- ¹⁰⁷D. Martoccia, P. R. Willmott, T. Brugger, M. Björck, S. Günther, C. M. Schlepütz, A. Cervellino, S. A. Pauli, B. D. Patterson, S. Marchini, J. Wintterlin, W. Moritz, and T. Greber, “Graphene on Ru(0001): a 25x25 supercell”, *Phys. Rev. Lett.* **101**, 126102 (2008).
- ¹⁰⁸S. Sorensen, H. Fuchtbauer, A. Tuxen, A. Walton, and J. Lauritsen, “Structure and electronic properties on in-situ synthesized single-layer MoS2 on a gold surface”, *ACS Nano* **8**, 6788–6796 (2014).
- ¹⁰⁹D. Kim, D. Sun, W. Lu, Z. Cheng, Y. Zhu, D. Le, T. Rahman, and L. Bartels, “Toward the growth of an aligned single-layer MoS2 film”, *Langmuir* **27**, 11650–11653 (2011).
- ¹¹⁰F. Muller, K. Stowe, and H. Sachdev, “Symmetry versus commensurability: Epitaxial growth of hexagonal boron nitride on Pt(111) from B-Trichloroborazine (ClBNH)₃”, *Chem. Mater.* **17**, 3464–3467 (2005).
- ¹¹¹E. Bauer, “Science of Microscopy”, in, edited by P. Hawkes and J. Spence (Springer, 2008) Chap. 8: LEEM and SPLEEM, pp. 605–656.
- ¹¹²“Surface Science Techniques”, in, edited by G. Bracco and B. Hoist (Springer, 2013) Chap. 18: Low-energy electron microscopy, pp. 531–561.
- ¹¹³E. Bauer, “Low energy electron microscopy”, *Rep. Prog. Phys.* **57**, 895–938 (1994).
- ¹¹⁴B. Fultz and J. M. Howe, *Transmission Electron Microscopy and Diffractometry of Materials*, 3rd (Springer, 2008).
- ¹¹⁵R. Tromp, “Measuring and correcting aberrations of a cathode objective lens”, *Ultramicroscopy* **111**, 273–281 (2011).

- ¹¹⁶B. Poelsema, L. K. Verheij, and G. Comsa, “Direct evidence for two-dimensional Xe gas-solid phase transition on Pt(111) by means of thermal He scattering”, *Phys. Rev. Lett.* **51**, 2410 (1983).
- ¹¹⁷*Private communication with K. McCarty.*
- ¹¹⁸M. A. Van Hove, W. H. Weinberg, and C.-M. Chan, *Low-Energy Electron Diffraction: Experiment, Theory and Surface Structure Determination* (Springer-Verlag Berlin, 1986).
- ¹¹⁹A. Zangwill, *Physics at Surfaces* (Cambridge University Press, 1988).
- ¹²⁰S. Nie, Calibration performed using Fe304(100), unpublished.
- ¹²¹F. C. Frank, “On the kinematic theory of crystal growth and dissolution processes”, in *Growth and Perfection of Crystals* (1958), p. 411.
- ¹²²L. Jin, Q. Fu, H. Zhang, R. Mu, Y. Zhang, D. Tan, and X. Bao, “Tailoring the growth of graphene on Ru(0001) via engineering of the substrate surface”, *J. Phys. Chem. C* **116**, 2988–2993 (2012).
- ¹²³S.-h. Phark, J. Borme, A. L. Vanegas, M. Corbetta, D. Sander, and J. Kirschner, “Atomic structure and spectroscopy of graphene edges on Ir(111)”, *Phys. Rev. B* **86**, 045442 (2012).
- ¹²⁴S. Marchini, S. Günther, and J. Winterlin, “Scanning tunneling microscopy of graphene on Ru(0001)”, *Phys. Rev. B* **76**, 075429 (2007).
- ¹²⁵W. J. Arnoult and R. B. McLellan, “The solubility of carbon in rhodium, ruthenium, iridium, and rhenium”, *Scripta Metall. Mater.* **6**, 1013–1018 (1972).
- ¹²⁶J. Criscione, A. Smith, and H. Volk, “Protection of graphite from oxidation at 2100 deg c”, *AIAA Journal* **4**, 1791–1797 (1966).
- ¹²⁷E. Starodub, S. Maier, I. Stass, N. C. Bartelt, P. J. Feibelman, M. Salmeron, and K. McCarty, “Graphene growth by metal etching on Ru(0001)”, *Phys. Rev. B* **80**, 235422 (2009).
- ¹²⁸Bartelt, Theis, and Tromp, “Ostwald ripening of two-dimensional islands on Si(001)”, *Phys. Rev. B* **54**, 11741–11751 (1996).
- ¹²⁹O. Yazyev and S. Louie, “Topological defects in graphene: dislocations and grain boundaries”, *Phys. Rev. B* **81**, 195420 (2010).
- ¹³⁰K. Kim, Z. Lee, W. Regan, C. Kisielowski, M. Crommie, and A. Zettl, “Grain boundary mapping in polycrystalline graphene”, *ACS Nano* **5**, 2142–2146 (2011).
- ¹³¹S. Kurasch, J. Kotakoski, O. Lehtinen, V. Skákalová, J. Smet, C. E. Krill III, A. V. Krasheninnikov, and U. Kaiser, “Atom-by-atom observation of grain boundary migration in graphene”, *Nano Lett.* **12**, 3168–3173 (2012).
- ¹³²P. Y. Huang, C. S. Ruiz-Vargas, A. M. van der Zande, W. S. Whitney, M. P. Levendof, J. W. Kevek, S. Garg, J. S. Alden, C. J. Hustedt, Y. Zhu, J. Park, P. L. McEuen, and D. A. Muller, “Grains and grain boundaries in single-layer graphene atomic patchwork quilts”, *Nature* **469**, 389–392 (2011).

- ¹³³F. Grey and J. Bohr, “A symmetry principle for epitaxial rotation”, *Europhys. Lett.* **18**, 717 (1992).
- ¹³⁴L. Meng, R. Wu, L. Zhang, L. Li, S. Du, Y. Wang, and H.-J. Gao, “Multi-oriented moiré superstructures of graphene on Ir(111): Experimental observations and theoretical models”, *J. Phys. Condens. Matter.* **24**, 314214 (2012).
- ¹³⁵L. D. Landau and E. M. Lifshitz, *Theory of Elasticity*, 3rd (Pergamon Press, London, 1986).
- ¹³⁶S. Chen and D. Chrzan, “Continuum theory of dislocations and buckling in graphene”, *Phys. Rev. B* **84**, 214103 (2011).
- ¹³⁷J. Klimeš, D. R. Bowler, and A. Michaelides, “Van der waals density functionals applied to solids”, *Phys. Rev. B* **83**, 195131 (2011).
- ¹³⁸G. Kresse and J. Hafner, “Ab initio molecular dynamics for liquid metals”, *Phys. Rev. B* **47**, 558 (1993).
- ¹³⁹G. Kresse and J. Hafner, “Ab initio molecular-dynamics simulation of the liquid-metal-amorphous-semiconductor transition in germanium”, *Phys. Rev. B* **49**, 14251 (1994).
- ¹⁴⁰G. Kresse and J. Furthmüller, “Efficiency of ab-initio total energy calculations for metals and semiconductors using a plane-wave basis set”, *Comp. Mater. Sci.* **6**, 15–50 (1996).
- ¹⁴¹G. Kresse and J. Furthmüller, “Efficient iterative schemes for ab initio total-energy calculations using a plane-wave basis set”, *Phys. Rev. B* **54**, 11169 (1996).
- ¹⁴²M. Dion, H. Rydberg, E. Schröder, D. C. Langreth, and B. I. Lundqvist, “Van der waals density functional for general geometries”, *Phys. Rev. Lett.* **92**, 246401 (2004).
- ¹⁴³M. Corso, W. Auwärter, M. Muntwiler, A. Tamai, T. Greber, and J. Osterwalder, “Boron nitride nanomesh”, *Science* **303**, 217–220 (2004).
- ¹⁴⁴Y.-H. Lee, X.-Q. Zhang, W. Zhang, M.-T. Chang, C.-T. Lin, K.-D. Chang, Y.-C. Yu, J. T.-W. Wang, C.-S. Chang, L.-J. Li, et al., “Synthesis of large-area MoS₂ atomic layers with chemical vapor deposition”, *Adv. Mater.* **24**, 2320–2325 (2012).
- ¹⁴⁵A. M. van der Zande, P. Y. Huang, D. A. Chenet, T. C. Berkelbach, Y. You, G.-H. Lee, T. F. Heinz, D. R. Reichman, D. A. Muller, and J. C. Hone, “Grains and grain boundaries in highly crystalline monolayer molybdenum disulphide”, *Nat. Mater.* **12**, 554–561 (2013).
- ¹⁴⁶S. Najmaei, Z. Liu, W. Zhou, X. Zou, G. Shi, S. Lei, B. I. Yakobson, J.-C. Idrobo, P. M. Ajayan, and J. Lou, “Vapour phase growth and grain boundary structure of molybdenum disulphide atomic layers”, *Nat. Mater.* **12**, 754–759 (2013).
- ¹⁴⁷J.-W. Jiang, Z. Qi, H. S. Park, and T. Rabczuk, “Elastic bending modulus of single-layer molybdenum disulfide (MoS₂): finite thickness effect”, *Nanotechnology* **24**, 435705 (2013).
- ¹⁴⁸M. Gulde, S. Schweda, G. Storeck, M. Maiti, H. K. Yu, A. M. Wodtke, S. Schäfer, and C. Ropers, “Ultrafast low-energy electron diffraction in transmission resolves polymer/graphene superstructure dynamics”, *Science* **345**, 200–204 (2014).